

APPLYING SPECTRAL MIXTURE ANALYSIS (SMA) FOR SOIL INFORMATION
EXTRACTION ON THE AIRBORNE VISIBLE / INFRARED IMAGING SPECTROMETER
(AVIRIS) DATA

by

Luciano Jose de Oliveira Accioly

Thesis Submitted to the Faculty of the
DEPARTMENT OF SOIL, WATER AND ENVIRONMENTAL SCIENCE

In Partial Fulfillment of the Requirements
For the Degree of

DOCTOR OF PHILOSOPHY

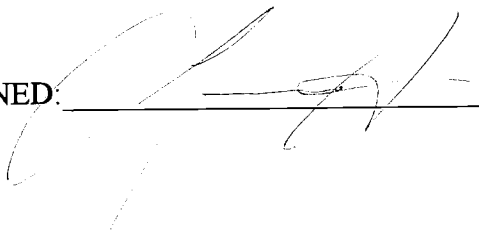
In the Graduate College
THE UNIVERSITY OF ARIZONA

1997

STATEMENT BY AUTHOR

This dissertation has been submitted in partial fulfillment of requirements for an advanced degree at The University of Arizona and is deposited in the University Library to be made available to borrowers under rules of the library.

Brief quotations from this dissertation are allowable without special permission, provided that accurate acknowledgement of source is made. Requests for permission for extended quotation from or reproduction of this manuscript in whole or in part may be granted by head of the major department or Dean of the Graduate College when in his or her judgment the proposed use of the material is in the interests of scholarship. In all other instances, however, permission must be obtained from the author.

SIGNED: 

ACKNOWLEDGMENTS

I am pleased to express my gratitude to those who taught and helped me complete my dissertation. To begin, I must express my special thanks to Dr. Alfredo R. Huete for his guidance and support as the dissertation director. I have great thankfulness to Dr. D. Post who taught me the value and excitement of learning. I also have a special thanks to Dr. Post for his friendship. I also wish to thank Dr. A. Matthias, Dr. S. Marsh, and Dr. S. Yool for their assistance during my research study.

I must also thank to K. Batchily and W. van Leeuwen for their assistance to this work. I have to extend my acknowledgements to many colleagues who helped me in the field and in the laboratory: T. Miura, E. Sano, G. de Lira. A special thanks I have to express for the friendship of J.C. Epiphonio.

My special thanks to my dear son Alexandre who helped me with some of the computer tasks, such as the cluster analysis graphs.

Finally I would like to thank for the support from the staff of the Department of Soil, Water, and Environmental Science: Judy, Lindy, Eleonor, Jan, and Barb.

DEDICATION

To my parents Jose Menezes e Maria Braulia (*in memoria*)

Dedicated with love and respect to my wife Fatima,

my son Alexandre and my daughter Paula

TABLE OF CONTENTS

	Page
LIST OF ILLUSTRATIONS.....	10
LIST OF TABLES	15
ABSTRACT	17
1. INTRODUCTION	19
Introduction, Objectives, and Statement of the Problem	19
Overview of the dissertation	22
2. SOIL SPECTRAL RESPONSE IN RELATION TO SENSOR VIEWING	
ANGLE, SOIL MOISTURE, AND SURFACE ROUGHNESS	24
Introduction	24
Methods	28
Results and Discussion	36
Field Spectra	36
Dry Conditions	42
Wet Conditions	45
RELAB Spectra	51
Effect of Roughness on the BRF Response of Epitaph Soil	57
Conclusions	67
3. IMAGE SPECTROSCOPY AS COMPARED TO FIELD AND LAB	
SPECTROSCOPY	70
Introduction	70

TABLE OF CONTENTS–Continued

	Page
Methods	76
Lab and Field Spectroscopy	76
Field Estimation of Ground Cover	77
Pre-processing AVIRIS image	77
Dimensionality of the Data Set	84
Results and Discussion	92
Comparing Field, Lab and AVIRIS Image Spectra	92
Comparing Field, Sieved Samples, RELAB and AVIRIS Spectra	
Using Derivative Spectroscopy	104
Grouping the Soils in Spectral Classes	117
Spectral Dimensionality of the Data Set	132
Conclusions	145
4. SPECTRAL MIXTURE ANALYSIS USING AVIRIS DATA	149
Introduction	149
Background	150
Methods	155
Site Description	155
Pre-processing AVIRIS Data	158
Spectral Mixture Analysis	160
Image Endmembers	160

TABLE OF CONTENTS–Continued

	Page
Fraction Images	163
Reference Endmembers	165
Problem Inherent in Selection of Endmembers	167
Results and Discussion	168
Principal Component Analysis	168
Mixture Analysis Using Image Endmembers	173
Mixture Analysis Using Reference Endmembers	189
Selection of Potential Reference Endmembers	189
Spectral Decomposition of AVIRIS Data Using Reference Endmembers	200
Spectral Decomposition of Subsets of AVIRIS Data	203
Conclusions	210
5. SUMMARY AND CONCLUSIONS	212
APPENDIX A: ATREM'S INPUT CARD.....	215
APPENDIX B: PICTURE OF THE LANDSCAPE AND DETAILS OF THE SOIL SURFACE OF THE MCALLISTER SOIL SERIES.....	217
APPENDIX C: PICTURE OF THE LANDSCAPE AND DETAILS OF THE SOIL SURFACE OF THE STRONGHOLD SOIL SERIES.....	219
APPENDIX D: PICTURE OF THE LANDSCAPE AND DETAILS OF THE SOIL SURFACE OF THE GRAHAM SOIL SERIES.....	221

TABLE OF CONTENTS—Continued

	Page
LIST OF REFERENCES	223

LIST OF ILLUSTRATIONS

Figure		Page
2-1	Location of the experimental site	29
2-2	Relative BRF under dry and wet conditions.....	37
2-3	Spectral variation of relative BRF for -30 and 30 degree viewing angles under dry and wet conditions.....	43
2-4	Spectral variation of relative BRF for -30 and 30 degree viewing angles under dry and wet conditions	44
2-5	Effect of viewing angles on soil spectral response under dry condition	47
2-6	Effect of viewing angles on soil spectral response under wet condition ..	48
2-7	Ratios BRF dry/BRF wet for nadir, -30 and 30 degree viewing angles ..	50
2-8	RELAB spectral curves	52
2-9	Relative BRF for RELAB data	55
2-10	Effect of view and sun zenith angles on the relative BRF under dry and wet conditions. Data processed for TM band 1 (0.45 to 0.52 Micrometers).....	61
2-11	The BRF for Epitaph soil compared to the BRF of volcanic rock outcrops	64
2-12	Wavelength dependency of the relative BRF for -30 degree (lines above the unit line) and for 30 degree (lines below the unit line) view zenith angles Sun zenith angle of 30 degree	66
3-1	Irradiance at the top of Earth's Atmosphere and for 1.5 Km elevation as modeled by MODTRAN and convolved to AVIRIS bands	83
3-2	Calibration results for ATREM radiative transfer code	93

LIST OF ILLUSTRATIONS—Continued

Figure		Page
3-3	Comparison between soil spectra obtained from AVIRIS data (ATREM and apparent reflectance), field, sieved samples, and RELAB data (0.45 to 0.90 micrometers)	94
3-4	Comparison between soil spectra obtained from AVIRIS data (ATREM and apparent reflectance) and RELAB data (0.90 to 2.45 micrometers)...	96
3-5	Magnitude of the differences between sieved samples, field, and RELAB as demonstrated by the spectral ratios.....	102
3-6	Soil spectral curves extracted from AVIRIS after smoothing for 0.45 to 0.90 micrometers (upper) and for 0.90 to 2.40 micrometers (below).....	107
3-7	Comparison between the first derivative for AVIRIS, RELAB, field, and sieved samples for the interval 0.45 to 0.90 micrometers	108
3-8	First derivative spectra for Goethite (Sample WS222-USGS), Hematite (Sample GDS76-USGS), and walnut leaf (Sample ABSREF950 -USGS).....	112
3-9	Comparison between the first derivative for AVIRIS and RELAB for the interval 0.90 to 2.40 micrometers.....	116
3-10	Dendogram for field spectra taken at nadir view angle for soils under dry (d) and wet (w) conditions	118
3-11	Dendogram for field spectra taken at -30 degree view angle for soils under dry (d) and wet (w) conditions.....	119
3-12	Dendogram for field spectra taken at 30 degree view angle for soils under dry (d) and wet (w) conditions	120
3-13	Dendogram for sieved sample spectra taken under dry (d) and wet (w) conditions	121

LIST OF ILLUSTRATIONS–Continued

Figure		Page
3-14	Picture of the soil samples used to obtain the sieved sample spectral classes presented in Figure 3-13 The first row represents the bright soils, while the second and the third rows represents the dark soil samples The capital letter D means dry, and W means wet sample.....	125
3-15	Dendograms from clustering RELAB's data set for nadir (a) -35 (b) and 35 (c) degree viewing angles The numbers represent: 1=Stronghold-1, 2=Stronghold-2, 3=Stronghold-3, 4=Baboquivari, 5=Epitaph, 6=Graham, 7=McAllister, 8=Tombstone	126
3-16	Dendogram from clustering RELAB's soil spectral curves for nadir (n), -35 (a), and 35 (f) degree viewing angles	127
3-17	Dendograms showing how the spectral curves were clustered after resample RELAB's data for nadir (a), 35 (b) and -35 (c) degree viewing angles and for field data for nadir (d), 35 (e) and -35 (f) degree viewing angles, respectively The correspondent numbers represents: 1=Stronghold-1, 2=Stronghold-2, 3=Stronghold-3, 4=Baboquivari, 5=Epitaph, 6=Graham, 7=McAllister, and 8=Tombstone	130
3-18	Spectral recomposition and error using one factor for the four soil basic curves	137
3-19	Spectral recomposition and error using two factors for the four soil basic curves.....	139
3-20	Spectral recomposition and error using three factors for the four soil basic curves.....	140
3-21	Spectral recomposition and error using four factors for the four soil basic curves	142
3-22	Dendograms resulting from clustering RELAB's data for 340 bands (a), average from each one of the spectral range shown in Table 3-7 (b), and using the four key bands given by the four factor model (c) The numbers represent: 1=Stronghold-1, 2=Stronghold-2, 3=Stronghold-3, 4=Baboquivari, 5=Epitaph, 6=Graham, 7=McAllister, 8=Tombstone	144

LIST OF ILLUSTRATIONS–Continued

Figure		Page
3-23	Spectral curves considering the four key bands for the four basic soil curves	146
4-1	Soil map of the area of the Walnut Gulch Experimental Watershed imaged by AVIRIS	159
4-2	First (a), and second (b) component images	170
4-3	Third (a), and fourth (b) component images	172
4-4	Fifth (a), and sixth (b) component images	174
4-5	The first six abstract eigenspectrum curves following the decomposition of AVIRIS image using PCA	175
4-6	Dendogram obtained after applying cluster analysis to the average spectra extracted for each soil from AVIRIS imagery	177
4-7	Spectral curves for each of the selected image endmembers	179
4-8	Error image after applying mixture analysis using image endmembers ...	180
4-9	McAllister (a) and Stronghold-3 (b) fraction images	182
4-10	Graham/Shade (a), and green vegetation (b) fraction images	183
4-11	Color coded maps presenting the distribution of the fractions for McAllister (a) and for Graham/Shade (b) image endmembers.....	186
4-12	Color coded map presenting the distribution of the fractions for Stronghold-3 image endmember	187
4-13	Scaled fraction images and color coded fraction images (A) Fraction image with shade; (B) Fraction image without shade; (C) Color coded fraction image with shade; (D) Color coded fraction image without shade The legend for colors is the same as for Figure 4-11	188

LIST OF ILLUSTRATIONS--Continued

Figure		Page
4-14	Field spectral curves for potential reference endmembers others than soils	191
4-15	Target test results for McAllister and Stronghold-3 soils	194
4-16	Target test results for Graham soil and dry forbes	195
4-17	Target test results for litter and dry grass	196
4-18	Target test results for bear grass and walnut leaf	197
4-19	Fraction images obtained using McAllister (a) and Graham (b) reference endmembers	201
4-20	Fraction image obtained using green vegetation (Walnut leaf) reference endmember	202
4-21	Spectral pixel recomposition (a) and reference endmember fractions (b) for the subset of pixels used as McAllister image endmember	205
4-22	Spectral pixel recomposition (a) and reference endmember fractions (b) for the subset of pixels used as Stronghold-3 image endmember	206
4-23	Spectral pixel recomposition (a) and reference endmember fractions (b) for the subset of pixels used as Graham image endmember	207
B1	Landscape of the McAllister soil series	218
B2	Details of the surface of the McAllister soil series	218
C1	Landscape of the Stronghold soil series	220
C2	Details of the surface of the Stronghold soil series	220
D1	Picture of the landscape and details of the soil surface of the Graham soil series	222

LIST OF TABLES

Table		Page
2-1	Soil Series and classification at the family level.....	30
2-2	Soil physical and chemical analysis.....	32
2-3	Day of the year (DOY), time and average sun angle for each field measurements of BRF	35
2-4	Roughness index	58
2-5	Characterization of the percent of cover in the roughness experiment	60
3-1	General Performance of AVIRIS (Goetz, 1992)	78
3-2	Eliminated channels from the original AVIRIS image of the Walnut Gulch Experimental Watershed	79
3-3	Percent of cover type in the transect of each soil	98
3-4	NDVI and SAVI values for the field samples. Field spectral response were convolved to TM and AVIRIS bands	114
3-5	Eigenvalue analysis for 340 bands (from RELAB data set) measured in 8 soil samples	133
3-6	Influence of the number of factors on the ten largest errors present in the reconstructed matrix. Soil numbers are: 1=McAllister, 2=Baboquivari, 3=Graham, 4=Stronghold-1, 5=Epitaph	134
3-7	Results of clustering 340 spectral bands using the option for 4 factors. Data from RELAB's soil spectra for nadir view angle	143
4-1	Comparison between supervised maximum likelihood classifier and mixture modeling.....	156
4-2	Spectral library utilized for the identification of potential reference endmembers.....	166
4-3	Summary of the principal component analysis for the first 6 components	169

LIST OF TABLES (Continued)

Table		Page
A1	Details of the input card for the ATREM radiative transfer code	216

ABSTRACT

The research objectives of this study were formulated to produce the soil spectral maps using spectral mixture analysis on the AVIRIS data of the Walnut Gulch Experimental Watershed, Tombstone, Arizona. To accomplish this objective the spectral characteristics of eight soils of this Watershed were determined considering the effect of the source of illumination/sensor viewing geometry, degree of wetness (dry vs wet), surface roughness, and the source of the spectra (field, sieved samples and lab) on the selection of image and reference endmembers. The scale effect of the source of spectra was also studied in connection with AVIRIS spectral response. The soils presented anisotropic behavior which varied inversely with the wavelength, and it was reduced under wet conditions. Loss of information occurred when moving from large scale data set (lab, sieved sample, and field spectra) to small scale data (AVIRIS).

Cluster analysis and factor analysis were used to extract information about how soil reference endmembers are grouped in relation to viewing angles, degree of wetness and the source of the spectra. Factor analysis was applied to identify the key set of bands that carried most of the information. Soil spectral classes varied as a result of scale effects, soil conditions (wet or dry), and viewing angles. Factor analysis showed that with four unique bands (located at 0.410, 1.310, 0.650, and 2.400 μm) it was possible to reconstruct the four basic soil spectral curves (Epitaph, Graham, McAllister, and Baboquivari) from the lab ~~data~~ set.

AVIRIS image was modeled using mixture analysis on the basis of image endmembers and reference endmembers. Based on the four dimensions of the AVIRIS data image endmembers were defined by three soil spectra (McAllister, Stronghold-3, and Graham) and by one spectra of green vegetation.

The shade fractions were separated from dark soils (Graham and Epitaph) on the basis of the spatial context. The target test identified at least seven reference endmembers in the AVIRIS scene of the Watershed however; mixture analysis failed in obtaining fraction images from these reference endmembers. Mixture analysis was able to produce fraction images with a relatively high error for a small set (3) of reference endmembers (McAllister and Graham soils, and walnut leaf). However when applied to a subset of pixel extracted from the AVIRIS image mixture analysis identified the reference endmembers and quantified their proportions.

CHAPTER 1

INTRODUCTION

Introduction, Objectives, and Statement of the Problem

As a natural resource involved in many processes, the soil is seen as a decisive component of different ecosystems that enables life to survive on the Earth's environment. Although soil is considered a nonrenewable natural resource in terms of a human life span (Jenny, 1980), currently its loss is estimated at 5 to 7 million hectares of arable land (0.3 to 0.5 % of the total arable land on Earth) every year through soil degradation (Lal and Stewart, 1992). Soil degradation is seen as a threat to food production (Brink et al., 1977) as well as a major player in the changes of the global carbon budget (Tang et al. 1990). To overcome the challenges of good soil management for preserving agroecosystems and natural ecosystems, we need to find ways to better characterize the soil system in space and time (i.e., soil mapping and monitoring). Airborne and spaceborne sensors have the capability of covering large areas (synoptic view) repeatedly in a short time and this gives to remote sensing important tools for monitoring and mapping soils. In fact, one of the driving forces in the study of soil spectral characteristics has been the need to improve our capabilities to inventory and monitor soil resources. Although optical remote sensing of soils produces spectral results only for a few millimeters of soil depth, this layer of soil is also responsible

for many of the important soil properties that is directly related to biosphere processes. Thus, most of organic carbon, nitrogen and other nutrients directly or indirectly derived from the soil organic matter come from this thin layer of soil.

Soil spectral characteristics can be considered a cumulative property which is derived from inherent spectral behavior of the heterogeneous combination of mineral, organic, and fluid matter that comprises mineral soils (Stoner and Baumgardner, 1981). It is well known, however, that naturally occurring surfaces have widely varying reflection properties, the variation being in terms of both total reflectance and the dependence of reflectance on wavelength, angle of incidence, angle at which the surface is viewed, and the physical character (such as surface roughness) of the surface itself. Besides the influence of these factors for the inherent complexity of soil spectra, another factor that must be taken into account when interpreting remotely-measured spectra of soils is that this spectra are collected from mixtures of materials which commonly include vegetation, shade, litter and rocks in different proportions for each pixel in a scene. Spectral mixtures of soils and these other materials arise at nearly every scale of remote sensing data and are difficult to interpret. To overcome the natural occurrence of mixed spectral signals from soil surfaces a technique called mixture analysis has been applied to decompose measured spectra from experimental data or pixels into the spectra of their reflecting components. This technique, however, has been applied without a previous evaluation of the anisotropic behavior of natural surfaces

such as soil. As a result of the anisotropic behavior of most of soil surfaces bidirectional reflectance factor (BRF) characterization is an invaluable instrument for mapping and monitoring soil processes. Thus, the investigation of how soil spectral classes change as a function of BRF can lead to a better understanding of mapping soils using remotely sensed data.

Another important aspect is that much of the remote sensing information about soils has come from multispectral images having only a few bands (e.g., Landsat). With the advent of new detectors and other technological advances, it is possible today to image soils in hundreds of narrow channels in the wavelength region from about 0.4 to 2.5 μm (e.g., the Airborne Visible-Infrared Imaging Spectrometer (AVIRIS)). These "hyperspectral" imaging systems make possible "imaging spectroscopy" that is, spectroscopy in a spatial context (Adams, et al., 1993). The amount of information added by a hyperspectral data set taken from soil surfaces, however, needs to be analyzed for different scales and in the context of spectral mixtures. It is also important to know if adding dimensionality by using hyperspectral data sets really makes a difference for soil spectral characterization and soil spectral classification.

As reviewed by Irons et al. (1987) remotely sensed data have been used for soil mapping since the 1920's in the form of black-and-white aerial photographs. Since then many researches have been using remote sensing for soil mapping (May and Petersen, 1975; Westin and Frazee, 1976). Kristof and Zachary (1971) have pointed out, however, that identification of soils at the level of soil series using remotely sensed data is not possible because both surface and subsurface properties differentiate series. New techniques such as image

spectroscopy, off-nadir view angle (BRF studies), and the use of sub-pixel analysis, which can isolate the spectral contribution of other types of cover (such as different types of vegetation, (that could be associated to specific types of soils), could be very helpful in mapping soils at the scale of soil series. These new techniques are still not used for mapping soils at that scale level.

The primary objective of this study was to produce the soils spectral map of the Walnut Gulch Experimental Watershed using spectral mixture analysis (SMA) on AVIRIS data. Other objectives were: a) To characterize BRF soil surfaces of the Walnut Gulch Experimental Watershed (Tombstone - AZ); b) To compare soil spectral information obtained at different scale levels; c) To evaluate the dimensionality of the soil spectra obtained at the Walnut Gulch Experimental Watershed in terms of soil spectral classes and "key" bands; d) To decompose the AVIRIS scene of the Walnut Gulch Experimental Watershed in terms of its main constituents (endmembers).

Overview of the Dissertation

Besides this introductory Chapter this dissertation is composed of four other chapters. Chapter 2 presents the lab and field BRF characterizations of the main soils present at the Walnut Gulch Experimental Watershed in relation to wet conditions and surface roughness. The soil spectral library generated in Chapter 2 constitutes the basic soil information for the other Chapters in this dissertation. Chapter 3 uses this information and compares it to the AVIRIS calibrated signal in order to see the scale effect on soil information extraction. Also in Chapter 3, we studied the dimensionality of the field and lab spectra in terms of soil spectral

classes and "key" bands using data reduction techniques such as cluster analysis and factor analysis.

In Chapter 4 the AVIRIS scene of the Walnut Gulch Experimental Watershed was decomposed in terms of image endmembers and a subset of this image are decomposed in terms of reference endmembers. The soil spectral maps from mixture analysis are also generated in this chapter. Chapter 5 presents the summary and conclusions

CHAPTER 2

SOIL SPECTRAL RESPONSE IN RELATION TO SENSOR VIEWING ANGLE, SOIL MOISTURE, AND SURFACE ROUGHNESS

Introduction

Early work of Coulson (1966) and Coulson et al. (1965) have pointed out the anisotropic behavior of some soil surface, desert sand (gypsum) and beach sand (quartz) when viewed from different sources of illumination/sensor viewing angle geometry. Coulson (1966) studied the spectral behavior of various materials, under lab conditions, in the principal plane for view angles varying from 0 to 80 degrees in both direction (backscattering and forward scattering). Under these conditions he found that particulate material having low absorption, such as desert sand (gypsum) and white quartz beach sand, present high reflectance values in the forward direction with a peak at a view zenith angle greater than the zenith angle of specular reflectance. On the other hand, red clay soils and loamy soils presented low reflectance values when the sensor was located in the forward scattering direction while the maximum reflectance occurred in the backscattering or antillumination direction. The pronounced reflectance peak in the backscattering direction was associated with highly absorbing materials, such as clayey and loamy soils. Coulson (1966) attributed the observed peak in reflectance values in the backscattering direction to the effects of mutual shadowing among particles. Thus, considering the phase angle (i.e., the angle between the source of

illumination direction and the view direction) reflectances usually decrease as we move away from the antillumination or backscattering to the forward scatter direction for most soil surfaces because the increase in the proportion of shadowed area. A sensor does not view shadows if and only if the sensor views a particulate from the backscattering direction. Moving from the peak in the backscattering direction toward the forward scattering direction, the increase in viewed shadow is rapid at first and then slows. The degree to which a given surface material absorbs radiation also plays a role in the anisotropic behavior of soils. Thus, materials, such as quartz, having low absorption shadows are softened by light that is multiply scattered or transmitted through particles. This softening of shadows tends to decrease reflectances in the backscattering direction by low-absorption materials (Irons, 1987)

Soil reflectance has also been measured as a function of sun/sensor viewing geometry in the field. Under these conditions, Eaton and Dirmhirn (1979) found results similar to that of Coulson (1966) for a plowed silty clay loam soil. These authors attributed the peak in the backscattering direction to the pronounced roughness of the soil surface and the resultant shadows. Coulson and Reynolds (1971) observed soil hemispherical reflectance under varying solar zenith angles. Hemispherical reflectance maxima were found at solar zenith angles between 70 and 80 degrees. Kimes (1983), Kimes and Sellers (1985), and Kimes et al. (1985) have observed the bidirectional reflectance of bare fields from multiple-view zenith and azimuth angles in their studies of plant-canopy reflectance. Irons and Smith (1990) studied the effect of surface roughness in a loam soil tilled with different implements in order to obtain a smooth, moderate, and rough soil surfaces. A drop pin device was used to characterize the three levels of surface roughness. The smooth surface presented a root mean

square (RMS) pin height of 1.1 ± 0.2 , while the moderate and rough presented 2.6 ± 0.5 , and 3.6 ± 0.2 RMS pin height, respectively. Irons and Smith (1990) found that the k value of the Minnaert function had the highest dependence for the roughest surface. The dependence of k value of the Minnaert function was not only attributable to the surface roughness but also to the shape and orientation of surface clods. Jackson et al. (1990) studied the effect of varying the sun/sensor viewing geometry in clay loam soil with different degrees of roughness: (a) laser-leveled; (b) tilled with a disc plow; (c) chisel plowed. Under any condition the scattered radiation was higher in the backscattering direction. At 44 degrees Jackson et al. (1990) found that the laser-leveled and the disc plow treatments scattered radiation in a similar way; however, the roughest surface (chisel plowed) presented a stronger response toward the backscattering direction. These studies demonstrated the importance of surface roughness in determining the directional distribution of soil reflectance in the field.

When water is added to soil, the general effect is a reduction in the reflected radiation in the spectral interval between 0.4 and 2.6 μm (Hoffer and Johannsen, 1969; Bowers and Hanks, 1965; Curran et al. 1990; Epiphany et al. 1992). As a result a given soil will appear darker when moist than when dry. Planet (1970) pointed out that differences in the reflected radiation when a given soil is wetted can be attributed the following reasons: (a) changes in refractive index due to soil solution; (b) changes in physical properties of soil particulate due to the presence of water; and (c) similar values for the refractive index of water (1.33) and the refractive index of soil minerals (about 1.5). Although some authors (Curran et al., 1990) had mentioned that moist soils have presented reduction in reflectance by a factor of 2 to 3, marked alteration in spectral curve shape after wetting had not been reported. The general

reduction in reflectance for moist soils has also been found to be dependent on the soil surface color (Curran et al., 1990; Epiphonio et al., 1992). Sadovnikov and Orlov (1978) cited by Curran et al. (1990) found that the effect of moist humus-accumulating horizons was higher for yellow and red soils. In a study conducted over 111 samples of tropical soils Epiphonio et al. (1992) found the less soil albedo, the less the variation between soil reflectance under dry and wet conditions. Hence, dark red Oxisols presented relatively less reduction in reflectance values after wetting than light red Oxisols.

Although a great deal of research has been done to characterize bidirectional reflectance factors for vegetated areas, only a few papers have dealt with the bidirectional reflectance factors for bare soils under dry and, mainly, under wet conditions. Most of these papers have shown that the directional distribution of solar radiation scattered from bare soil is generally anisotropic (Irons et al. 1987; Kimes et al. 1985; Eaton and Dirmhirn, 1979; Salomonson and Marlatt, 1971). However, most do not show how the anisotropic behavior is affected when the soil is wetted. On the other hand, the great majority of field studies that relate surface roughness to the anisotropic behavior of soil have been done by plowing the soil surfaces. Few, if any, studies have been done under natural conditions for bare soils, where interactions between the spectral properties of rocks and the underlying soil could play a major role. As Irons et al. (1991) pointed out, the anisotropic behavior of bare soil has several significant consequences, among them the fact that directional distributions of soil reflectance potentially carry information on soil properties such as moisture content, organic matter content, iron-oxide content, mineralogy, particle size distribution, and surface roughness.

Considering that factors such as the sensor/source of illumination viewing geometry, wet conditions, and surface roughness affect the spectral response of soils, and, consequently, have potential effects on the soil spectral map of the Walnut Gulch Experimental Watershed produced by mixture models, questions proposed for this chapter are: (a) What does soil spectra look like; (b) Are there significant differences between soil spectra obtained for different sensor viewing angles; (c) What do differences look like when compared among soils; (d) Is the anisotropic behavior of the soils the same for different wavelengths; (e) How does wetness affect the soil spectral responses under different viewing geometry; (f) What is the effect of the surface roughness on soil spectral response for different sensor/viewing geometry, and wet conditions ?

To answer these questions we propose to characterize the dynamics of soil directional reflectance factor distributions as a function of wavelength, view angle, soil surface wetness and soil surface roughness.

Methods

BRF measurements were made over six soil series within the Walnut Gulch Experimental Watershed in southeastern Arizona (31.7°N - 110.1°W). The area sampled is in the portion of the AVIRIS scene taken on May 14, 1991 (Figure 2-1). The soil samples and classification at the family level for the six soil series are presented in Table 2-1. These are the most representative soil series in the area imaged by AVIRIS and together they represent more than 90 percent of the area imaged by AVIRIS. The fact that we have differences in

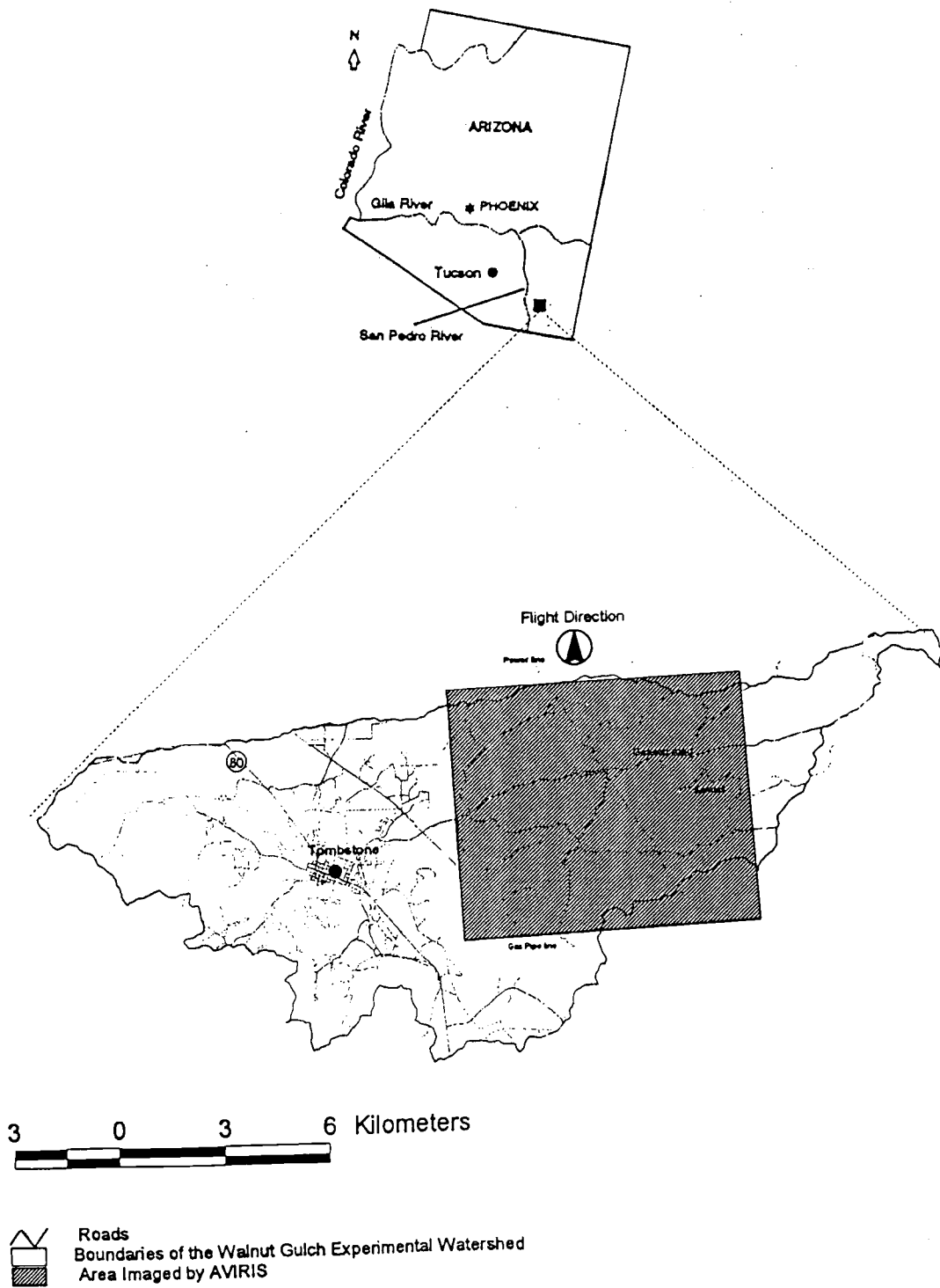


Figure 2-1. Location of the experimental site

Table 2-1. Soil series and classification at the family level

Soil Series	Classification at the family level
Baboquivari	Fine-loamy, mixed, thermic Ustollic Haplargids
Epitaph	Fine, montmorillonitic, thermic Leptic Haplotorrerts
Graham	Clayey, montmorillonitic, thermic Lithic Ustollic Haplargids
McAllister	Fine-loamy, mixed, thermic Ustollic Haplargids
Stronghold	Coarse-loamy, mixed, thermic Ustollic Calciargids
Tombstone	Loamy-skeletal, mixed, thermic shallow Ustollic Calciargids

vegetation cover in the Stronghold series leads to the use of three different locations, designated as: Stronghold-1, Stronghold-2, and Stronghold-3. In Stronghold-1 forbes dominates the vegetation. In Stronghold-2 shrubs, Creosotebush (*Larrea tridentata*), are the main vegetation, while in Stronghold-3 dry shrubs and some grass are mixed and constitute the dominant vegetation in this area of the AVIRIS image. Table 2-2 presents some of the physical and chemical characteristics of each soil. Description of the surface roughness measurements is given at the end of this methodology.

Robinson and Biehl (1979) defined a reflectance factor as "the ratio of the radiant flux actually reflected by a sample surface to that which would be reflected into the same reflected beam geometry by an ideal (lossless) perfectly diffuse (Lambertian) standard surface irradiated in exactly the same way as the sample". Once the reflectance properties of the standard surface (reference panel) are known, one can obtain the reflectance properties of a given target nearly independent of the sky conditions at the time of the measurement. The procedure in the field consists in measuring the response V_s of the instrument viewing the target and then measuring the response of the instrument viewing a leveled reference plate (V_r). An approximation of BRF is given by:

$$BRF_s(\theta_i, \phi_i, \theta_r, \phi_r) = \frac{V_s}{V_r} BRF_r(\theta_i, \phi_i, \theta_r, \phi_r) \quad 2.1$$

Where θ_i , θ_r and ϕ_i , ϕ_r are the source of illumination, and reflected beam zenith and azimuth angles, respectively. The bidirectional reflectance factor for the plate (BRF_r) is determined

Table 2-2. Soil physical and chemical analysis

Soil Unit	Particle Size (%)			Organic Carbon (%)	Total Iron (%)	Color - Chromameter						Roughness (Relative arc length)
	Sand	Silt	Clay			Dry			Wet			
						Hue	Value	Chroma	Hue	Value	Chroma	
Baboquivari	75	14	11	0.3	1.33	4.50	4.80	2.73	4.23	3.59	2.49	1.02
McAllister	68	20	12	0.32	1.61	3.84	4.41	4.50	3.67	3.42	3.59	1.11
Stronghold-1	85	12	3	0.56	1.11	4.63	4.91	2.79	4.41	3.53	2.55	1.07
Graham	67	8	25	0.97	1.73	4.85	4.25	2.06	4.28	2.98	2.00	1.14
Stronghold-2	70	18	12	0.39	1.51	4.50	4.85	2.55	4.15	3.48	2.31	1.08
Epitaph	35	39	26	0.4	1.97	4.45	3.81	2.73	4.06	2.98	2.43	1.18
Stronghold-3	68	17	15	1.08	1.42	4.50	5.35	2.55	4.23	3.75	2.43	1.15
Tombstone	70	15	15	0.86	1.05	4.54	4.80	2.55	4.19	3.53	2.37	1.08

in lab conditions and is needed in order to correct for departures in lambertian properties of the reference plate.

The bidirectional reflectance factors were measured in the dry seasons of 1995 and 1996 during the months of May and June. Sites for assessment of the bidirectional reflectance factor were selected in a way so that almost no other constituent besides bare soil were present in the field of view of the instrument. Small vegetation (such as forbes) represented, in all sites, less than 5% of the field of view of the instrument. For each soil, bidirectional reflectance factors were measured first under dry conditions and then the soil were wetted to take wet measurements of the bidirectional reflectance factor.

Fine resolution spectra were obtained with an SE590 Spectron spectroradiometer (0.45-0.90 μm in 0.01 μm or 10 nm sampling interval) with 15° field of view and mounted 2.3 m above the ground on a BRF apparatus (Jackson et al., 1990). The BRF apparatus was designed to measure radiances from exactly the same spot for all view angle settings in a given plane. The device can be adjusted manually to provide view angles from -45° to +45° from the vertical in 5° increments. Reflectance factors were measured along the principal plane. Kimes et al. (1984) mentioned that the principal plane contained the maximum information about the physical characteristics of a scene (which included bare soil surfaces).

Measurements were made from view angles starting at -45° and proceeding to +45° in 5° view angle increments. This sequence was then repeated in reverse from +45° to -45°, and the pair of measurements for each view angle was averaged. Readings from a calibrated, horizontal spectralon panel were recorded immediately before and after each measurement sequence. The entire sequence of panel and target readings required 10 minutes to complete

for dry or wet condition. BRF measurements for wet soil were made right after the dry measurement for a given soil. An average of 20 minutes were spent for the entire series of measurements for each soil.

Table 2-3 presents the variation in sun angle for the BRF measurements in each soil and wet condition. All angles in the antisolar viewing direction were assigned negative values while angles in the forwardscatter direction were assigned positive values. The data from the Spectrun instrument were convolved and processed for TM bands 1 (0.45 - 0.52 μm), 2 (0.52 - 0.60 μm), 3 (0.63 - 0.69 μm), and 4 (0.76 - 0.90 μm) with reflectance factors calculated by ratioing the "averaged" view angle response by the nadir view angle response from the reference panel, that had known reflectance properties as a function of sun angle. In the case of the roughness experiment the BRF was measured for 50, 40, and 30 degrees solar zenith angles.

Sieved samples (crushed to pass in a 2 mm sieve) of each of the soils were also sent to the Reflectance Experiment Laboratory (RELAB) at Brown University. The RELAB's spectra were obtained only for samples under air dry conditions for the region from 0.4 to 2.5 μm with a sample interval of 0.005 μm or 5 nm. The RELAB spectrometer measures bidirectional reflectance at user-defined phase angles with reference to a pressed halon standard. RELAB's procedure used a quartz halogen lamp as the source of radiation and pressed halon as the reference standard. More details on the bidirectional spectrometer used to obtain the spectra of each soil series is presented in RELAB manual (1993). To allow comparisons with field results, RELAB's measurements were made for nadir, -35° (antillumination direction) and 35° (forward scattering direction) in the principal plane, and

Table 2-3. Day of the year (DOY), time and average sun angle for each field measurement of BRF.

Soil	DOY	Average Decimal Time	Average Sun Angle (Decimal degrees)
Baboquivari (dry)	166	9.97	32.54
Baboquivari (wet)	166	10.15	30.22
Epitaph (dry)	168	10.01	31.33
Epitaph (wet)	168	10.24	29.17
Graham (dry)	170	9.97	32.36
Graham (wet)	170	10.16	30.34
McAllister (dry)	152	9.98	32.34
McAllister (wet)	152	10.28	28.55
Stronghold-1 (dry)	142	9.96	32.96
Stronghold-1 (wet)	142	10.19	30.17
Stronghold-2 (dry)	169	10	32.34
Stronghold-2 (wet)	169	10.2	29.71
Stronghold-3 (dry)	181	9.93	33.78
Stronghold-3 (wet)	181	10.15	31
Tombstone (dry)	145	10.17	30.24
Tombstone (wet)	145	10.37	27.79

an illumination zenith angle of 25° .

Soil surface roughness was measured by using a microroughness meter (Simanton, et al. 1971). The device (described in detail by Simanton, et al., 1971) is a drop pin device composed of 100 pins vertically orientated so that when dropped onto the soil surface creates a continuous profile of pin tops. The profile was drawn on chart paper and the lines were digitized and processed to give a roughness index for each soil surface. The result is expressed in terms of relative arc length which was the ratio between the length of the line drawn following the pins and the length of an horizontal line (1.00 m). Ten profiles were obtained for each soil surface following the direction of the principal plane of the sun. The percent of cover were also measured for each roughness profile (Simanton, et al., 1971). Rock fragments were measured following the criteria presented by the Soil Survey Manual (Soil Survey Division Staff, 1993)

Results and Discussion

Field Spectra

Processed data for TM bands are presented in Figure 2-2 in terms of bidirectional reflectance factors relative to nadir reflectance factor and referred to as relative BRFs (Jackson et al.1990). All soil series under dry conditions presented a strong anisotropic response not symmetric about the nadir. Reflectance values were higher for higher view angles in the backscattering direction and gradually decreased in the forwardscattering direction with lower values for higher positive viewing angles. The relative BRFs show that

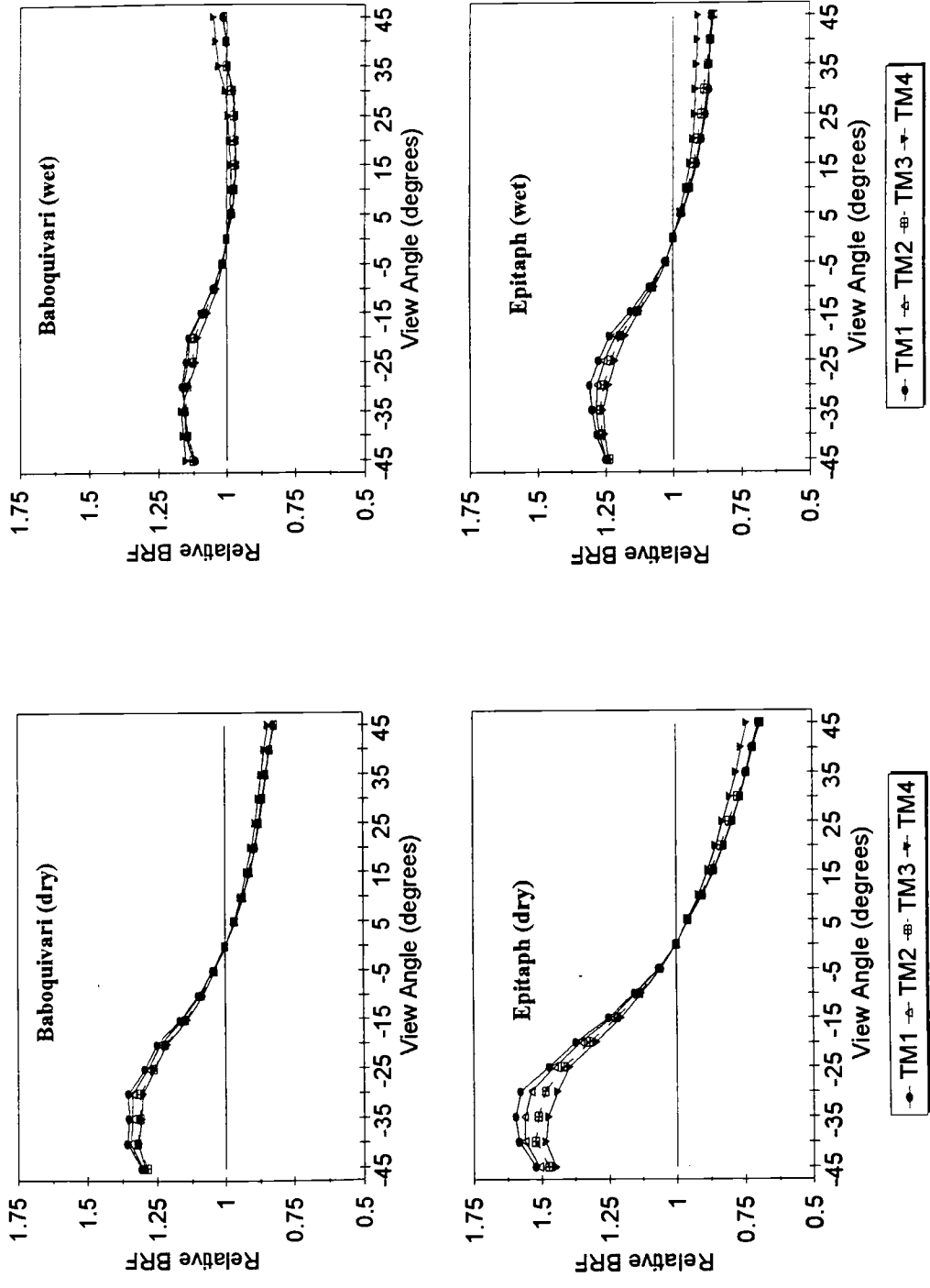


Figure 2-2. Relative BRP under dry and wet conditions

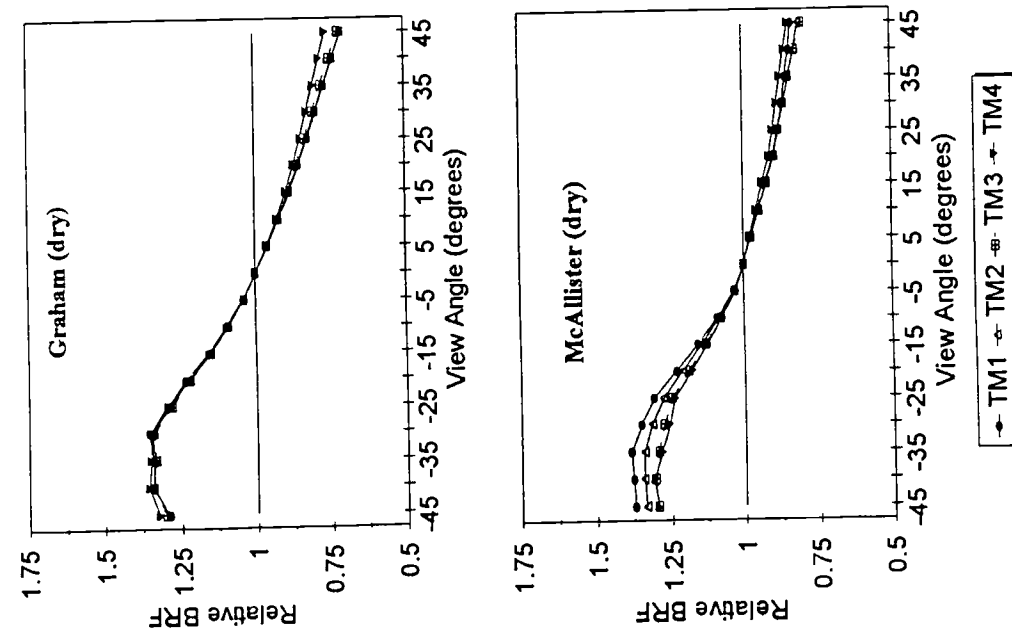
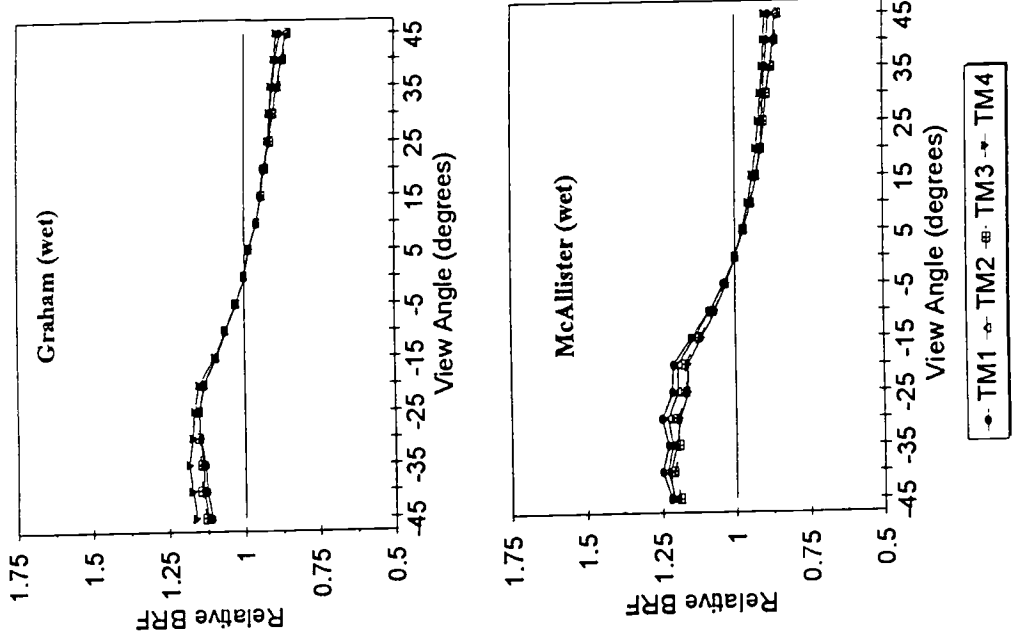


Figure 2-2. Relative BRP under dry and wet conditions (cont.)

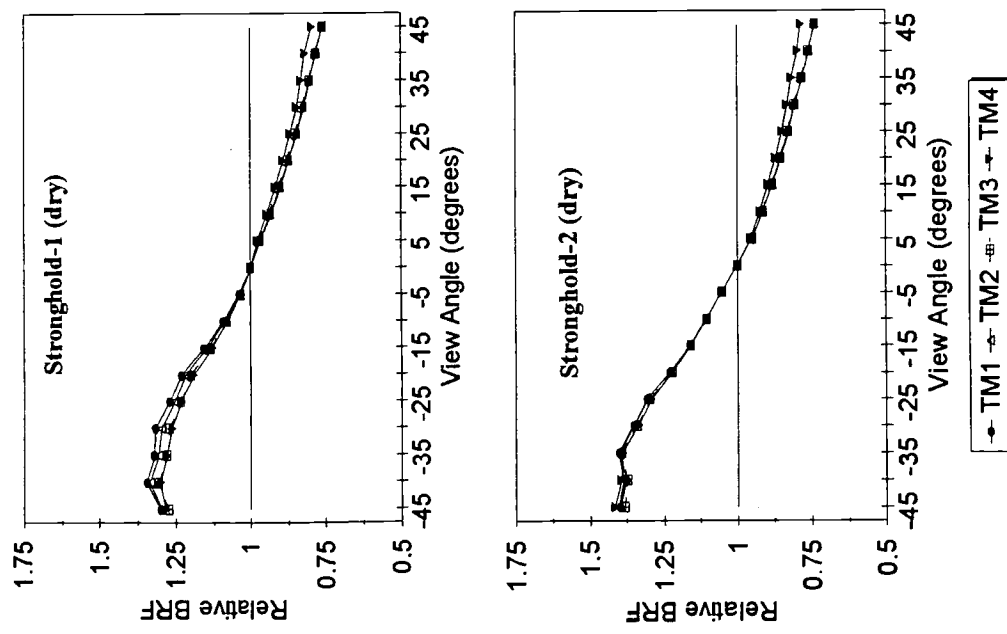
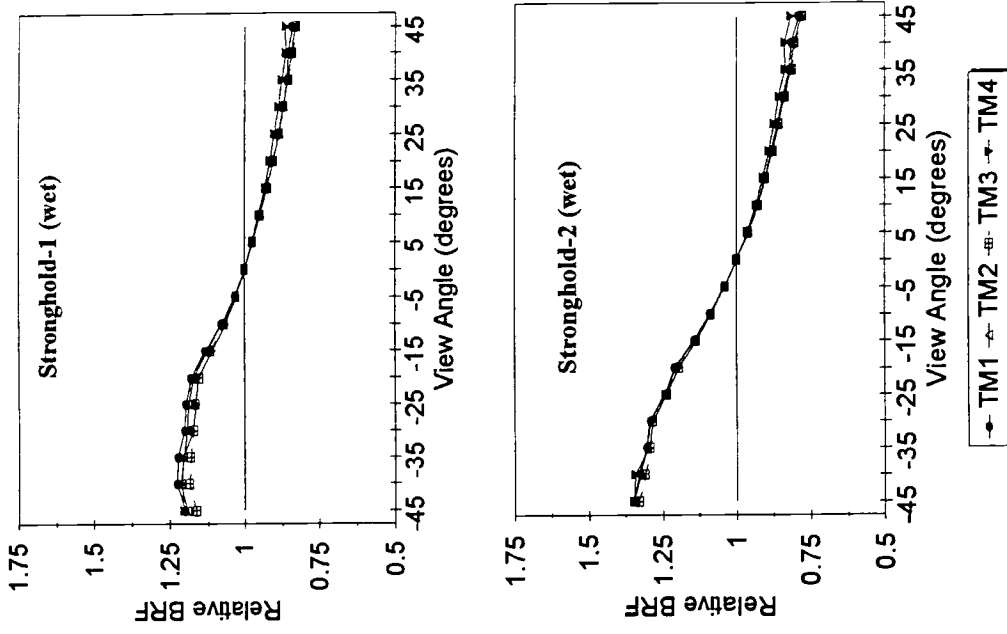


Figure 2-2. Relative BR/PI under dry and wet conditions (cont.)

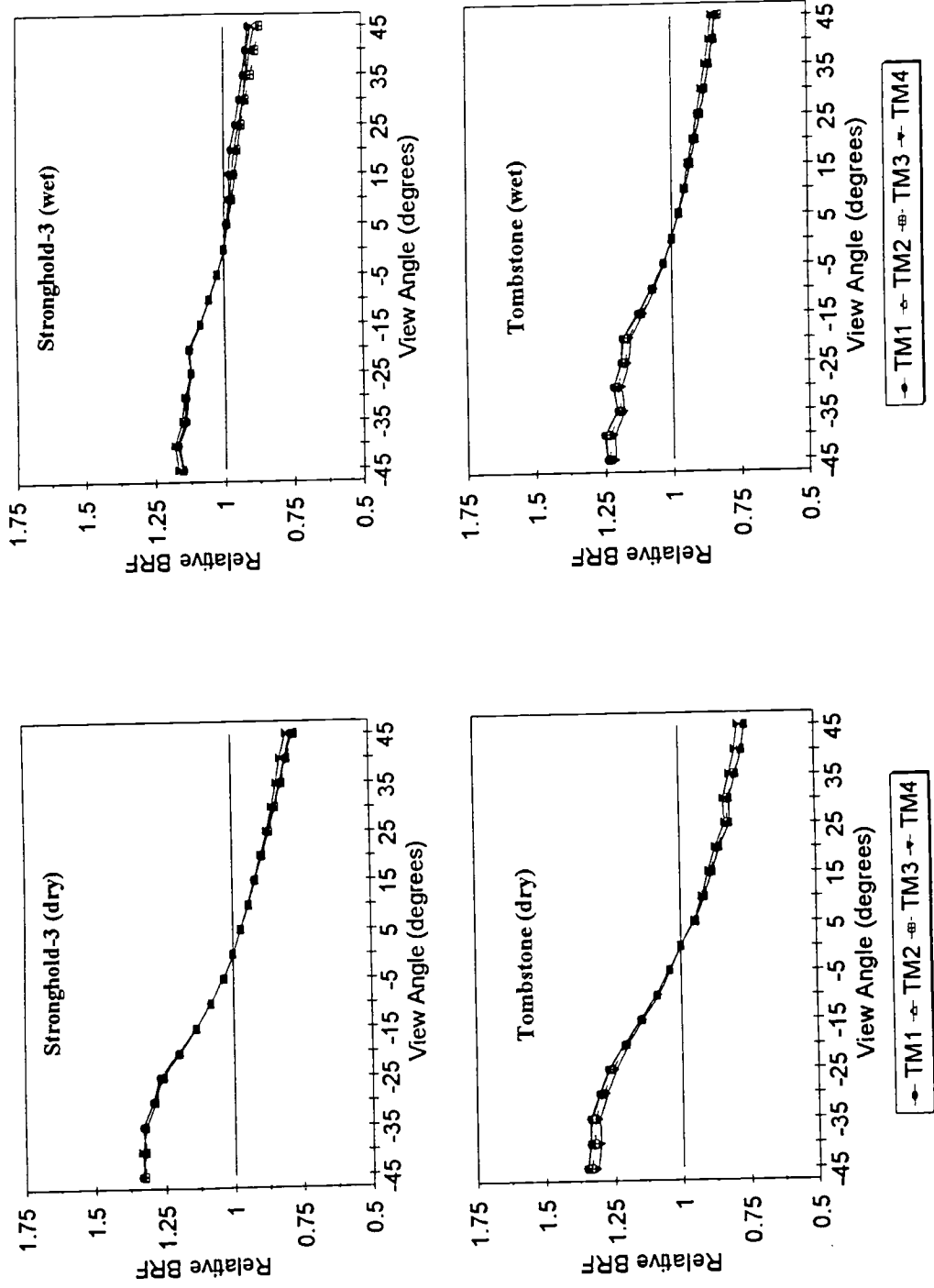


Figure 2-2. Relative BRP under dry and wet conditions (cont.)

the view angle affected reflectance values in the same proportion for all four TM bands in most soils but Epitaph.

Relative BRF values decreased substantially when the soils were wetted. The general effect was to flatten the curves for all soils in the four bands when compared with the curves for dry soil conditions. Under dry conditions for all eight soil samples and for all four TM bands, relative BRF increased from nadir toward the negative angles (backscattering region). A reflectance peak was found in the region between -30 and -40 degrees for all eight soils and for all bands. However, for some soils, such as Stronghold-2, Stronghold-3 and Tombstone, this peak is not as clear since the curve becomes rather flat with no evidence of an inflection point.

For positive view angles the relative BRF decrease gradually from 0 to 45 degrees: the higher the positive view angle, the less the value for the relative BRF. The highest anisotropic behavior was found for dry Epitaph soil. For this very cobbly loam soil, reflectance values for the -35 degrees view angle were about 1.6 times that found for the nadir view angle. The highest anisotropic behavior of Epitaph soil could be associated to its highest surface roughness (Table 2-2). On the other hand, for higher positive view angles, Epitaph soil presented reflectance values of only 0.6 times that for nadir view angle. For the other 7 soils under dry conditions the relative BRF curves presented almost the same anisotropic behavior with reflectance values varying from 1.4 to 0.75 times that were found for the nadir view angle.

Under wet conditions all eight soils presented a tendency to flatten the curves (less anisotropy). Except for Stronghold-2 and Epitaph soils, the relative BRF values increased

rapidly from 0 to -15 degrees and then reduced the increase with an almost flat curve from -20 degrees.

When comparing dry conditions the peak of reflectance moved toward smaller view angles due to the effect of the reduced solar zenith angle (see Table 2-3). Thus the peak or hot spot for Baboquivari, McAllister and Epataph soils, which was found at approximately -35° under dry conditions, moved to -30 degrees under wet conditions.

The relative BRF was calculated for the entire range of the SE590 Spectron instrument (0.45 to 0.90 μm) for -30° and 30° and the results plotted in the graphs presented in Figures 2.3 and 2.4 for dry and wet conditions, respectively. The reason for choosing -30 and 30 degrees was to compare the response in the backscattering and forward scattering directions. Also, for approximately -30 degrees, all soil series presented a peak (hot spot) for the relative BRF.

Dry condition. Under dry condition except for Epataph soil series for a given wavelength the relative BRF presented little variation either for -30 or 30 degrees view angle when compared with the remaining 7 soils. The relative BRF presented were almost constant throughout the measured spectrum for both -30 degrees (backscatter direction) and 30 degrees (forwardscatter direction) view angle for all soils but McAllister, Epataph and in less extension Stronghold-1. For McAllister and Epataph the relative BRF for -30 degrees decreased continuously from 0.45 μm through 0.90 μm . Under dry condition and for -30 degrees view angle for Epataph soil, the relative BRF varied from 1.6 for 0.45 μm to 1.4 for 0.90 μm . For McAllister this variation was from 1.35 to 1.25 for 0.45 and 0.90 μm , respectively.

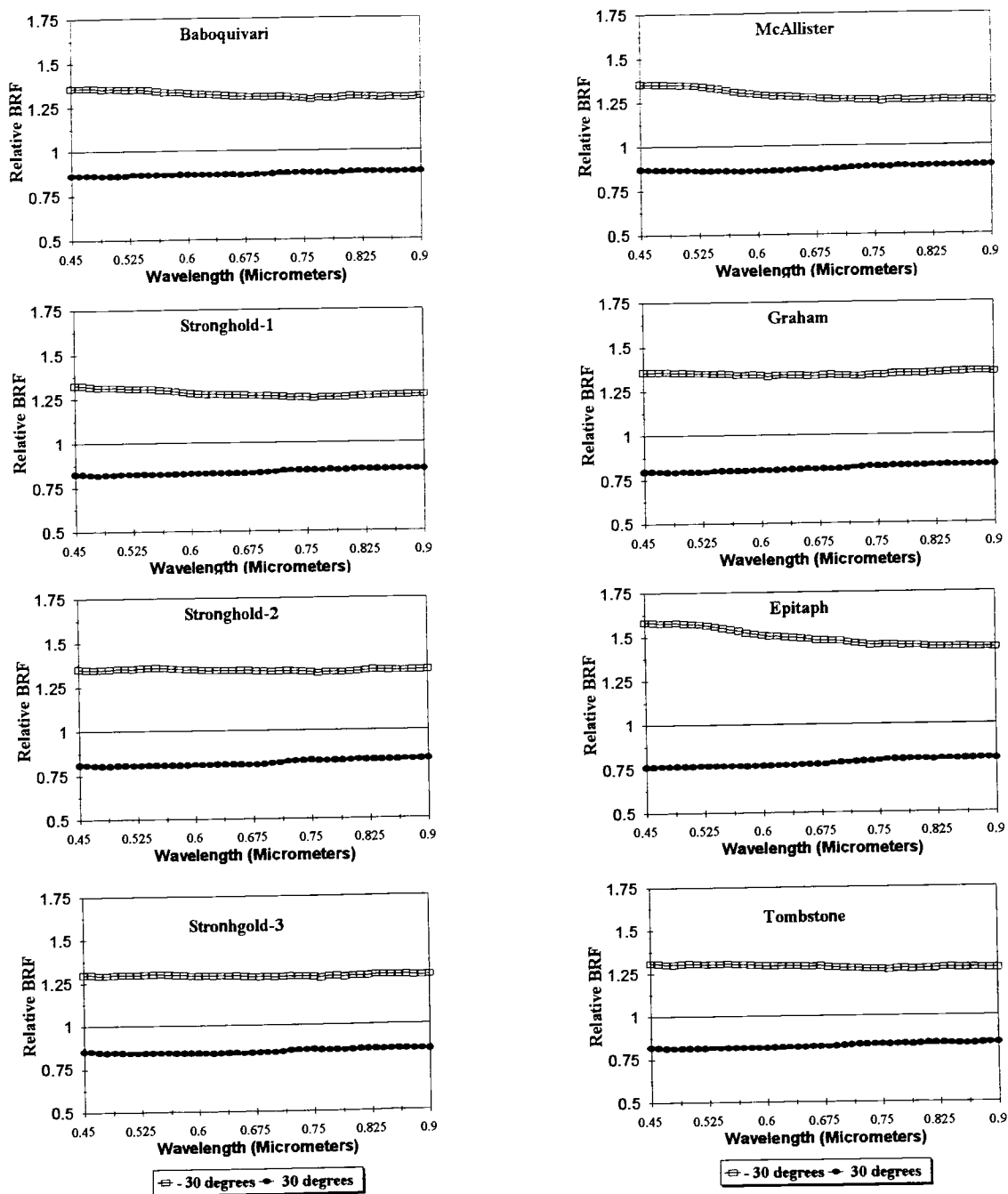


Figure 2-3. Spectral variation of relative BRDF for -30 and 30 degree viewing angles under dry conditions

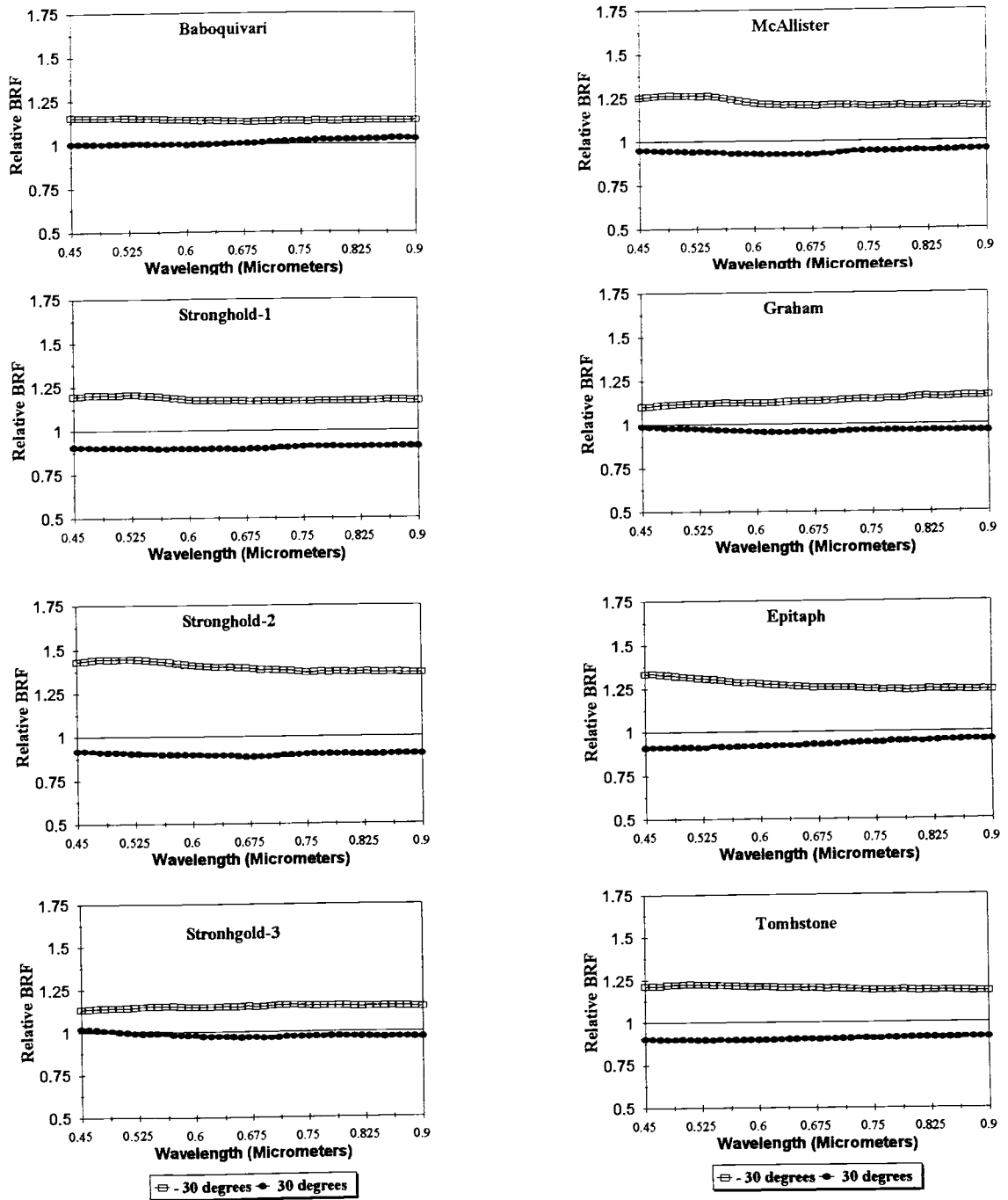


Figure 2-4. Spectral variation of relative BRDF for -30 and 30 degree viewing angles under wet conditions

Comparisons among the soils showed that almost all soils presented an increase between 30 and 36 percent relative to nadir in the reflectance factor throughout the measured spectrum in the backscatter direction for -30 degrees view angle.

Without exception the relative BRF for forward scattering direction decrease between 13 and 24 percent throughout the spectrum as compared to the nadir viewing response. Epitaph soils series showed the greatest decreased in the relative BRF (around 24 percent throughout the measured spectrum), while McAllister showed the least decrease in relative BRF (about 13 percent).

The highest value for relative BRF throughout the spectrum was found for Epitaph soil. For this soil, reflectance values for -30 degree view angles were about 60 percent in the visible and about fifty percent in NIR more than that found for the nadir view angle.

Wet condition. Under wet condition (Figure 2-4), the decrease in the relative BRF with the wavelength was noticed not only for McAllister and Epitaph but also for Stronghold-2 and, in less extension, for Stronghold-1 soils. When compared to dry condition, the relative BRF under wet condition were less for all soils but Stronghold-2. For Stronghold-2 soil sample, the relative BRF was about the same under wet and dry conditions. For Stronghold-2 soil, the relative BRF for -30 degrees were about 1.45 to 1.40 in the visible portion of the spectrum and about 1.37 in the NIR. The increase in relative BRF was much less for Graham, Stronghold-3, and Baboquivari soil samples. For these soils the relative BRF was about 10 to 15 percent greater than the values found for nadir view angle.

In the forward scattering direction (30 degrees view angle) there was much less decrease in relative BRF when the soils were wetted. In some cases this value approached the value found for the nadir view angle, or was higher (e.g. Baboquivari soil series) than that found for the nadir view angle. For the Baboquivari soil series, the relative BRF increased from the visible to the NIR region. In the visible Baboquivari soil series presented the same reflectance factor as that for nadir while in the NIR the reflectance factor was higher for 30 degrees than for nadir. Thus the value of the relative BRF was slightly above one.

Spectral variations on BRF as a function of -30 and 30 degree view angles as compared to nadir view angle for all eight soils are presented in Figure 2-5 for dry and in Figure 2-6 for wet conditions, respectively. Under dry and wet conditions, BRF values increased substantially for all soils when the sensor was positioned at -30 degree view angle. The increase was greater for Stronghold-2 soil sample and less for McAllister soil unit. BRF values decreased throughout the spectrum for 30 degrees view angle. Under dry conditions, however, the decrease in reflectance response due to the positive view angle was much less, relatively speaking, than the increase in reflectance response due to negative view angle (Figure 2-5).

Under wet conditions (Figure 2-6) the difference between nadir reflectance and the reflectance values presented when the sensor was pointing at -30 or 30 degree view angles is much less than that found for dry conditions. The only soil sample that maintained high values for reflectance in -30 degree view angle under wet conditions was Stronghold-2 . Baboquivari and Graham soils presented reflectance values for -30 degrees under wet conditions close to that for the nadir view angle. McAllister, Stronghold-1, Epitaph,

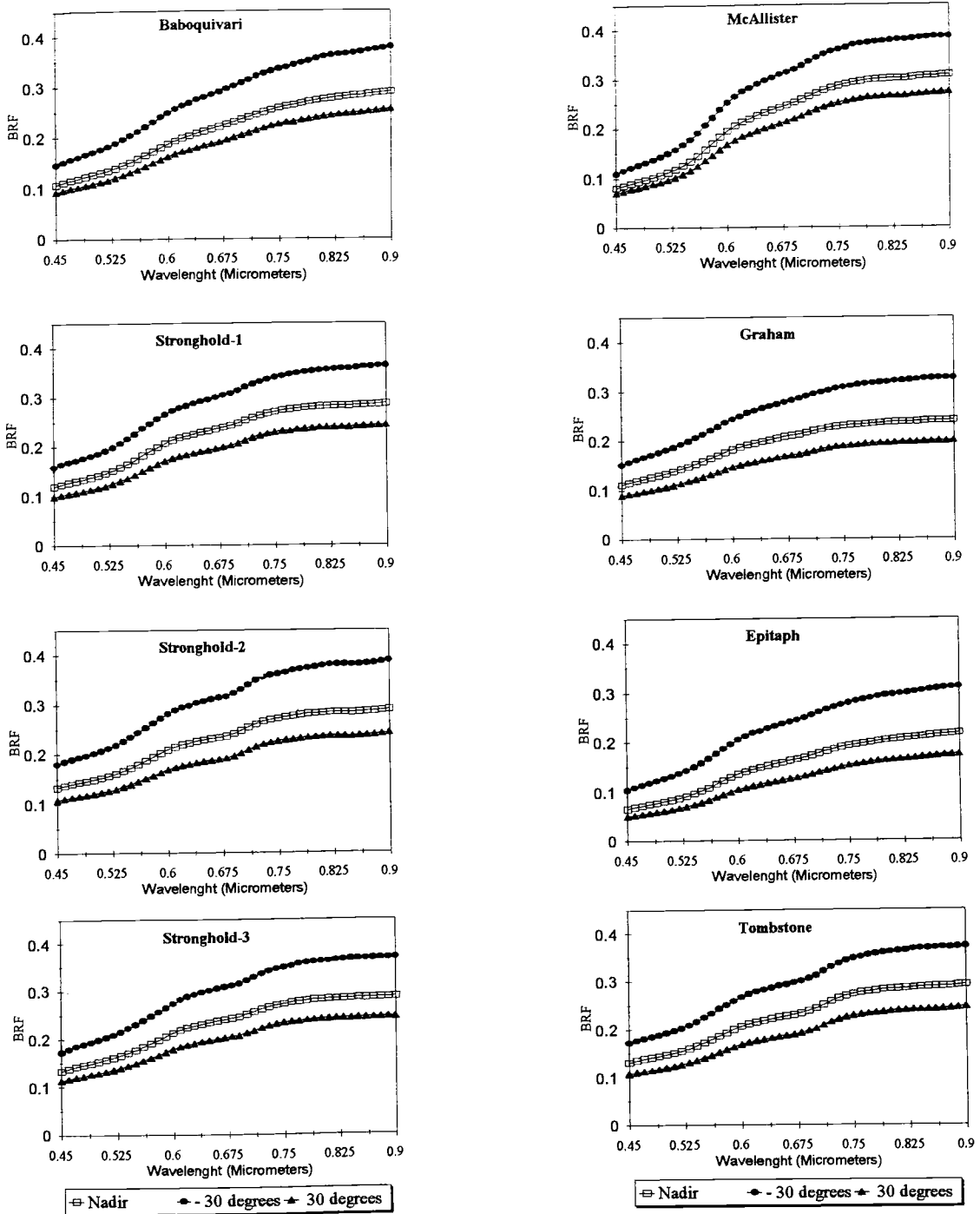


Figure 2-5. Effect of viewing angle on soil spectral response under dry condition

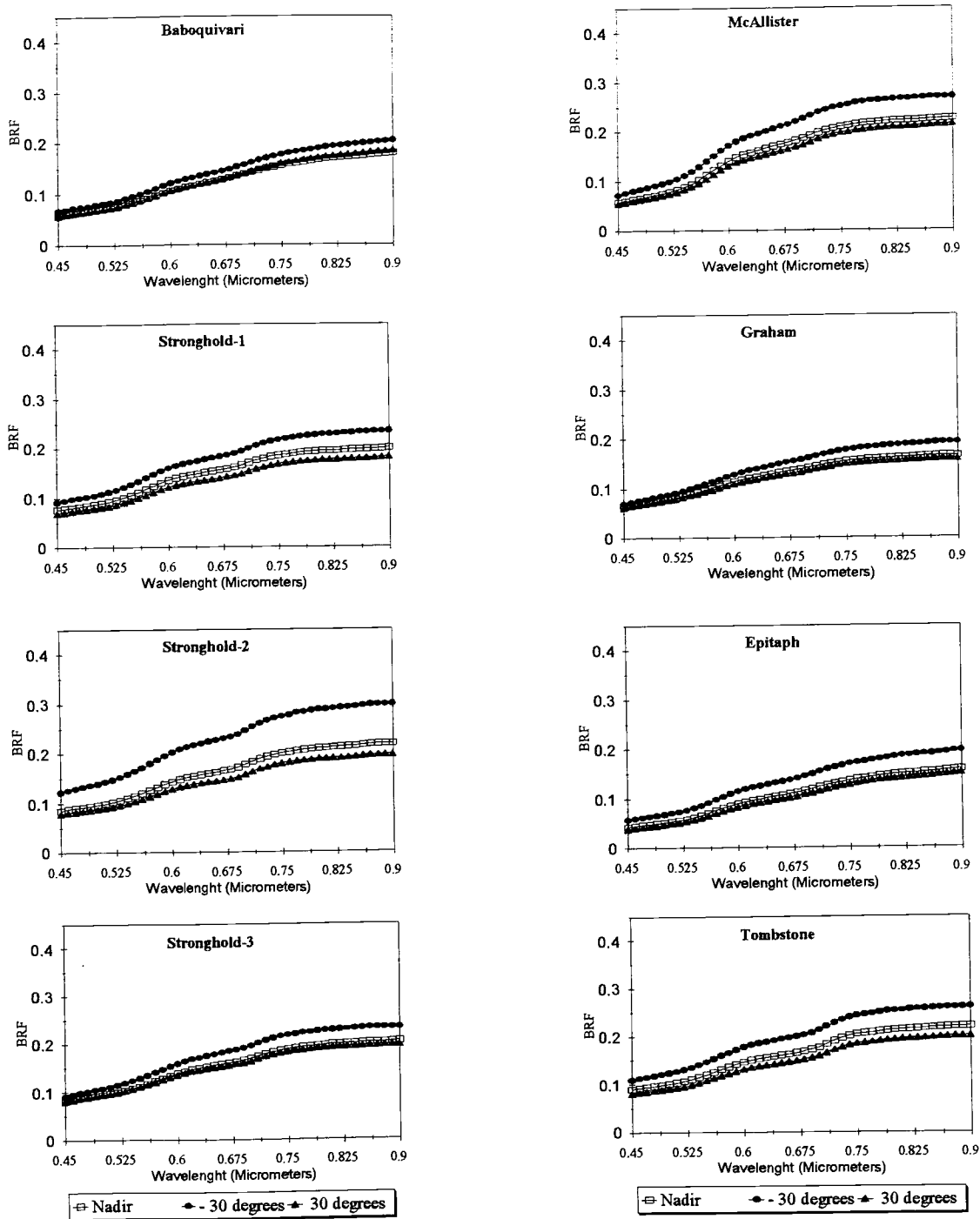


Figure 2-6. Effect of viewing angle on soil spectral response under wet condition

Stronghold-3 and Tombstone presented an intermediate reflectance value for -30 degree under wet conditions when compared to Stronghold-2 and Baboquivari or Graham (Figure 2-6). The spectra from most of the eight soil samples were very similar under either dry or wet conditions.

The effect of wetting for -30 degree, nadir, and 30 degree viewing angles is better visualized by ratioing the BRF response for these three view angles under dry and wet conditions (Figure 2-7). The ratio BRF dry/BRF wet varied with the wavelength for all soil surfaces and for both view angles considered. The ratio decreased continually from the blue part of the spectrum to the NIR. The only exception was Epitaph soil which presented a little peak at 0.52 μm .

For the backscatter direction (-30 degree view angle) the ratio BRF dry/BRF wet was much higher for Baboquivari, Graham, Epitaph and Stronghold-3 soil. For Baboquivari the ratio was above 2 for the visible portion of the spectrum, while in the NIR, this ratio was between 1.8 and 2. Graham soil series presented a very high ratio but this ratio decreased rapidly from the visible to the NIR. For a wavelength of 0.45 μm , Graham soil series presented a ratio BRF dry/BRF wet of about 2.2, while for 0.90 μm this ratio was reduced to 1.7. Stronghold-3 and Graham soils presented ratios that varied respectively from 1.9 and 1.8 for 0.45 μm to about 1.6 for both soils in 0.90 μm . McAllister, Stronghold-2 and Tombstone series presented about the same values for the ratio BRF dry/BRF wet. These values were around 1.5 for 0.45 μm and decreased to about 1.4 for McAllister and Tombstone and to 1.3 for Stronghold-2 in 0.90 μm . Stronghold-1 soil presented a ratio BRF dry/BRF wet that was intermediate between that found for the remaining soils.

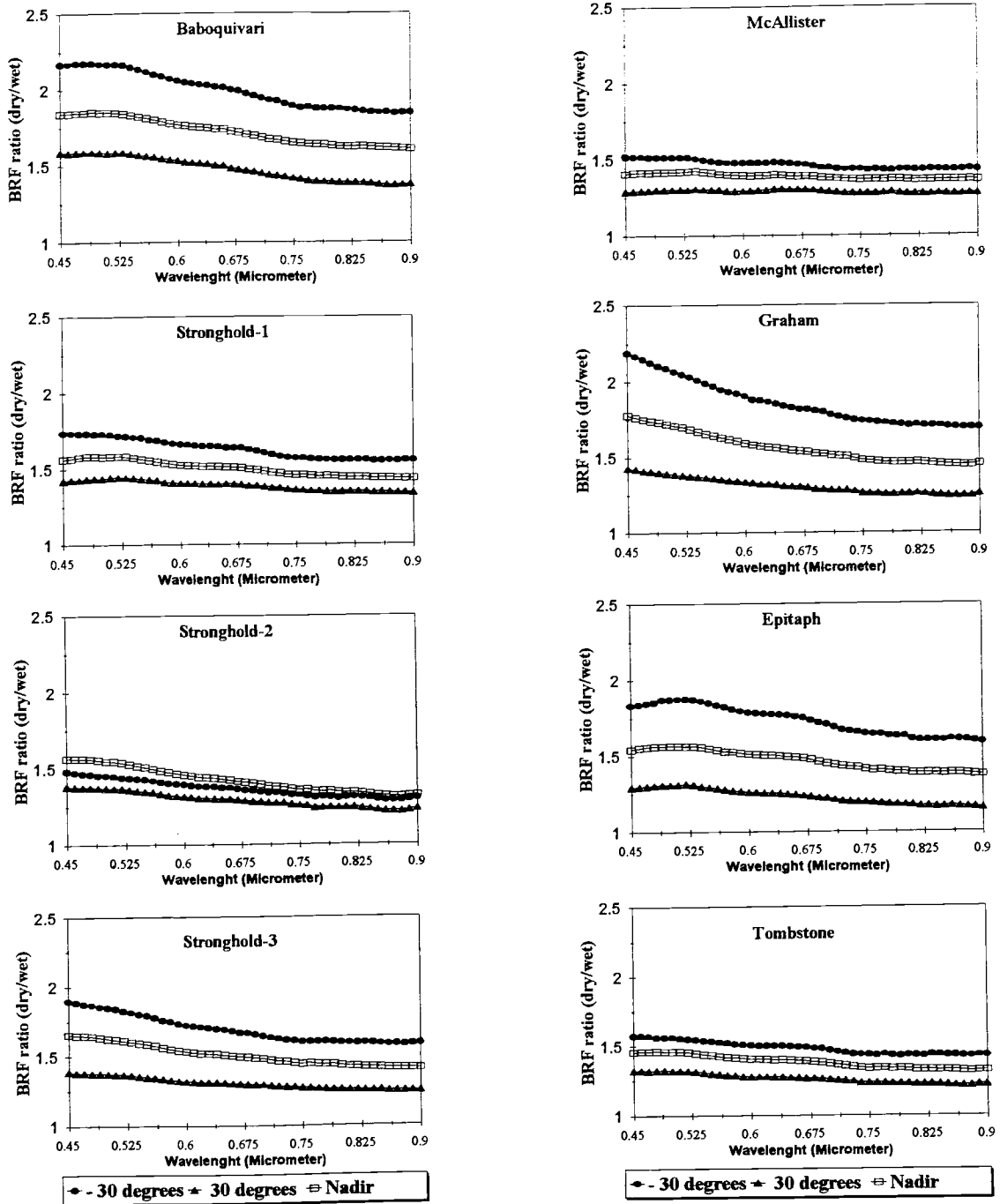


Figure 2-7. Ratios BRF dry/BRF wet for Nadir, -30 and 30 degree viewing angles

In the forwardscatter direction (30 degrees view angle), the ratio BRF dry/BRF wet was much less than that found in the backscatter direction, except for Stronghold-2 soil. The effect of wetting the soils on the spectral curves was much more pronounced when the sensor viewed the soils in the backscatter direction than in the forwardscatter direction. Baboquivari soil with 1.6 for 0.45 μm and 1.4 for 0.90 μm presented the highest values for the ratio of BRF under dry and wet conditions (1.6 for 0.45 μm and 1.4 for 0.90 μm). McAllister, Epitaph and Tombstone soils with an average of 1.3 for 0.45 μm and 1.2 for 0.90 μm presented the lowest value for the ratio in the forwardscatter direction. The behavior of the ratio BRF dry/Brf wet for the nadir viewing angle was, for all soils and in all spctral bands, intermediate between that found for -30 and 30 degree viewing angles.

RELAB Spectra

Figure 2-8 shows the spectral curves for each of the soil samples taken by the RELAB for three different viewing angles; nadir, -35 degrees (antillumination direction) and 35 degrees (forward scatter direction). All curves presented a monotonic increase from the blue region of the spectrum toward the midi-infrared region. In relation to the magnitude of response, Baboquivari, Tombstone and all of the Stronghold samples presented higher BRF throughout the spectrum than any other soil in all viewing angles, while Epitaph, and Graham presented low reflectance factors for all the measured spectrum and also for all viewing angles.

Absorption features were present in all soils, but in different levels of intensity. The water absorption bands were clearly distinguished in all curves, independent of the viewing angle, at about 1.40 μm and 1.90 μm with the last one being more pronounced. Some of the spectral

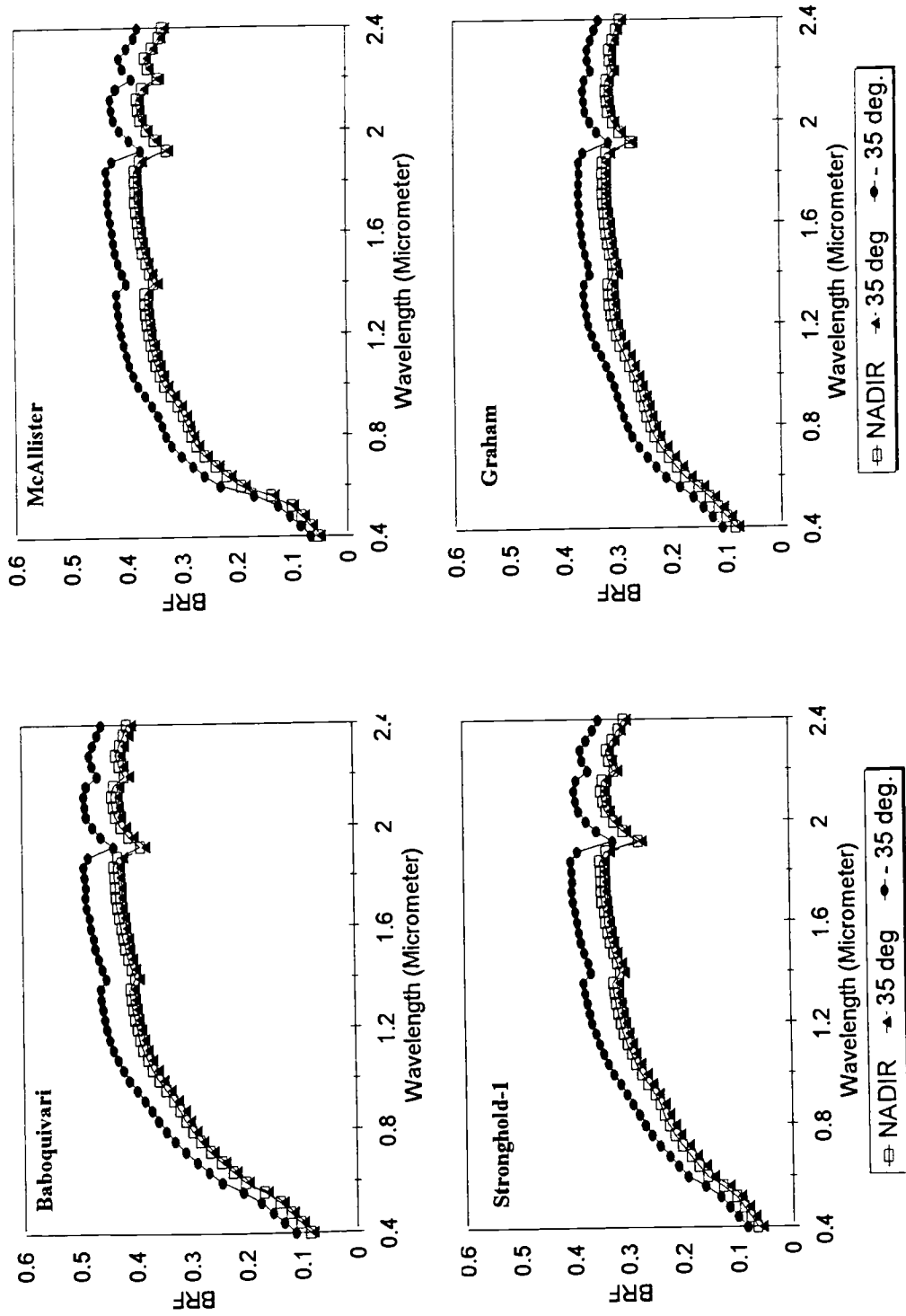


Figure 2-8. RELAB spectral curves

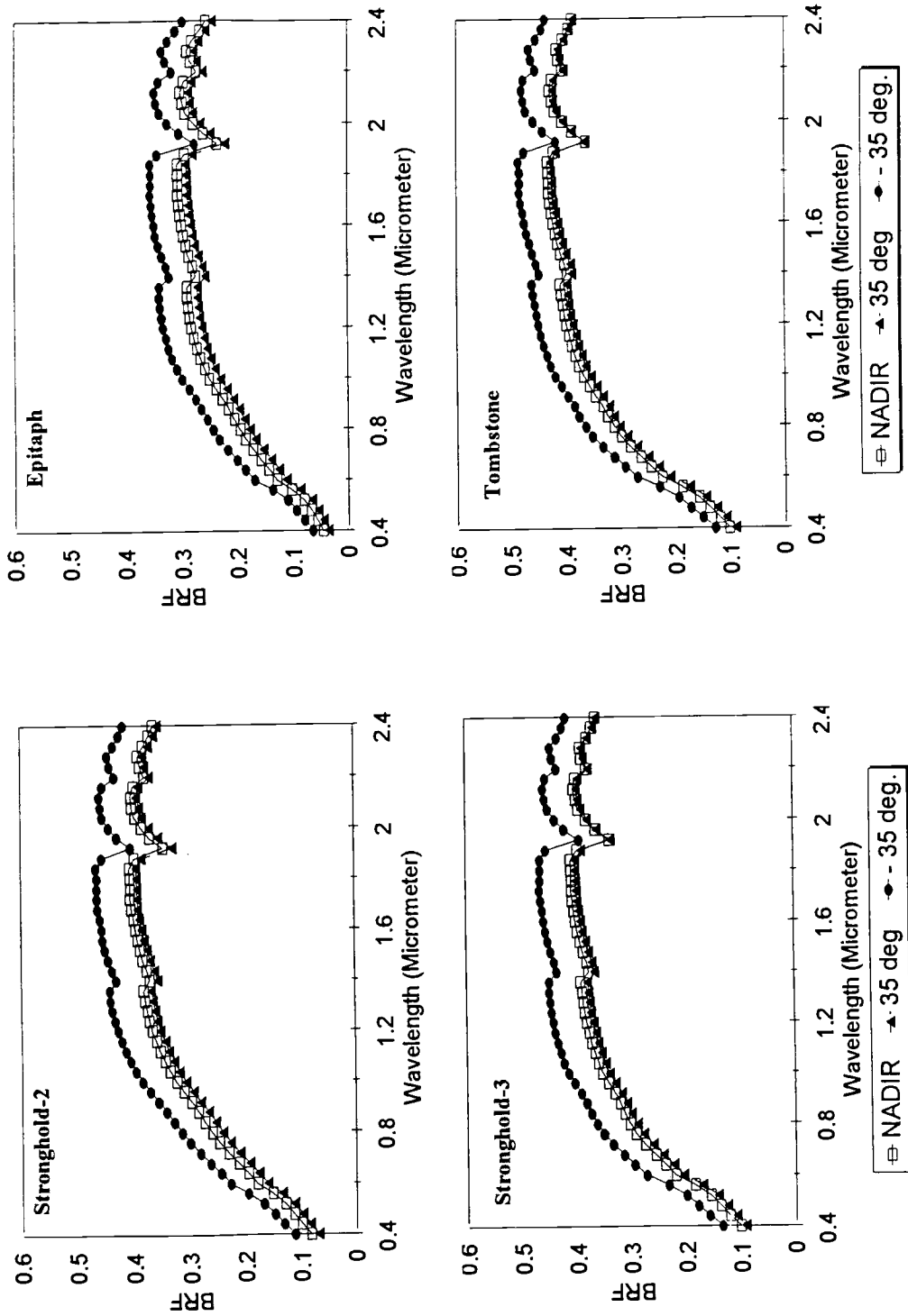


Figure 2-8. RELAB spectral curves (cont.)

spectral curves such as McAllister and Stronghold-3 resembled iron affected soils while others, such as Baboquivari, Stronghold-1, Stronghold-2, and Tombstone resembled the minimally altered spectral curves given by Stoner and Baumgardner (1981) and Baumgardner et al.(1985). The iron absorption band at about 0.90 μm was shown in a greater intensity by McAllister followed by Stronghold-3 soils. The decrease in reflectance toward the blue (one of the characteristics of the iron affected soils) was more pronounced for the McAllister soil than any other soil. Another feature, present in varying degrees of intensity at about 2.20 μm , is probably caused by the presence of kaolinite in the clay fraction of the soils. This feature at 2.20 μm was more pronounced in McAllister, Stronghold (1,2 and 3) and Epitaph, while it was almost absent for Graham soil. Indeed, as a result of its position in the landscape (which implies a less developed soil compared to the others) Graham soil was expected to have less kaolinite than other soils.

Figure 2-9 presents the relative BRF for RELAB's data resampled to match the six Thematic Mapper bands in the visible and reflective infrared region. The anisotropic behavior of all soils decreased from the blue region (TM1 or 0.45 to 0.52 μm) toward the mid-infrared region with TM bands 7 (2.08 to 2.35 μm) and 5 (1.55 to 1.75 μm) being the least affected by the non-lambertian properties of the soils. For TM band 1, the relative BRF in the antillumination direction (-35 degree) varied from 1.2 to 1.4 times the value obtained for nadir viewing angle while in the forward scatter direction (35 degree) BRF were decreased by a factor that varied from 0.94 to 0.81 in relation to nadir BRF in the same band. On the other hand, for TM band 7 these same quantities varied from 1.11 to 1.15 for -35° and from 0.95 to 0.99 for 35° viewing angles, respectively.

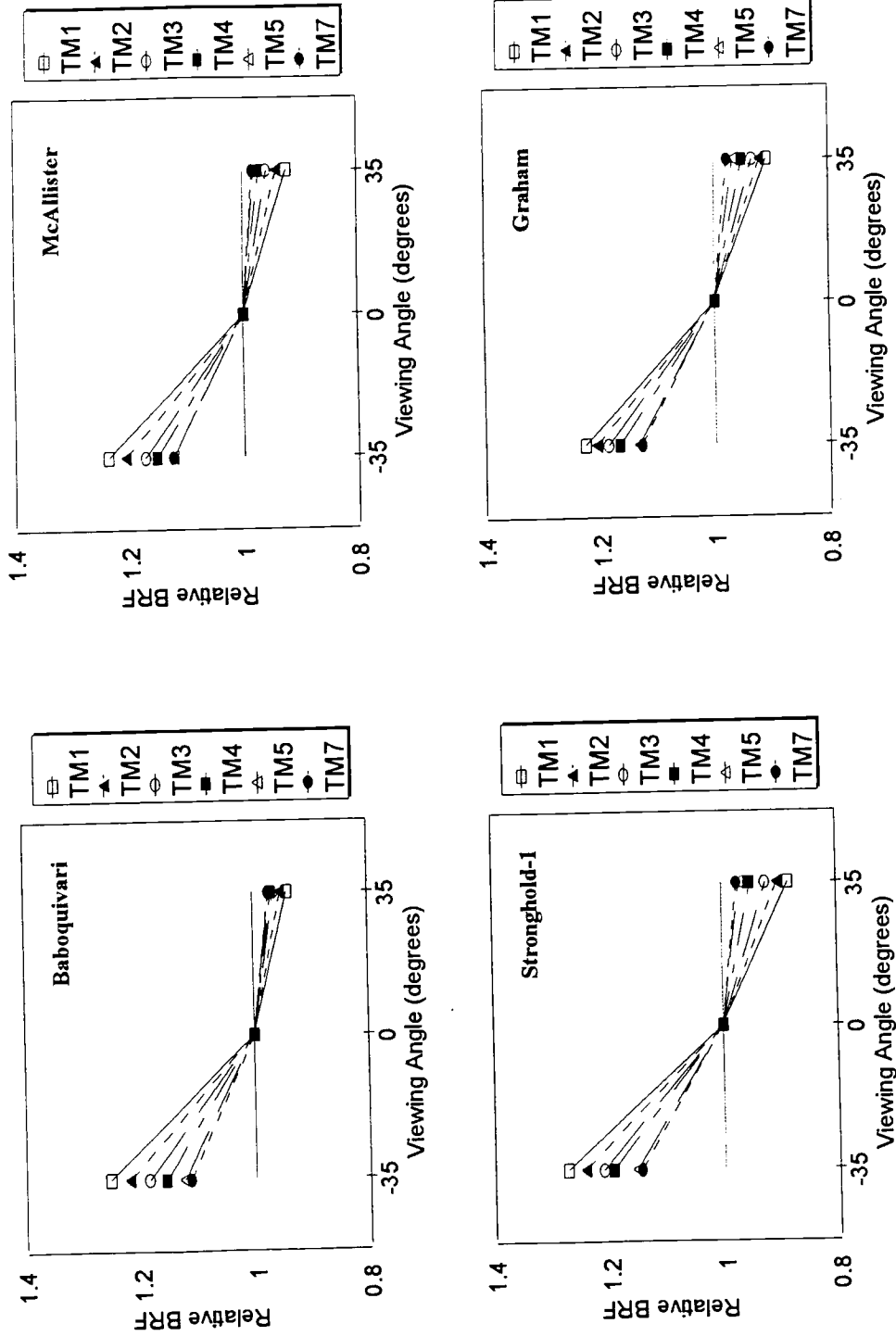


Figure 2-9. Relative BRF for RELAB data

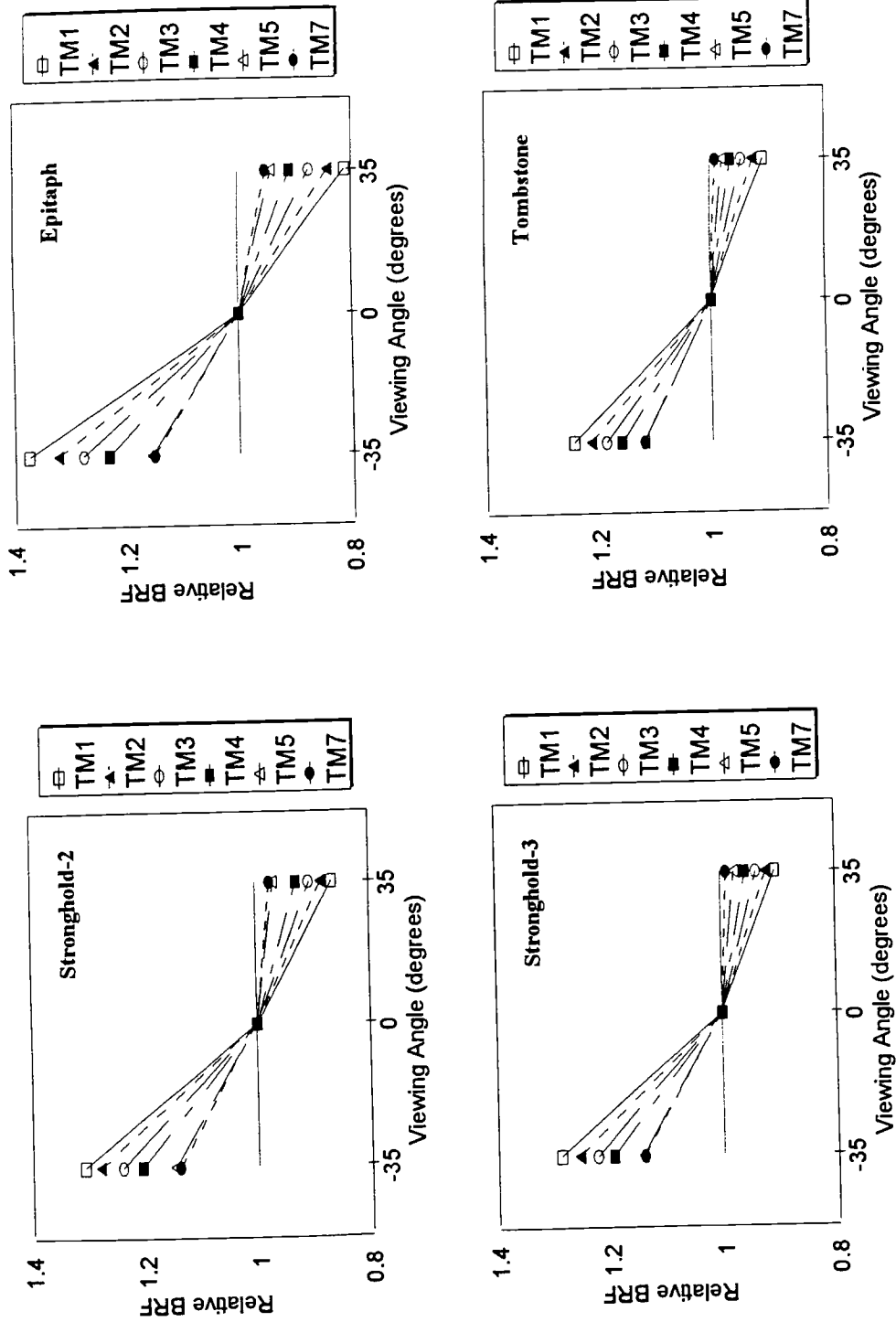


Figure 2-9. Relative BRP for RELAB data (cont.)

The TM band 5 presented values for relative BRF similar to that found for TM band 7 (Figure 2-9). Among the soils Epitaph exhibited the highest level of anisotropic behavior. For this Vertisol the ratio between BRF in the antilumination direction (-35 degree) and nadir were 1.38, 1.32, 1.28, 1.23, 1.16, and 1.15 for TM band 1 through TM band 7, respectively. Thus, the differences between BRF taken at nadir and at -35 degree increased by a factor of two when comparing the TM band 7 with TM band 1. In the opposite direction (35 degree viewing angle) Epitaph soil showed the same ratio, values of 0.81, 0.84, 0.87, 0.91, 0.94, and 0.95 for TM band 1 through TM band 7, respectively. Therefore, the decrease in BRF values varied from about 20 % for the blue band (TM1) to only 5 % in TM bands 5 and 7. Graham, McAllister and Tombstone presented less anisotropic behavior with a relative BRF that varied from about 1.25 for TM band 1 to about 1.13 for TM band 7 in the antilumination direction and from about 0.91 for TM band 1 to about 0.98 for TM band 7 in the forward scatter direction. The remaining soils presented an intermediate anisotropic behavior between these two extremes (Figure 2-9).

Effect of Roughness on the BRF Response of Epitaph Soil

As there were not too many differences in the roughness of the eight soil (except for Baboquivari and Epitaph - see Table 2-2) the influence of surface roughness on the spectral response for Epitaph soil series was evaluated. The Epitaph soil series was chosen because in this soil it is much easier to find naturally occurring "smooth" and "rough" surfaces.

The roughness index for each of the three conditions are present in Table 2-4. No significant differences were found for the roughness index for each of the surface conditions

Table 2-4. Roughness index

Solar Zenith Angle (degrees)	Roughness (Relative Arc Length)		
	Smooth	Intermediate	Rough
30	1.028a	1.143b	1.304c
40	1.032a	1.152b	1.293c
50	1.036a	1.171b	1.341c

Averages followed by the same letter do not differ by t - test ($P < 1\%$)

for measurements made in different solar zenith angles (Table 2-4).

Table 2-5 shows the percent of cover for each rough condition and for the three solar zenith angles. The proportion of each cover type varied according to the solar zenith angle because the location of the area was tilted along an imaginary axis so that the measurement of the percent of cover was taken in lines parallel to the line that represent the intersection of the principal plane with the soil surface.

Bare soil surface and fine gravel predominated on the smooth surface, while rock fragments greater than fine gravel dominated the surface cover of the intermediate and rough surfaces. Most of the differences between intermediate and rough surfaces were due to the differences in the proportion of the type of rock fragments rather than the total percent in rock fragments per se. Thus, for intermediate rough surface the rock fragments were dominated by almost equal proportions of medium gravel (5 - 20 mm), coarse gravel (20 - 75 mm) and cobbles (75 - 250 mm), while for the rough surface cobbles dominated the rock fragment fraction.

Figure 2-10 shows the results for relative BRF processed for TM1 (0.450 - 0.520 μm) for each roughness condition and for each sun zenith angle under dry and wet conditions. TM band 1 was selected because it presented more sensibility to surface roughness as discussed. For both conditions, dry and wet, the anisotropic behavior of the soil increase from 30 to 50 degree solar zenith angles. A "hot spot" was visible for viewing angles in the backscatter direction that coincided to the solar zenith angle. Thus, due to the range of viewing angle given by the BRF apparatus (- 45 to 45 degrees) the hot spot for 50 degree solar zenith angle (Figure 2-10) could not be seen.

Table 2-5. Characterization of the percent of cover in the roughness experiment

Cover Type	Percent of cover											
	Smooth			Intermediate			Rough					
	30°	40°	50°	30°	40°	50°	30°	40°	50°			
Bare Soil	76.5	64.5	60.0	35	37.5	25.5	33.5	34.5	31.0			
Rock Fragments	13.0	27.5	34.0	56.0	49.5	59.0	53.0	55.0	50.5			
- Fine Gravel (2-5 mm)	12.5	27.5	32.5	7.5	8.5	11.5	0.5	-	0.5			
- Medium Gravel (5-20 mm)	-	-	-	18.5	16.0	15.5	2.0	1.0	0.5			
- Coarse Gravel (20-75 mm)	0.5	-	-	16.5	13.5	15.0	4.0	6.0	9.0			
- Cobbles (75-250 mm)	-	-	1.5	13.5	11.5	17.0	26.0	45.5	38.0			
- Stones (250-600 mm)	-	-	-	-	-	-	19.5	2.5	2.5			
Litter	10.5	8	6	9	13.5	14.5	13.5	10.5	18.5			

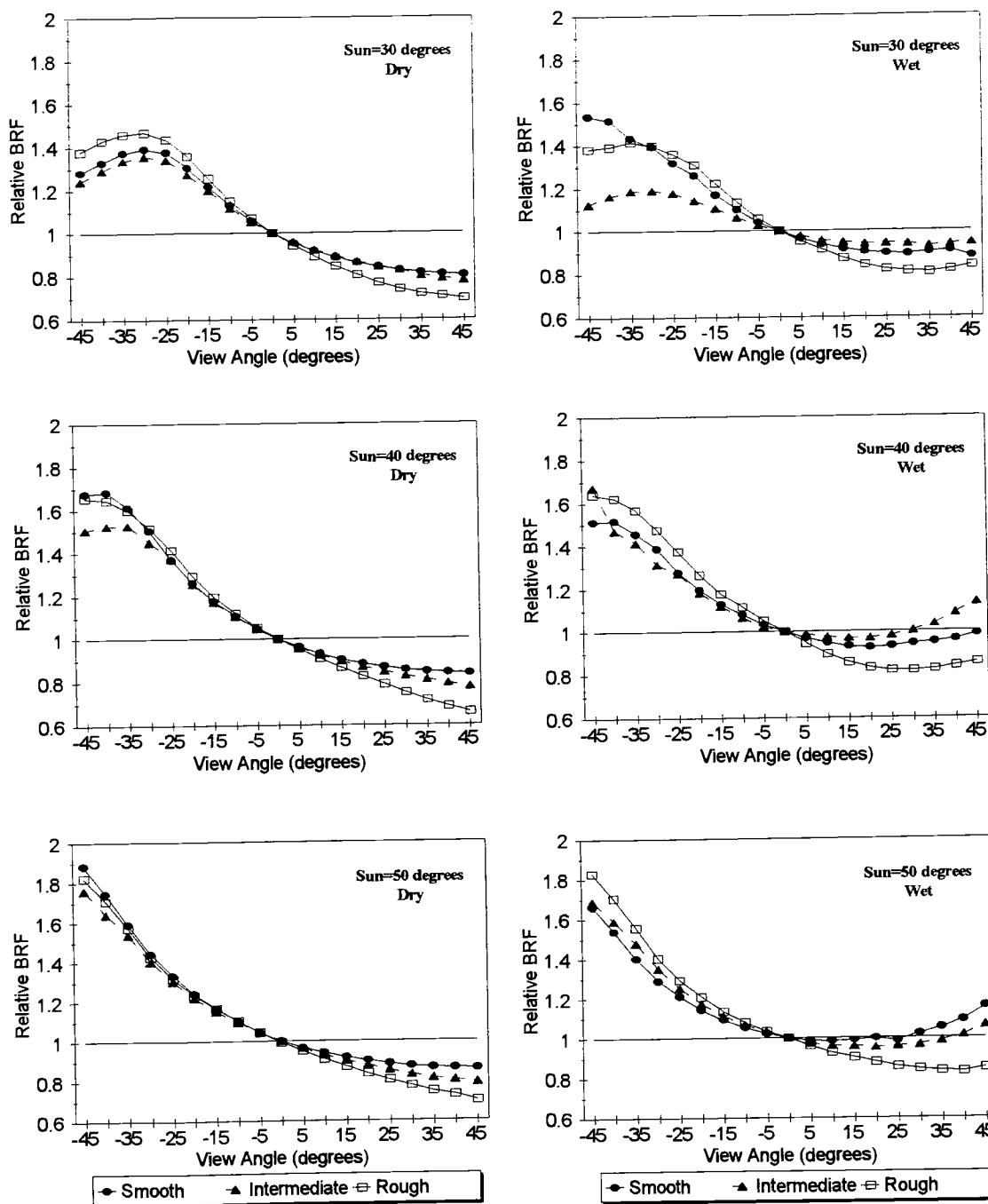


Figure 2-10. Effect of View and Sun zenith angles on Relative BRF under dry and wet conditions

Data processed for TM band 1(0.45 to 0.52 Micrometers)

In the backscatter direction the relative BRDF varied from 1.5 (for 30 degree solar zenith angle) to 1.9 (for 50 degree solar zenith angle) for the dry condition. Except for some specular behavior of the smooth and the intermediate rough surface in the forward scatter direction, little differences between spectral responses for the soil surfaces in dry and wet conditions can be seen in Figure 2-10 for the cases of solar zenith angles of 40 and 50 degrees. Some differences can be seen between the spectral response of different surface roughness when both conditions (dry and wet) for a solar zenith angle of 30 degree are considered. For that solar zenith angle, the spectral response of the intermediate and rough surface decreased when the soil was wetted.

The curves in Figure 2-10 show that even for the smooth surface there was enough roughness relative to the wavelength to cause them to be asymmetric about nadir with a hot spot in the antisolar direction for solar zenith angles of 30 and 40 degree. Although the microroughness meter had detected a range of about only 1.03 to 1.04 relative arc length for the roughness conditions, Table 2-5 shows that the fraction of small rock fragments was much more representative in the smooth surface than the value obtained by the microroughness meter. Indeed, the measurement of surface roughness had been reported as a complex task and many devices have been suggested for several authors (see the list of selected profile meters presented by Robichaud and Molnau, 1990). Huang and Bradford (1990) stated that surface elevations between grid point, normally 5 to 50 mm apart, were not measured by drop pin devices and as a result these type of devices are useful for measuring surface roughness due to tillage marks or large clods. In the case of our microroughness meter, for example, the fine gravel fraction (diameter between 2 and 5 mm) could not be

detected by the 10 mm spaced pins. Probably the fine gravel fraction, which increased from the measurement made for 30 degree to 50 degree solar zenith angle (Table 2-5), had an important role in the small differences when comparing the smooth surface with the intermediate and rough surfaces in any solar zenith angle and for both conditions, dry and wet when considering the spectral response in the antisolar direction.

Another probable reason for the small differences between the smooth surface and the intermediate and rough surfaces was associated with the fact that the basalt rocks presented in the field of view of the instrument were spectrally darker than the soil background. Figure 2-11 shows the average spectral curve for nine samples of the rocks present in the plots in the rough experiment. Considering that both the intermediate and the rough surfaces presented more than 50% of rock fragments the BRF values for these two rough conditions were expected to be highly influenced by the dark spectral response of these rock fragments mainly in the backscatter direction. The best results mentioned in the literature relating BRF to surface roughness normally used the tillage effect on a "smooth" soil surface (see for example, Irons and Smith 1990, and Jackson et al.,1990). The use of a leveled soil to mechanically generate various degrees of roughness did not present the same effects as the random rock background pointed out above.

The effect of the roughness can be readily seen, however, when we consider the spectral response in the forward scatter direction for any solar zenith angle and in dry and wet conditions (Figure 2-10). In the forward scatter direction the effect of shadows prevailed over any other factor and, as a result, the rough surface presented the lowest BRF values. In the forward scatter direction the effect of shadows increased as the viewing angle was increased.

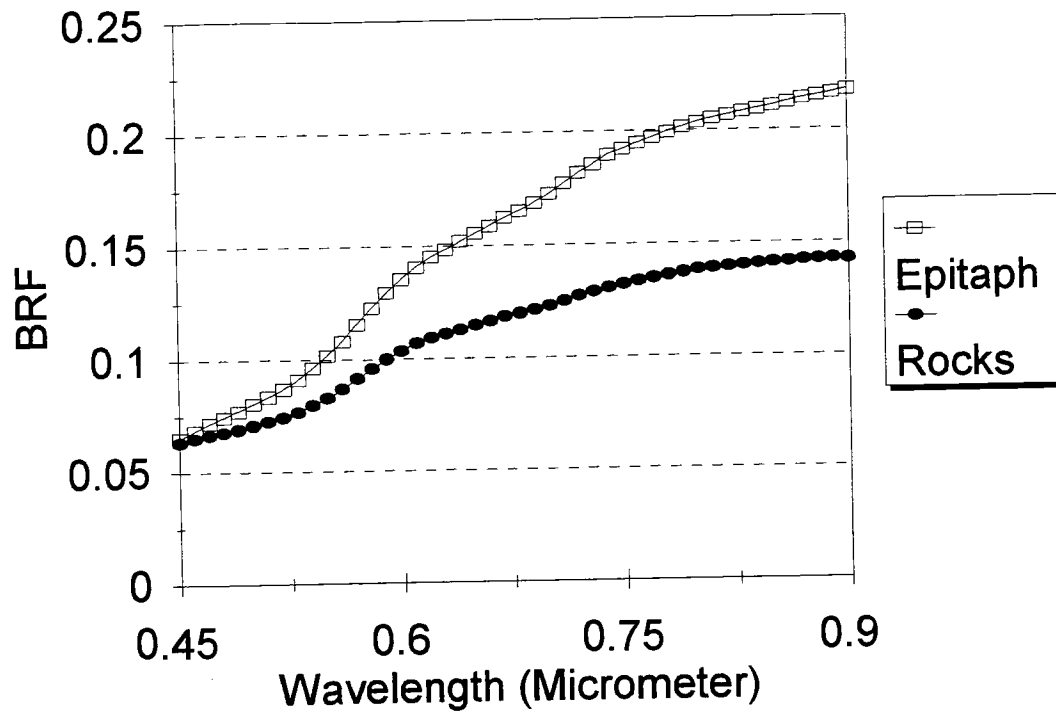


Figure 2-11. BRF for Epitaph soil as compare to the BRF of volcanic rock outcrops

The decrease in BRF for 45 degrees under dry condition, for example, was about 0.65 of that for nadir BRF for the rough surface and an average of 0.85 for the smooth surface when the three solar zenith angles were considered.

Though the same tendency as seen for dry condition can be seen for 30 degrees solar zenith angle, the effect of roughness in the forward scatter direction under wet condition is somehow difficult to analyze for the other two solar zenith angle due to retroreflectance for viewing angle greater than 15 degrees.

The wavelength dependency as a function of surface roughness under dry and wet conditions and for a solar zenith angle of 30 degrees is shown in Figure 2-12. In the backscatter direction, the relative BRF decreased from the blue toward the NIR region for all surface roughness and for dry and wet conditions except for the intermediate rough surface under wet condition. Under dry condition the difference between rough and smooth surfaces when seen in the backscatter direction was kept constant throughout the measured spectrum (0.45 to 0.90 μm). Under wet condition, however, no difference in the relative BRF was seen when compared to rough and smooth surfaces in the visible spectrum. The relative BRF for the rough surface was greater than the relative BRF for the smooth surface from 0.70 to 0.90 μm in the backscatter direction. The intermediate rough surface, however, presented the same relative BRF as the smooth one throughout the spectrum in the backscatter direction and under dry condition. Under wet condition and for the same viewing direction, the relative BRF was much smaller in the intermediate rough surface than in the smooth surface. The greater anisotropic behavior throughout the measured spectrum of the rough surface as compared to the smooth and intermediate rough surfaces can also be seen for the forward

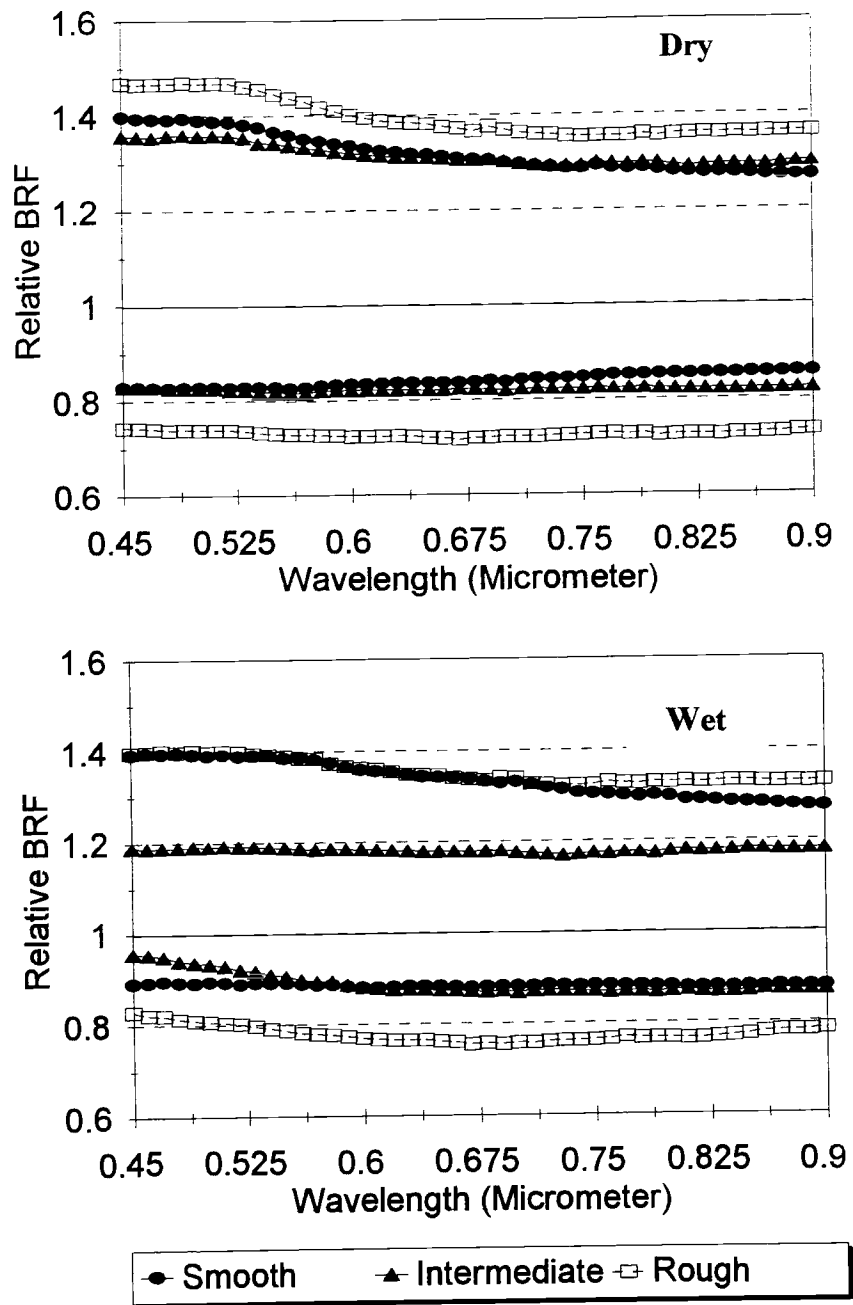


Figure 2-12. Wavelength dependency of relative BRF for -30 degree (lines above the unit line) and for 30 degree (lines below the unit line) view zenith angles. Sun zenith angle of 30 degrees

scatter direction in Figure 2.12. The relative BRF was almost constant throughout the spectrum with an average value of 0.7 for the rough surface and 0.8 for the smooth and intermediate surfaces in the forward scatter direction and under dry conditions. Under wet conditions these values increased for an average of 0.8 for the rough surface and 0.9 for the smooth and intermediate surfaces.

The results presented and discussed above are in agreement with the statements of Irons and Smith (1990) that a simple quantification of the degree of roughness is insufficient to predict the characteristics of a rough surface BRF. Irons and Smith (1990) also emphasized that the shape and orientation of the geometric objects which form the surface, rock fragments in our case, must also be taken into account.

Conclusions

The results presented in this Chapter show that the non-lambertian properties of soil surfaces need to be taken into account when we are dealing with off-nadir signal that comes from an airborne or spaceborne sensor.

Among the soils, Epiaph presented the highest anisotropic behavior whether the data came from field or from RELAB's spectral curves. Except for Epiaph, the other soils presented similar anisotropic behavior.

Besides the influence of soil types, the extent of non-lambertian behavior of soil surfaces depended on the moisture (wet or dry conditions), surface roughness, solar zenith angle, and the wavelength. Thus, for any of the soils in this study BRF signatures presented a high degree of anisotropy under dry conditions, under the roughest conditions (within the

characteristic range of roughness of each soil), under higher solar zenith angle and for measurements taken at shorter wavelength.

In relation to the criteria defined by Stoner and Baumgardner (1981) for soil spectral curve shapes two basic types were distinguished in the AVIRIS scene of Walnut Gulch Experimental Watershed: the iron affected curve form represented by McAllister and Stronghold-3 soils and minimally altered curve form represented by Baboquivari, Stronghold-1, Stronghold-2, and Tombstone.

Besides the spectral response due to the intrinsic characteristics of soil surfaces, soil spectral signatures varied with view angle, moisture conditions and surface roughness. In relation to view angle, although curve shape was preserved, the magnitude of soil surface BRFs for all soils presented in the AVIRIS scene were higher for off-nadir viewing angles in the backscatter direction and lower for off-nadir viewing angles in the forward scatter direction compared to nadir BRFs. The effect of wetting on reducing BRF was dependent on the viewing angle and wavelength. For all the eight soils the reduction in BRF after wetting was greater for nadir and for viewing angles in the backscattering direction than for viewing angles in the forward scatter direction and also in shorter wavelength (blue) than in longer wavelength (NIR).

In relation to the influence of surface roughness on the spectral response of soil surfaces, it appeared that the spectral contrast between rock fragments and soil background plays an important role on BRF differences between "smooth" and "rough" surfaces. In this particular case, for Epitaph soil the dark fragments of basalt rocks tended to reduce the anisotropic behavior of the roughest surfaces in the backscattering direction. In this situation

a better differentiation between "smooth" and "rough" surfaces on the base of their BRFs was obtained in the forward scatter direction.

CHAPTER 3

IMAGE SPECTROSCOPY AS COMPARED TO FIELD AND LAB SPECTROSCOPY

Introduction

Remote sensing spectroscopy can be divided into lab spectroscopy, field spectroscopy and image spectroscopy. Some of the basic differences in these three types of remote sensing spectroscopy are related to the way in which the information is extracted and typically involve scale problems. At laboratory scale the sensor is close enough to have a small field of view under controllable, and normally strong, source of illumination. Normally, samples sent to laboratory are as homogeneous as possible and, in some cases, they can be considered "pure". As a result of the increase in the area viewing by the sensor the spectra measured under field conditions frequently are from a much less homogeneous sample. In the field a target is illuminated by a variable and uncontrollable source of radiation. Although the time that a sensor sees a target (dwell time) can be adjusted under lab and field spectroscopy to assure that enough photons can reach the sensor under the sensor and target characteristics (and, consequently increasing the output signal), the same is not true when dealing with imaging spectroscopy. An airborne or spaceborne imaging spectrometer has less measurement time and a variable, uncontrollable, and relatively weak radiation source which illuminates a typically heterogeneous sample located far from a detector (Curran, 1994). As compared to

lab or field spectrometry, the radiances that reach an imaging spectrometer carry much of the atmospheric effects which affects the retrieval of spectral ground information.

Laboratory spectroscopy has been applied to remote sensing most of the time in the optical region (from 0.25 to 3.0 μm). The primary objective of the lab spectroscopy is for spectral matching studies, where libraries of "pure" spectra are used to identify spectra of other unknown samples obtained from laboratory, field or image data. Laboratory spectra can be used, also, to convolve digital number or radiance images to reflectance images (Milton, et al., 1995; Adams et al., 1993; Farrand et al., 1994). Laboratory spectroscopy also has importance in evaluating the concentration of these "pure" materials in a sample. Thus, near infrared laboratory spectra have been used for many years to determine nitrogen and lignin concentration in plant materials (Norris et al. 1976; Wessman et al., 1988b). Field spectroscopy is a technique used to measure the spectral characteristics of objects in the natural environment and find application in a number of areas of remote sensing (Milton et al., 1995). Measurements in the field are used to serve as (1) "ground truth" for airborne or spaceborne data calibration, validation, and interpretation and/or (2) as a way to characterize interactions between target and the impinging electromagnetic radiation (Deering, 1989).

Image spectroscopy or spectrometry consists of the simultaneous acquisition of images in many narrow (e.g 10 nm) contiguous spectral bands in the visible and solar-reflected infrared (Goetz et al., 1985). One of the main reasons for developing hyperspectral systems is to detect narrow absorption bands in the spectra of minerals and other materials, because such bands often are diagnostic of chemical composition and structure and are useful for identification (Adams et al., 1993). Thus, early work with data from the first airborne

imaging spectrometers confirmed that direct mineral identification could be achieved remotely (Goetz et al., 1985) and indicated that the tool was of value for scientists in other areas, such as botanic (Peterson et al., 1988; Wessman et al., 1988a). Kruse and Calvin (1988) used image data from AVIRIS to characterize the presence of sericite (fine grained muscovite) and dolomite by matching the image spectra of these minerals with the ones obtained in the laboratory. The same authors were able to directly identify the minerals kaolinite, alunite, and buddingtonite at Cuprite, Nevada, using a feature extraction algorithm implemented for a 64 channel data acquired by the Geophysical and Environmental Research Imaging Spectrometer (GERIS) (Kruse and Calvin, 1988). In the field of ecology several authors have shown that there are strong relationships between the concentration of key elements/biochemical (e.g., nitrogen, lignin, etc) and the amount of reflected radiation across spectral absorption in leaves under lab conditions (Card et al., 1988). Researchers have been trying to derive similar relationships for vegetation canopies using imaging spectroscopy but there is still a need for research for a better understanding of this information (Curran and Kupiec, 1995). Wessman (1995) states that advances in imaging spectrometry will permit the detection of spectral shape characteristics indicative of a vegetation biochemical state and will enable the reduction of atmosphere and background effects.

The success of spectral matching studies, however, depends to a large extent on how well the encoded radiance data is calibrated to reflectance as well as on the various factors that control the presence and strength of characteristic absorption bands in spectra (Adams et al., 1993). On the other hand, the problem of scale leads to the fact that many of the strong absorption bands that are seen in the laboratory spectra are weak or undetectable when the

same materials occur on natural surfaces. Absorption bands in any one material may vary significantly in strength depending on factors such as particle size and the presence of other materials that are strongly absorbing. Within a pixel-size area a material, which in pure form in the laboratory would show characteristic absorption bands, may have weak or indistinct bands that are of the same magnitude as the effects of atmospheric and instrumental variations (Adams et al., 1993). Special techniques, such as the first and higher order derivative spectra, are often needed to enhance these subtle features which were degraded either due to scale problems or due to low concentration of the target material in the sample.

The spectroscopy concepts either applied to lab and field or to images, leads also to the concept of hyperspectral that refer to the multidimensional character of the data set (Goetz et al., 1985). The use of multidimensional data either in terms of number of the different set of observations or in terms of the number of variables enables us to apply different kinds of multivariate techniques to extract the dimensionality of our data set. When dealing with observations, cluster analysis has proven to be one of the most valuable techniques to find groups of observations that presented high degrees of similarity within the group when considering a pool of variables. Cluster analysis is a generic term for a set of techniques which produce classifications from initially unclassified data (Everitt, 1980). Ball (1971) cited by Everitt (1980) listed the following seven possible uses of clustering techniques: (i) finding a true typology, (ii) model fitting, (iii) prediction based on groups, (iv) hypothesis testing, (v) data exploration, (vi) hypothesis generating, (vii) data reduction. Smith et al. (1990) used cluster analysis as a mean of testing whether spectral mixture analysis provides a consistent framework to evaluate temporal changes in a scene. Smith et al.(1990) showed that

uncorrelated multitemporal images should be revealed by cluster analysis.

In relation to hyperspectral data, the dimension in terms of bands can be found through other kind of multivariate techniques, such as factor analysis. Factor analysis attempts to simplify complex and diverse relationship that exist among a set of observed variables (such as bands in a hyperspectral data set) by uncovering common dimensions or factors that link together the seemingly unrelated variables, and, consequently, provides insight into the underlying structure of the data (Dillon and Goldstein, 1984). Unlike cluster analysis, however, factor analysis involves an artificial or abstract factor solution (Parks, 1966). One purpose of factor analysis, as applied to remote sensing, is to decompose measured spectra from experimental data or pixels into the spectra of their reflecting components. It is also of interest to identify the unique components present in a spectral mixture and assess their relative contributions toward measured responses (Huete, 1986). Huete (1986) successfully decomposed soil-plant spectral mixtures into dry soil, wet soil, and vegetation components and found their respective concentration. Using factor analysis Huete and Escadafal (1991) were able to identify four basis curves in a wide genetic range of fine resolution spectra from soil materials.

As shown in Chapter 2, the soils of the Walnut Gulch Experimental Watershed presented different anisotropic behavior which varied, among other factors, with the wet, and rough conditions. These results were confirmed either for soil spectra collected under field or under lab conditions. Although different, it is still unknown whether the extent of the differences for a given soil can affect the selection of a spectra as an endmember. Grouping the soils in spectral classes using cluster analysis can give a good idea if factors, such as

viewing angle and degree of wetness, can affect endmember selection in spectral mixture analysis. Another aspect of the selection of spectra to serve as the input in spectral mixture models is related with where given spectra come from. As reviewed above, scale problems affect the information that can be extracted from a given spectra and, as a result, this factor has to be taken into account in the selection of spectra for mixture modelling.

The objectives of this Chapter were: (i)-to compare the information content from spectra obtained under field conditions, sieved samples, lab (RELAB) and extracted from AVIRIS image (atmospherically corrected, and apparent reflectance); (ii)-to study the dimensionality of the data set in terms of soil spectral classes in relation to viewing angle, degree of wetness, and scale effects;(iii)-to study the dimensionality of the data set in terms of number of bands, their location, and the spectral bands that each one represents.

Some questions to be answered in this Chapter are: (a) How spectra obtained from different conditions compare to each other ? (b) How enhancement techniques, such as first derivative spectra can help in extracting information from soil spectra ? (c) How many spectral classes of soils are there for spectra obtained under different conditions ? (d) Is there any change in the way soil spectra are grouped when comparing soil spectra obtained under different conditions ? (e) How many bands are needed for soil information extraction ? (f) Where are they located and which interval of the electromagnetic spectrum do they represent (g) How are soil spectra grouped after hyperspectral data set are compressed.

Methods

Lab and Field Spectroscopy

Soil samples were collected from the first centimeter in depth from the same spot where BRF were measured in the field. Air dried samples for each of the eight sites were crushed to pass through a 2 mm sieve before BRF measurements. The BRF was measured with the Spectron SE590 spectroradiometer (0.45-0.90 μm in 0.01 μm or 10 nm sampling interval) for these soil samples under dry and wet conditions. The soil samples were put in black plates 2 cm deep and 22 cm in diameter. The measurements were made outdoor on cloudless days. In this case the outgoing radiance was collected with the sensor in the nadir view angle, while the solar zenith angle was about 30 degree. Sample wetting was done in the same manner as described in Chapter 2. Reflectance factors were obtained by ratioing the reflected response from a soil by that of the spectralon panel with reflectance values adjusted for the sun angle. From here the spectra obtained in this way is called the "sieved sample spectra" to differentiate it from the spectra obtained under field condition (field spectra) and the ones obtained under RELAB conditions (RELAB spectra). The methodologies used to obtain field and RELAB spectra were discussed in Chapter 2. All spectral curves, whether they came from sieved samples, field or RELAB, were convolved using a Gaussian filter in order to match the AVIRIS spectral bands.

Field Estimations of Ground Cover

The percent of ground cover was estimated by using a pinpoint method in a 100 m transect with a sampling interval of 1 m. For bare soil and rocks the criteria described in the Soil Survey Manual (1993) was used to separate these two classes and also to separate the different fraction of rocks. Vegetation was separated into three classes: shrub, forbes and grass. Each one of the vegetation classes were subdivided into green, yellow and dark, according to their conditions in the field at the time of the measurement. The litter cover was also subdivided into dark and yellow.

Pre-processing AVIRIS Image.

The AVIRIS instrument was built with the objective of providing a source of data both for addressing a wide range of earth science issues and for developing new methodologies for information extraction from high spectral resolution image data (Vane et al., 1993). The sensor acquires images from the NASA ER-2 high-altitude aircraft in the whisk-broom imaging mode (Vane et al., 1993). The instrument operates in the 0.4-2.45 μm region collecting 224 channels with a nominal spectral bandpass of 10 nm.. After eliminating spectral overlap, there are 210 spectrally unique channels. These and other characteristics of AVIRIS are given in Table 3-1. (Goetz, 1992).

AVIRIS data were collected over the study area on May 14, 1991, with a nominal spatial resolution of 20 x 20 m and a flight height of 20,000 m. The original image was displayed and each band was examined to look for noise. A total of 167 "good" bands resulted from this visual inspection . Table 3-2 presents the list of bands that were eliminated

Table 3-1. General Performance of AVIRIS (Goetz, 1992).

Parameter	Performance
Spectral Coverage	0.40 to 2.45 μm
Spectral Sampling Interval	9.6 to 10.0 nm
Number of Spectral Bands	
Raw Data	220
Radiometrically Corrected Data	210
Instantaneous Field of View (IFOV)	0.95 mrad
Ground IFOV from U-2 Aircraft	20 m
Angular Field of View (AFOV)	30 deg
Ground FOV from U-2 Aircraft	10.5 km
Number of Cross-Track Pixels	
Raw Data	614
Geometrically Corrected Data	550
Data Encoding	10 bits
Data Rate	17 Mbps
Radiometric Calibration Accuracy (Laboratory)	
Absolute	7.3%
Spectral Band-to-Band	0.4%
Spectral Calibration Accuracy	2 nm

Table 3-2. Eliminated channels from the original AVIRIS image of the Walnut Gulch Experimental Watershed.

Channel in the original AVIRIS image	Wavelength (μm)	Reason for the exclusion
1 to 6	0.40-0.45	Noisy
33 to 36	0.68-0.71	Overlapping channels
97 to 101	1.24-1.28	Overlapping channels
108 to 115	1.35-1.42	Noisy. Water absorption bands around 1.4 μm
154 to 174	1.81-1.96	Noisy and overlapping channels (156 to 160)
178 and 179	2.00-2.01	Noisy
212	2.34	Noisy
215 to 224	2.37-2.45	Noisy

from the original AVIRIS data.

The AVIRIS image was registered to the USGS 7.5 minute topographic maps using a polynomial warping. The registration process gave an rms error of 0.62 pixels in the x-axis and 0.68 pixels in the y-axis, and a total rms error of 0.92 pixels. One 3x3 window from each site was used to extract soil reflectance values from the registered and atmospherically corrected image. Pixel values in each AVIRIS band were averaged and used to compare with field, lab and RELAB spectral curves.

The original AVIRIS image came as a scaled radiance image and was processed to continental surface reflectance imagery by using the Atmosphere Removal Program (ATREM) (Gao et al., 1996).

The interactions of incoming solar irradiance with the atmosphere and the surface has been described by Moran et al. (1992) using the following equation:

$$\rho_{g\lambda} = [\pi(L_{s\lambda} - L_{d\lambda}\uparrow) / \tau_{v\lambda}] / [(E_{0\lambda})\cos\theta_z\tau_{z\lambda} + E_{d\lambda}\downarrow] \quad 3.1$$

Where:

$\rho_{g\lambda}$ = spectral reflectance of the surface, after discounting the effects of atmospheric scattering and absorption;

$L_{s\lambda}$ = spectral radiance at the satellite sensor ($Wcm^{-2}sr^{-1} \mu m^{-1}$);

$E_{d\lambda}\downarrow$ = downwelling spectral irradiance at the surface due to scattered solar flux in the atmosphere ($Wcm^{-2} \mu m^{-1}$);

$L_{d\lambda}\uparrow$ = upwelling atmospheric spectral radiance scattered in the direction of and at the sensor entrance pupil and within the sensor's field of view (spectral path radiance) ($Wcm^{-2}sr^{-1} \mu m^{-1}$);

$\tau_{z\lambda}$ = atmospheric spectral transmittance along the path from the sun to the ground surface

where $\tau_{z\lambda} = \exp(-\delta_{\lambda} \sec\theta_z)$ for scattering and weak absorption;

$\tau_{v\lambda}$ = atmospheric spectral transmittance along the path from the ground surface to the sensor,

where $\tau_{v\lambda} = \exp(-\delta_{\lambda} \sec\theta_v)$ for scattering and weak absorption;

δ_{λ} = spectral extinction optical depth;

$E_{0\lambda}$ = solar spectral irradiance on a surface perpendicular to the sun's rays outside the atmosphere ($\text{Wcm}^{-2}\mu\text{m}^{-1}$);

θ_z = angle of incidence of the direct solar flux onto the earth's surface;

θ_v = angle between the line from the sensor to the surface and the normal to the surface of interest

λ = spectral band.

Variation in at-sensor radiances can be reduced greatly by normalizing the radiance signal by the exo-atmospheric solar irradiance, i.e., by expressing the radiances in reflectance units known as apparent reflectance (Huete, 1996). Thus, the first approach used to calibrate the AVIRIS scene to reflectance was the apparent reflectance ($\rho_{g\lambda v}$) defined by Moran et al. (1992) as:

$$\rho_{g\lambda v} = \pi L_{s\lambda} / (E_{0\lambda} \cos\theta_z) \quad 3.2$$

Where:

$L_{s\lambda}$ is the spectral radiance at the sensor ($\text{Wcm}^{-2}\text{sr}^{-1}\mu\text{m}^{-1}$);

v signifies uncorrected (or apparent) reflectance.

The solar spectral irradiance ($E_{0\lambda}$) was given by the MODTRAN radiative transfer code for the transmittance mode (Berk et al., 1989) which also accounted for the solar-illumination geometry by using the latitude, longitude, and time of the AVIRIS data

acquisition over the Walnut Gulch Watershed. MODTRAN was used for a midlatitude, summer, and rural (23 Km visibility) model based on the location and season of AVIRIS data acquisition. A plot of the irradiance values at the top of the Earth's atmosphere, as well as for the 1.5 Km altitude (average for the AVIRIS scene), as a function of the wavelength of the 210 nominal AVIRIS bands for this model is presented in Figure 3-1.

To extract ground reflectance the ATmosphre REMoval Program (ATREM) (Gao et al., 1996) was used. ATREM software derives scaled surface reflectance using an approximate atmospheric radiative transfer model (Gao et al., 1996). The program assumes horizontal surfaces that have lambertian reflectance. The atmospheric scattering effects are modeled in ATREM by using the Simulation of the Satellite Signal in the Solar Spectrum (5S) code (Tanre et al., 1986) with a user selected aerosol model. The transmittances of seven gases are calculated based on an assumed atmospheric model, the solar and observational geometries, and the Malkmus (Malkmus, 1967) narrow band spectral model. For six gases (CO_2 , O_3 , N_2O , CO , CH_4 , and O_2), the algorithm assumes that the amount of gases are uniform across the scene. Only one transmittance spectrum is calculated for each of these gases (Gao et al., 1996). ATREM's algorithm treats the atmospheric water vapor differently. The algorithm derives water vapor values from AVIRIS data in the 0.94 μm and 1.4 μm regions on a pixel by pixel basis using a 3-channel ratioing technique and a look-up table procedure (Gao et al., 1996). An average value of 4,600 feet (1,550 m) for the elevation in the AVIRIS scene was used as input for the ATREM model (details about the ATREM's input card are presented in Appendix A).

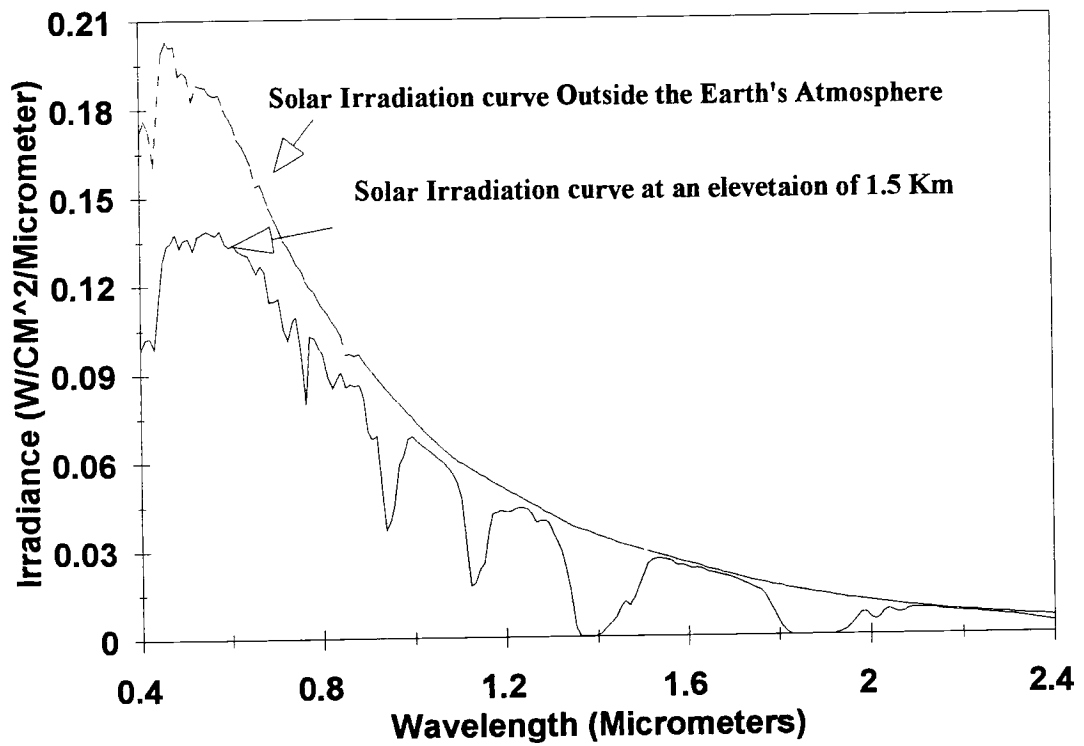


Figure 3-1. Irradiance at the top of Earth's Atmosphere and for 1.5 Km elevation as modeled by MODTRAN and convolved to AVIRIS bands

To check the results of applying ATREM, one of the few "pure" targets found in the AVIRIS scene was selected. Subsurface horizons of the McAllister soil series were exposed after removal of surface horizon. This target had virtually no vegetation and represented an area of about 4 x 5 AVIRIS pixels. The four pixel in the center of this area (UTM coordinates of the upper left corner pixel: 3510400 N, and 592443 W, zone 12) were selected for making measurements with the Spectron instrument (range 0.45 - 0.90 μm).

Dimensionality of the data set

The spectral response of each soil from the sieved samples, field, and RELAB were cluster using the procedure CLUSTER in SAS* (SAS Institute Inc., 1995) to find the group of soils according to their spectral characteristics. The goal in many cluster applications is to arrive at clusters of objects that display small within-cluster variation relative to the between-cluster variation (Dillon and Goldstein, 1984). Cluster analysis was used in this work as a data reduction technique that allowed an easy visualization of how the different soils were grouped in function to their spectral responses.

Cluster formation was obtained by using the unweighted centroid method. In centroid methods the distance between groups is defined as the Euclidian distance between the centroids of the groups. The two groups for which the intercentroid is minimal are then merged. In the centroid method, the distance between two clusters (D_{KL}) is defined by:

$$D_{KL} = \| \bar{x}_K - \bar{x}_L \|^2 \quad 3.3$$

Where:

\bar{x}_K , mean vector for cluster C_K

\bar{x}_L , mean vector for cluster C_L

If the distance of dissimilarity measure between observations (or, in this case variables) or vectors x and y is given by:

$$d(x,y) = \|x - y\|^2 \quad 3.4$$

then the combinatorial formula (SAS Institute Inc., 1995) is:

$$D_{JM} = (N_K D_{JK} + N_L D_{JL}) / N_M - N_K N_L D_{KL} / N_M^2 \quad 3.5$$

Where:

N_K , N_L , and N_M are the number of observations in clusters C_K , C_L , and C_M , respectively.

The study of the dimensionality of the data set in terms of bands was done on RELAB's spectra (range of 0.4 μm to 2.4 μm and sampling interval of 5 nm) by using factor analysis. One of the objectives of factor analysis is to express a data matrix in terms of a minimum number of factors (Malinowski, 1982). Finding "key" bands (as defined by Malinowski 1982) was done for all soil series after removing the bands present in the water absorption regions. The water absorption bands in the intervals 1.35 μm to 1.47 μm and 1.78 μm to 2.01 μm were eliminated and a total of 340 were left for further processing. This study evolved 3 phases: First the number of factors was determined from the original data set using one or more criteria described by Malinoswiki (1982); Second using as input the number of factors the key set of bands, and also the key set of soils were identified after a series of orthogonalization of vectors. A third phase was added with the purpose of

identifying the band interval represented by each of the key bands. The theory for these three steps is given below.

To work with factor analysis, our original data set was first represented by a spectral system matrix containing d rows represented by RELAB's spectral bands and s columns represented by the spectral response of the soils (one column for each soil). This original data matrix is designated as [D] matrix and as $a_{i,j}$ for each element of this matrix which represents the spectral response of soil j in band i . As several soil properties (such as color parameters, soil roughness, soil texture, type and amount of organic material, etc.) contribute differently to the spectral response of each of the soils, the spectral response is expressed as a linear function represented by the summation of the spectral contribution of each of these individual spectral feature. Thus:

3.6

$$d_{i,k} = \sum_{j=1}^n r_{i,j} c_{j,k}$$

Where $d_{i,k}$ is the measured response of soil k in band i , n the number of unique spectral features in the soil population, $r_{i,j}$ is the response of feature j in band i , and $c_{i,k}$ is the contribution of feature j for the spectral response of soil k . Using the matrix notation, equation (3.6) can be rewritten as follow:

$$[D]=[R][C] \quad 3.7$$

where [D] is the experimental data matrix containing the spectral response of each soil for

each of the 340 bands, $[R]$ is the response or eigenspectra matrix of independent "basis" spectral curves (or simply the row matrix, since this matrix is associated with the row designees of the data matrix), and $[C]$ is the eigenvector matrix (also called column matrix) consisting of the contribution of scalar multiples of each "basis" curve to the experimental data.

Factor analysis was initially used to decompose the data matrix D into an abstract (abstract because they constitute mathematical solutions, devoid of any spectral meaning) eigenspectra matrix R_A and an abstract eigenvector matrix C_A such that $[D]=[R]_A[C]_A$. The decomposition of the D is done by solving the eigenvalue problem given by:

$$[Z]_0[C]_A=[\lambda][C]_A \quad 3.8$$

and

$$[Z]_0=[D]^T[D] \quad 3.9$$

Where Z is the covariance about the origin matrix obtained from the original matrix, D , and λ is the diagonal matrix of eigenvalues. The abstract eigenspectra matrix is then constructed according to:

$$[R]_A=[D][C]_A^T \quad 3.10$$

Where $C^{-1} = C^T$ for orthonormal matrices (matrices that have an orthogonal set of unit vectors).

There are several methods for determining the number of factors. Huete (1986) used equation 3.6 in a stepwise procedure to reconstruct the original data matrix. In this procedure he started with only one factor (i.e. $n = 1$, the largest eigenvalue) and at each step he checked the reconstructed data matrix using the real error (RE) or residual standard deviation (RSD) given by:

$$\sum RE = RSD = \left[\frac{\sum_{j=n+1}^c \lambda_j^0}{r(c-n)} \right]^{1/2} \quad 3.11$$

Where r and c are the numbers of rows and columns (with $r > c$) and λ_j^0 is j th error eigenvalue, and n is the number of factors.

In this case the concept of real error is the same as the residual standard deviation which is calculated to provide a measure of the deviation of the regenerated data matrix from the experimental data matrix (RSD) (Malinowski and Howery 1980). Huete and Escadafal (1991) used the residual standard deviation as a criteria to find the factor space needed to fully characterize soil spectra and derive maximum soil information.

Malinowski (1991) suggests some approximate or empirical methods to determine the number of factors for the unknown experimental error in the original data matrix. Among these methods there are the imbedded error function and the factor indicator function.

The imbedded error, which is a function of the secondary eigenvalues, the number of rows and columns, and the number of factors is given by:

$$IE = \left[\frac{n \sum_{j=n+1}^c \lambda_j^0}{rc(c-n)} \right]^{1/2} \quad 3.12$$

Where IE is the imbedded error function and the other variables are as described for the real error.

The factor indicator function (IND) is defined as follow:

$$IND = \frac{RE}{(c-n)^2} \quad 3.13$$

Once the number of factors is determined the key set of bands which best reproduces the original data set must be found. For small data matrices this task can easily be accomplished by testing combinations of row (or column) vector. However, for large data matrices that lie in a factor space greater than three-dimensional, testing every possible combination becomes impractical. Malinowski (1982) showed that the original data matrix, D can be expressed in terms of a key set of typical data rows, D_{key} , chosen from the data matrix itself.

To achieve this, a matrix T must be found so that

$$[D]=[R]TT^{-1}C=[D]_{key}\bar{C} \quad 3.14$$

Where

$$= T^{-1}C \quad \text{and} \quad D_{key} = RT.$$

It is proposed here that the key set of typical rows is that which has the most unique behavior, recognizable as those with relative mixtures of eigenvectors most orthogonal to each other (Malinowski, 1982).

If $V_i = (v_{i1}, v_{i2}, \dots, v_{in})$ is the i th row vector of the abstract row-factor matrix after normalization; v_{ik} would represent the relative importance of k th eigenvector on the direction of the i th row. The first key row is that row which contains the least relative amount of the first eigenvector (i.e., the row with v_{i1} closest to zero). Each eigenvector which emerges from factor analysis successively accounts for a maximum variation in the residual data. Thus, the first eigenvector is most important, the second eigenvector is next most important, and so on. To obtain the second key row, only the first two components of each normalized row vector are considered because these components are associated with the two most important eigenvectors. Hence, the j th row with $V_j = (v_{j1}, v_{j2})$ is most orthogonal to the first chosen row vector, V_i , in two-dimensional space will be the second key row point. In other words, the dot product between V_i and V_j should be a minimum in the two-dimensional subspace (Malinowski and Howery, 1980).

To obtain the third key row, only the first three components of the normalized row vectors are considered. The third key row will be that which is most orthogonal to the plane defined by the first two chosen row vectors expressed in three-dimensional space. This is accomplished by recognizing that the cross product between the first two chosen row vectors is a vector perpendicular to the plane, hence the dot product between this vector and the most orthogonal row vector will be farthest from zero.

In a similar manner, each successive key row can be extracted from the normalized row matrix. In general, the m th key row is that row vector which makes the value of the determinant constructed from itself and the previously chosen key rows farthest from zero in m th space, i.e.,

$$\det \begin{vmatrix} v_{i1} & v_{i2} & v_{im} \\ v_{j1} & v_{j2} & v_{jm} \\ v_{m1} & v_{m2} & v_{mm} \end{vmatrix}$$

is farthest from zero (Malinoswiki and Howery, 1980)

In this Chapter the analysis of the dimension of the data set in terms of the number of soil and bands was performed simultaneously with the identification of the key soil and the key band vectors.

Results and Discussion

Comparing Field, Lab, and AVIRIS Image Spectra

Figure 3-2a presents a comparison between ground reflectance values obtained for the "pure" target with ATREM reflectance values for the same target. The calibration with ATREM code presented a good fit for the measured spectral range (0.45 - 0.90 μm). The good agreement of ATREM code can be better interpreted by the ratio according to the wavelength of ATREM and the measured ground reflectance presented in Figure 3-2b. The results shows that for this spectral range the deviation of ATREM from the measured field spectra range from -7.% (ratio of 0.93) to 5% (ratio of 1.05). The greater deviations are due to ATREM's overcorrection at secondary water absorption bands located near 0.72, 0.82, and 0.9 μm and also due to O_2 absorption band near 0.75 μm .

Figures 3-3 and 3-4 present the spectral curves for field, sieved samples, RELAB, apparent reflectance and atmospherically corrected AVIRIS, using the radiative transfer code (RTC) ATREM for the intervals 0.45 to 0.90 μm and 0.90 to 2.45 μm , respectively. Spectral curves from field, sieved samples, RELAB, apparent reflectance and ATREM are different in shape and magnitude. The curves from the radiative transfer model and from the apparent reflectance represents the spectral contribution not only from soil but also from other types of materials detected by the evaluation of the percent of cover (Table 3-3). The algorithm above described for ATREM was believed to better remove the remains of water vapor, however, other authors (Verdebout et al., 1993; Huete, 1995) report the same characteristic peaks in the NIR region in spectra extracted from bare soil and brown fields and pointed out

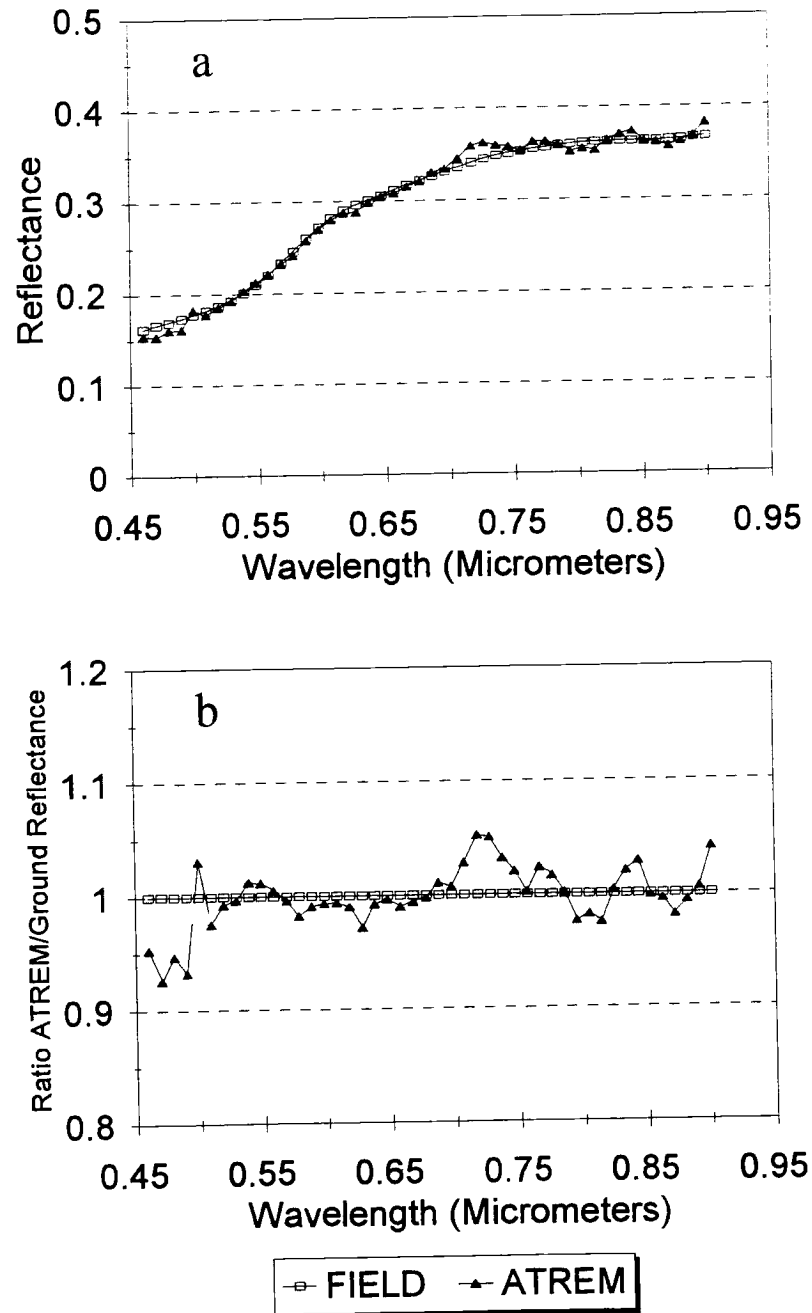


Figure 3-2. Calibration results for ATREM radiative transfer code

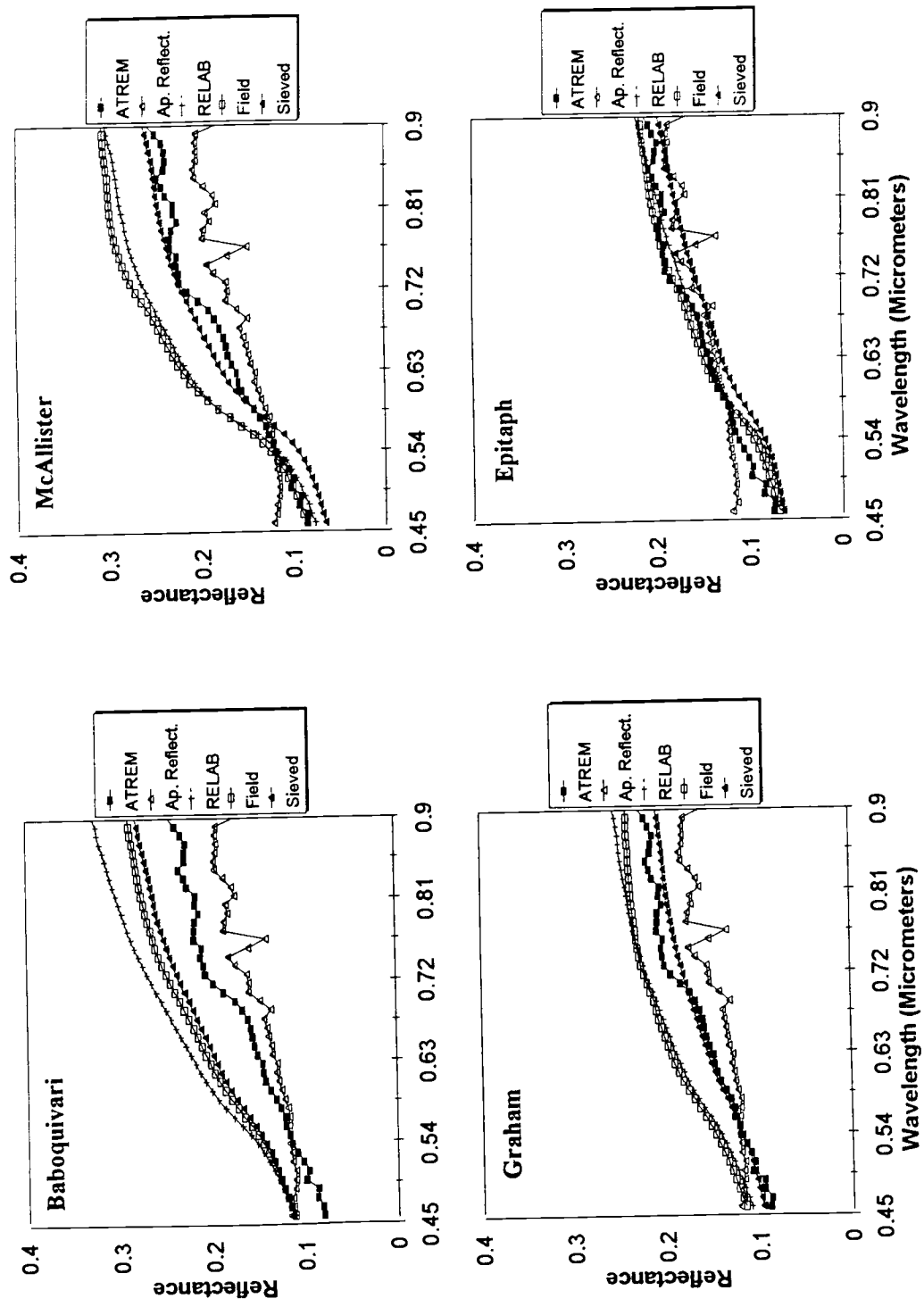


Figure 3-3. Comparison between soil spectra obtained from AVIRIS data (ATREM and apparent reflectance), field, sieved samples, and RELAB data (0.45 to 0.90 micrometers)

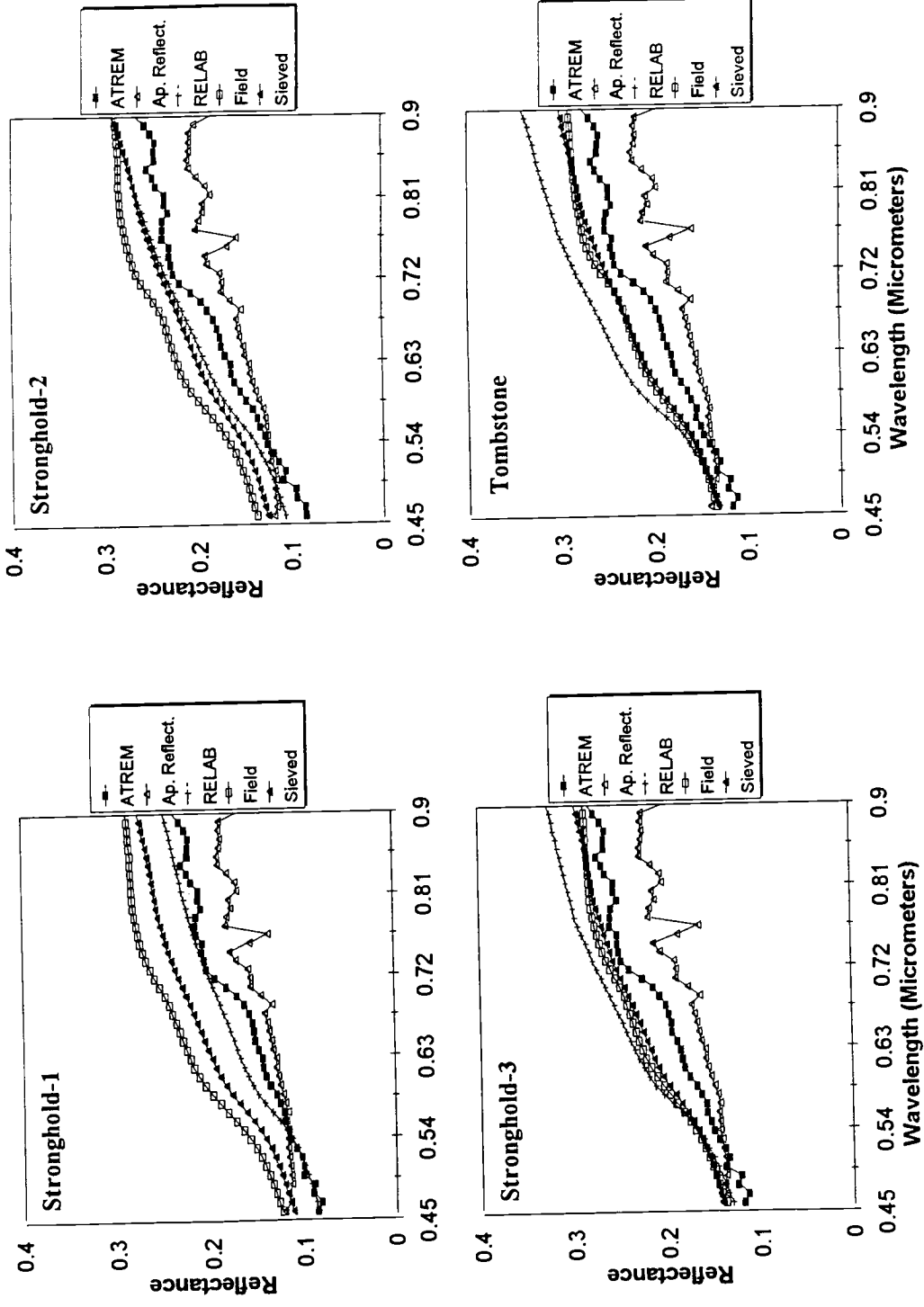


Figure 3-3. Comparison between soil spectra obtained from AVIRIS data (ATREM and apparent reflectance), field, sieved samples, and RELAB data (0.45 to 0.90 micrometers) (cont.)

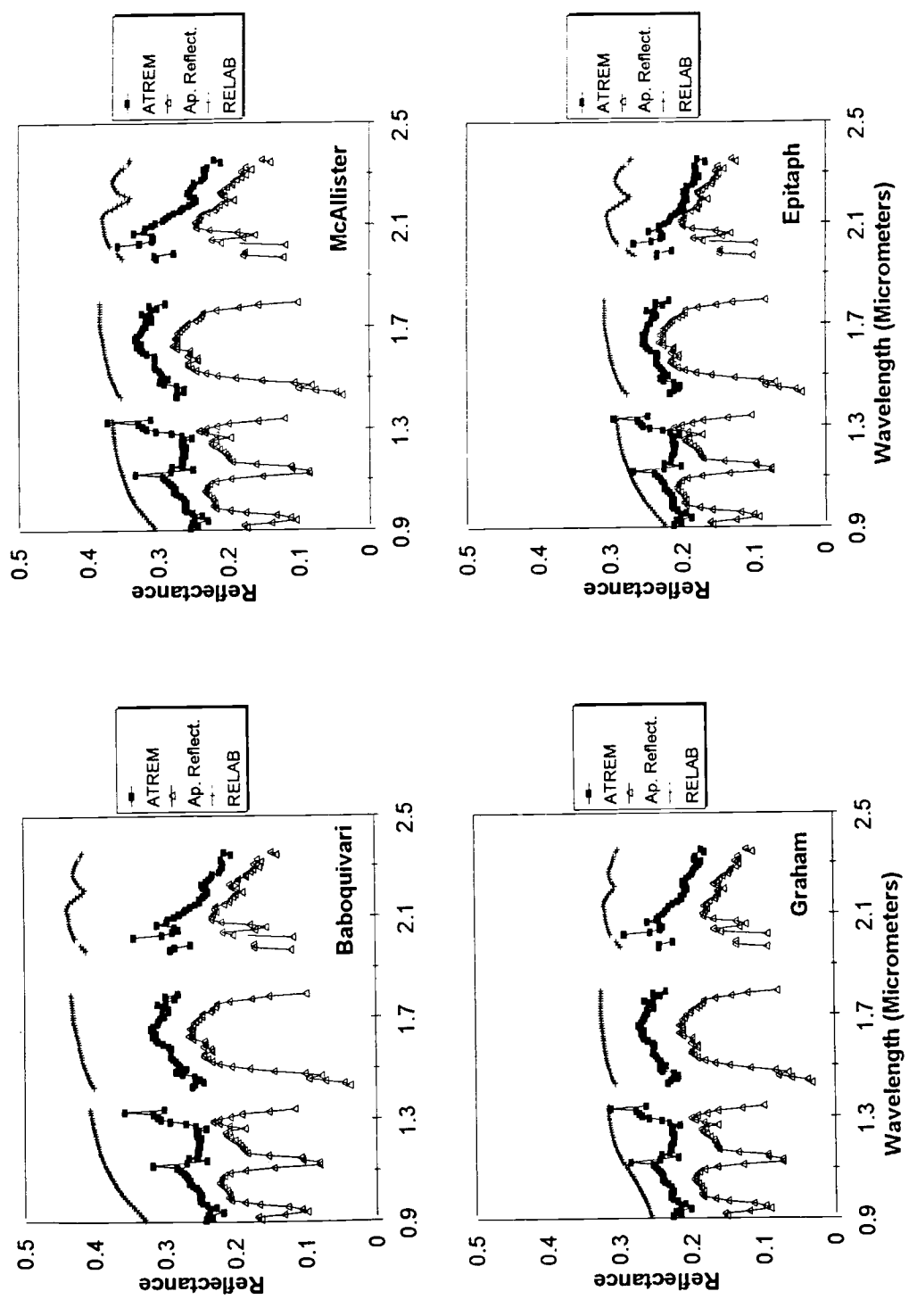


Figure 3-4. Comparison between soil spectra obtained from AVIRIS data (ATREM and apparent reflectance), and RELAB data (0.90 to 2.45 micrometers)

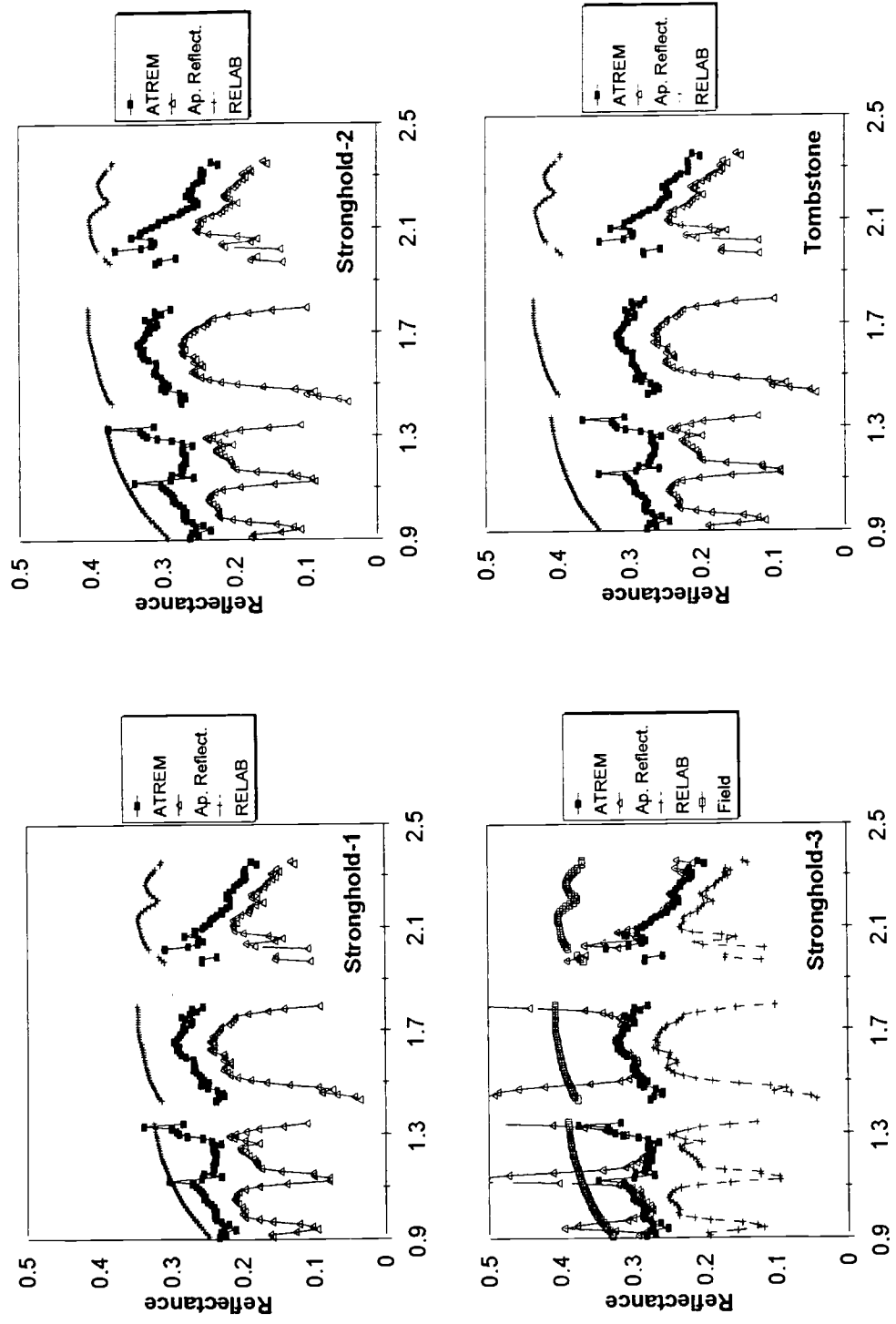


Figure 3-4. Comparison between soil spectra obtained from AVIRIS data (ATREM and apparent reflectance), and RELAB data (0.90 to 2.45 micrometers) (cont.)

Table 3-3. Percent of cover type in the transect of each soil.

Cover Type	Soil Number ⁽¹⁾							
	1	2	3	4	5	6	7	8
	Percent of Cover							
Bare soil	21.7	4.0	10.4	15.0	5.3	8.4	3.2	4.3
Rock Fragments	10.3	30.3	37.4	40.3	30.3	35.7	30.5	21.3
- Fine Gravel	7.8	13.4	19.3	1.3	11.7	2.7	1.3	2.3
- Medium Gravel	2.7	14.4	15.4	2.7	16.3	4.7	13.1	13.7
- Coarse Gravel	-	2.7	2.7	4.7	2.3	5.4	11.3	4.0
- Cobbles	-	-	0.7	21.7	-	17.4	4.0	1.0
- Stones	-	-	-	9.3	-	5.0	0.3	0.3
- Boulders	-	-	-	0.7	-	0.7	-	-
Vegetation	51.0	45.4	45.0	34.7	51.7	53.0	55.3	57.0
- Shrub	4.4	15.3	4.3	4.7	30.0	8.0	1.7	31.0
Green	4.4	9.7	1.0	0.7	15.3	1.7	1.3	20.7
Yellow	-	0.4	-	-	-	-	0.3	0.3
Dark	-	5.2	1.4	4.0	14.7	6.4	-	10.0
- Forbes	32.4	26.7	-	19.0	18.7	5.4	36.3	26.0
Green	12.0	9.0	15.0	-	6.7	-	9.3	6.0
Yellow	10.4	13.7	14.4	4.0	7.3	4.7	15.3	6.7
Dark	10.7	4.0	10.4	15.0	4.7	1.0	13.7	16.7
- Grass	13.7	3.4	0.7	11.0	3.0	39.5	17.3	-
Green	-	-	-	-	-	-	.3	-
Yellow	12.7	3.4	0.7	9.3	2.7	31.5	17.0	-
Dark	1.0	-	-	1.3	0.3	8.0	-	-
Litter	16.3	20.3	6.7	10.0	12.7	3.0	5.0	17.3
- Yellow	5.3	14.0	3.4	2.7	4.7	2.0	1.3	0.3
- Dark	11.0	6.3	3.3	7.3	8.0	1.0	3.7	17.0

⁽¹⁾ Soil numbers are: 1 = Baboquivari, 2 = McAllister, 3 = Stronghold-1, 4 = Graham, 5 = Stronghold-2, 6 = Epitaph, 7 = Stronghold-3, 8 = Tombstone.

that a slight error in the wavelength calibration file can cause such small disturbance in the ATREM spectral curves. Noise associated with uneven corrections of water absorption bands are more evident in ATREM's curves at 0.94 and 1.15 μm (Figure 3-4).

Apparent reflectance curves presented higher values for blue and green regions than ATREM radiative transfer code (Figure 3-3). The highest difference was found in 0.46 μm with an increase in relation to ATREM's results that varied from 21% for Tombstone and Stronghold-3 to 60% for Epitaph. The increase in reflectance values for the extreme portion of the short wavelengths was caused mainly by the great contribution of molecular scattering in this portion of the spectrum which was not removed by using apparent reflectance. The presence of molecular scattering in apparent reflectance curves tended to reduce the spectral differences between soil series, mostly in the blue region of the spectrum. Those differences were reduced because the contribution of molecular scattering was not the same for bright and dark target. Thus, for Epitaph soil series, which had very low values of reflectance in the blue region, the contribution of molecular scattering can reach values 60% over ATREM's results, while for Tombstone and Stronghold-3, which have relatively high values for reflectance in the blue region, this contribution is at most 21% of ATREM's results. These results, although not tested, could affect mixture analysis if image endmembers are taken into account.

Soil spectral information was also reduced as a result of the influence of molecular scattering on apparent reflectance. One example of losing information was related to iron and iron-oxide content in soils which presented a decrease in reflectance values in the blue region of the spectrum as the iron content increased (Irons et al., 1987). From about 0.54 μm

the reflectance values for apparent reflectance became less than that found for ATREM for most of the soils. However, for dark soils, such as Epitaph, values of apparent reflectance remained higher than that found for radiative transfer codes for longer wavelengths.

Compared to ATREM, the reduction in apparent reflectance values for wavelengths longer than 0.54 μm (excluding regions more affected by water absorption bands) varied from 15% in the NIR to 34% in the mid infrared for Graham soil series and from 7% to 25% for NIR and mid infrared respectively, for Epitaph soil series (Figures 3-3 and 3-4). Moran et al. (1990), found that the apparent reflectance taken on a fallow field by the HRV sensor (mounted in SPOT-1 satellite) tended to overestimate surface reflectance in band XS1 (0.50 - 0.59 μm) and underestimate in band XS3 (0.79 - 0.89 μm). However for band XS2, located in the interval of 0.61 - 0.68 μm , Moran et al. (1990) found that apparent reflectance was either underestimated or overestimated, illustrating the interplay of path radiance and atmospheric radiance as a function of reflectance. Even though there was lost of information (mostly in the blue region of the spectrum) when the spectral curves from ATREM radiative transfer code and from the apparent reflectance curves were compared, some absorption features, such as the kaolinite doublet at 2.2 μm , were preserved in the apparent reflectance curves. These results agreed with Huete (1996) who found that soil spectral signatures that were contaminated with atmosphere tended to present higher blue and green responses and were attenuated by gas absorption, particularly the secondary water vapor absorption bands, such as at 0.92 and 0.83 μm , and by the oxygen band near 0.76 μm .

When considering the spectral curves obtained under field and sieved conditions, field spectra presented higher reflectance values than sieved sample spectra for six of the eight

soil samples (Baboquivari, McAllister, Stronghold-1, Graham, Stronghold-2, and Epitaph) while they were about the same for Stronghold-3 and Tombstone (Figure 3-3). Field and sieved sample spectra were also compared to RELAB spectra for the 0.45 to 0.90 μm interval. Sieved sample spectra and RELAB spectra for the 0.45 to 0.90 μm interval were featureless when compared to field spectra.

Dividing the spectral response obtained in the sieved samples or RELAB conditions by the spectral response obtained on the field allows for identification of the spectral regions in which the greatest magnitude of difference occurred. The ratio also permits to identify if the spectral response obtained in sieved samples or RELAB conditions are directly proportional to that found under field conditions. Figure 3-5 presents the spectral curves for the ratios: sieved/field, RELAB/field, and RELAB/sieved. Only for the Baboquivari soil sample was the RELAB spectra greater than the field spectra for the whole wavelength range. For McAllister, Epitaph, Stronghold-1 and Stronghold-2 RELAB spectra were less than field spectra for the whole wavelength interval. For the remaining soils (Graham, Stronghold-3 and Tombstone), the ratio RELAB/field varied from values less than 1 to greater than 1 according to the wavelength.

The literature results comparing field and lab spectra are somewhat contradictory. Curran et al. (1990) presented results showing that the spectral-brightness coefficient or SBC (the Russian version for spectral reflectance) obtained in the laboratory were between 1.5 and 3 times higher than those measured in the field. The same authors (Curran et al., 1990) reaffirm that the SBC measured in the laboratory was, in general, higher than that measured under field conditions because of a difference in environmental conditions and analytical

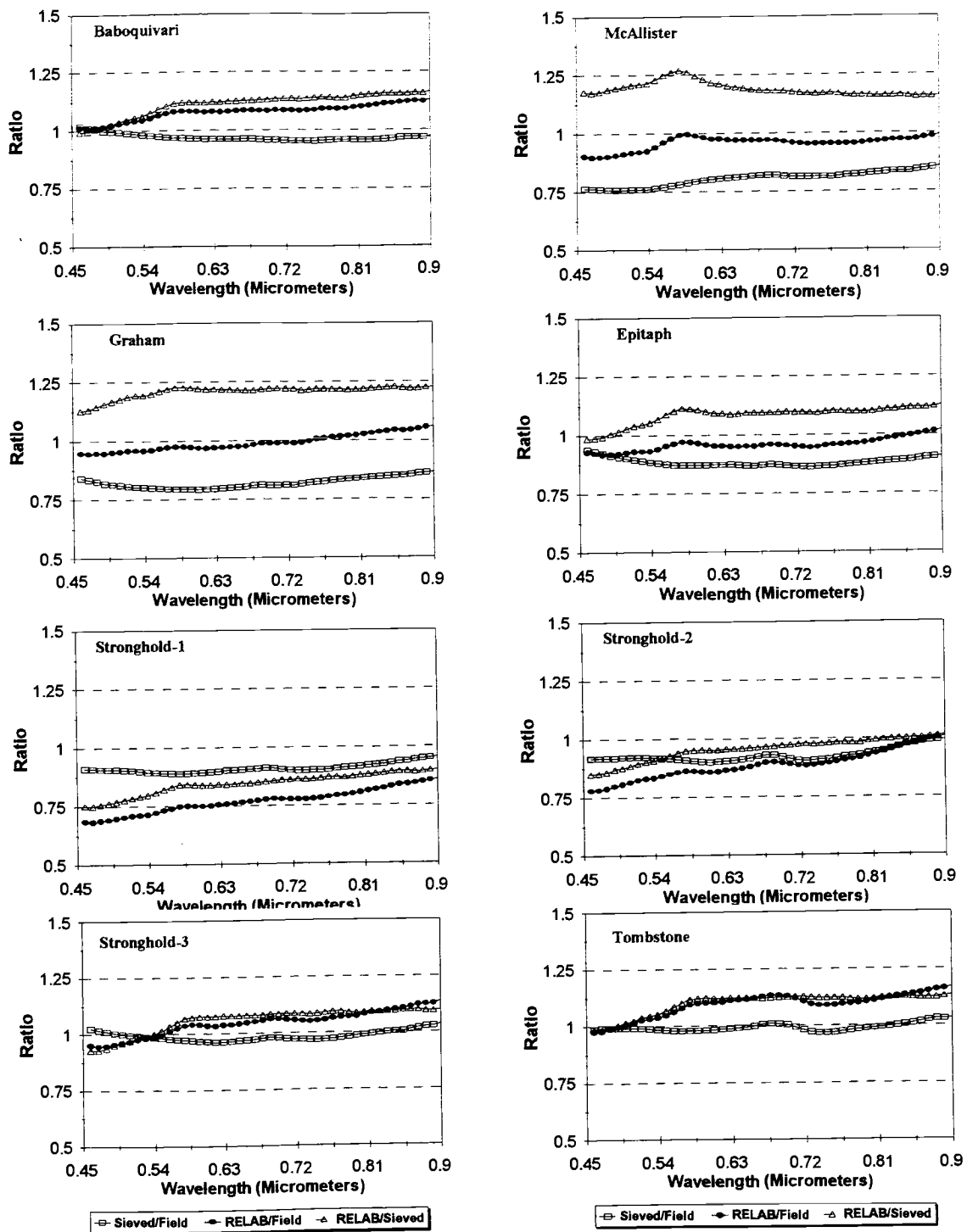


Figure 3-5. Magnitude of the differences between Sieved sample, Field, and RELAB as demonstrated by the spectral ratios

procedures. On the other hand, Stoner et al. (1980) showed that the field reflectance for two soils - Chalmers silty clay loam, a fine-silty, mixed, mesic Typic Haplaquoll, and Fincastle silt loam, a fine-silty, mixed, mesic Aeric Ochraqulf - as measured under bare moist field conditions- was found to be about 1.5 times greater than the reflectance of laboratory (measured in moist soils at 0.10-bar tension) at any given wavelength in the 0.52 to 2.32 μm interval.

Both sieved sample and RELAB spectra were not directly proportional to field spectra, which means that spectral features obtained under field conditions were lost after sieving the samples and their spectral response was measured under controlled conditions.

Departures from field spectra presented by sieved samples and RELAB spectra differ from soil to soil. Those differences are probably associated with the distribution and composition of soil surface materials, such as litter, rock fragments greater than 2 mm, which are left out in different proportion for each soil when preparing the samples, and also due to soil surface characteristics that were disturbed in the process of sampling (such as surface roughness, soil crust, soil structure, etc). Thus, when comparing the ratio of sieved sample and RELAB to field results with the ratio of RELAB to the sieved samples (for the interval between 0.6 and 0.9 μm) we can see that the curves tend to present a constant value for the ratio for most of the soils (Baboquivari, Graham, Epitaph, Stronghold-3, and Tombstone). For the interval 0.45 to 0.60 μm , however, the ratio RELAB/sieved increased almost linearly (Figure 3-5). These results differed in part from that reported by Stoner et al. (1980) who found that laboratory-measured spectra of soils at 0.10-bar tension were directly proportional to the spectral response of the same soil when measured in the field under bare moist

conditions.

One probable reason for the higher spectral values in field spectral curves was the presence of surface crust, which is very common in many of desert soils. Soil surfaces that have crust tend to present higher surface reflectance values in the 0.43 - 0.83 μm wavelength region than soils with the crust broken (Cipra et al., 1971).

Comparisons between field, sieved sample, and RELAB spectra with the results presented by ATREM, or apparent reflectance are complicated by the fact that it was not possible to locate pure pixel in any one of the field sample locations. In general the radiative transfer model, ATREM, presented lower reflectance values than field, sieved sample or RELAB results. The type of covers and their distribution (Table 3-3) have an important role in soil spectral response in a mixed pixel. Most of these soil cover represented dark materials, such as litter and dry vegetation, which tended to have much more influence on bright soils, such as Stronghold and Tombstone, than on dark soils, such as Epitaph.

Comparing Field, Sieved Samples, RELAB, and AVIRIS Using Derivative Spectroscopy

Ratios are more adequate for extracting information about the magnitude of the differences between spectral responses. However when dealing with curve shape in image spectroscopy, one valuable way of enhancing subtle differences in absorption features is the use of first derivative. Derivative spectroscopy is a simple yet powerful technique for magnifying the fine structure of spectral curves. It consists of calculating the first, second, or higher order derivative of a spectrum with respect to wavelength or frequency and plotting the derivative rather than the spectrum itself (Cahill, 1979; Whitbeck, 1981). Derivative

curves can also be used to resolve bands that are too close to be resolved in their zero-order absorption spectra (Cahill, 1979).

Derivative spectroscopy was used to evaluate subtle differences in absorption bands in the region between 0.45 μm and 0.90 μm for RELAB, field, sieved, and AVIRIS spectral curves and in the interval between 0.90 and 2.4 μm for AVIRIS and RELAB data. The derivative of a spectrum is its rate of change with respect to wavelength and can be represented by the equation:

$$\text{Derivative} = (\rho_{\lambda_n} - \rho_{\lambda_{n-1}}) / (\lambda_n - \lambda_{n-1}) \quad 3.15$$

Where ρ and λ are reflectance and spectral band, respectively.

This approach is very sensitive to the slope variations of a spectrum and has been used for several authors for extracting information about vegetation conditions (Ambrosia et al., 1991; Chen et al., 1993; Curran and Kupiek, 1995) and by others to extract information about the amount of iron oxide minerals in soil samples (Kosmas et al. 1984; Escadafal, 1994) and to evaluate desert soil degradation (Escadafal, 1994). Spectral flat profiles (either plateaus or troughs) have a derivative value of "0" while negative derivative values represent a decreasing slope value with increased wavelength. Positive values are indicative of an increasing spectral slope with concurrent wavelength increased.

As some amount of noise still remains in AVIRIS spectral curves, after applying ATREM radiative transfer code, those curves were smoothed before taking the first derivative by convolving them using a 5 band moving average. The procedure of smoothing hyperspectral curves has been used by several authors to reduce noisy spectra to extract information from hyperspectral data set (Chen and Elvidge, 1993; Chen et al., 1992;

Demetriades-Shah et al., 1990). Figure 3-6 presents the results of smoothing each of the AVIRIS soil spectra for the range of 0.45 to 0.90 μm and for the range of 0.90 to 2.4 μm . The noisy spikes caused by ATREM's overcorrection 0.45 to 0.90 μm wavelength region were effectively removed by the moving average algorithm, which, in turn, improved further comparisons when using a first derivative spectra. For the 0.90 to 2.4 μm spectral region peaks due to water vapor features still remained in the smoothed curves.

Figure 3-7 presents the first derivative spectra for the intervals of 0.45 to 0.90 μm . A major feature, occurring in all soil samples in the interval between 0.55 and 0.60 μm was characterized by a peak in this interval (precisely at 0.57 μm) present in RELAB, field and sieved sample first order derivative spectra. For field and sieved sample first derivative spectra a second consecutive peak appeared at 0.59 μm . Some soils, such as Graham and Epitaph present a much less pronounced peak in the region of 0.55 to 0.60 μm . The distinctive character of these two soils in relation to the other soils is their degree of development and parent material (Breckenfeld, 1995).

McAllister, Stronghold and Tombstone soil series are well developed soils located in fan terraces which are the oldest and most stable landform developed during the early Pleistocene to early Holocene (Breckenfeld, 1995). In these soils there was enough time and conditions for the weathering process to transform Fe(II) silicate minerals in iron oxides. On the other hand, for soils developed on hill and mountain landforms, such as Epitaph and Graham, the degree of development was highly dependent on the nature of the bedrock such as the chemical composition, grain size and hardness (Breckenfeld, 1995). The secondary Fe oxides are the most important pigment agents in soils having a low content of organic matter

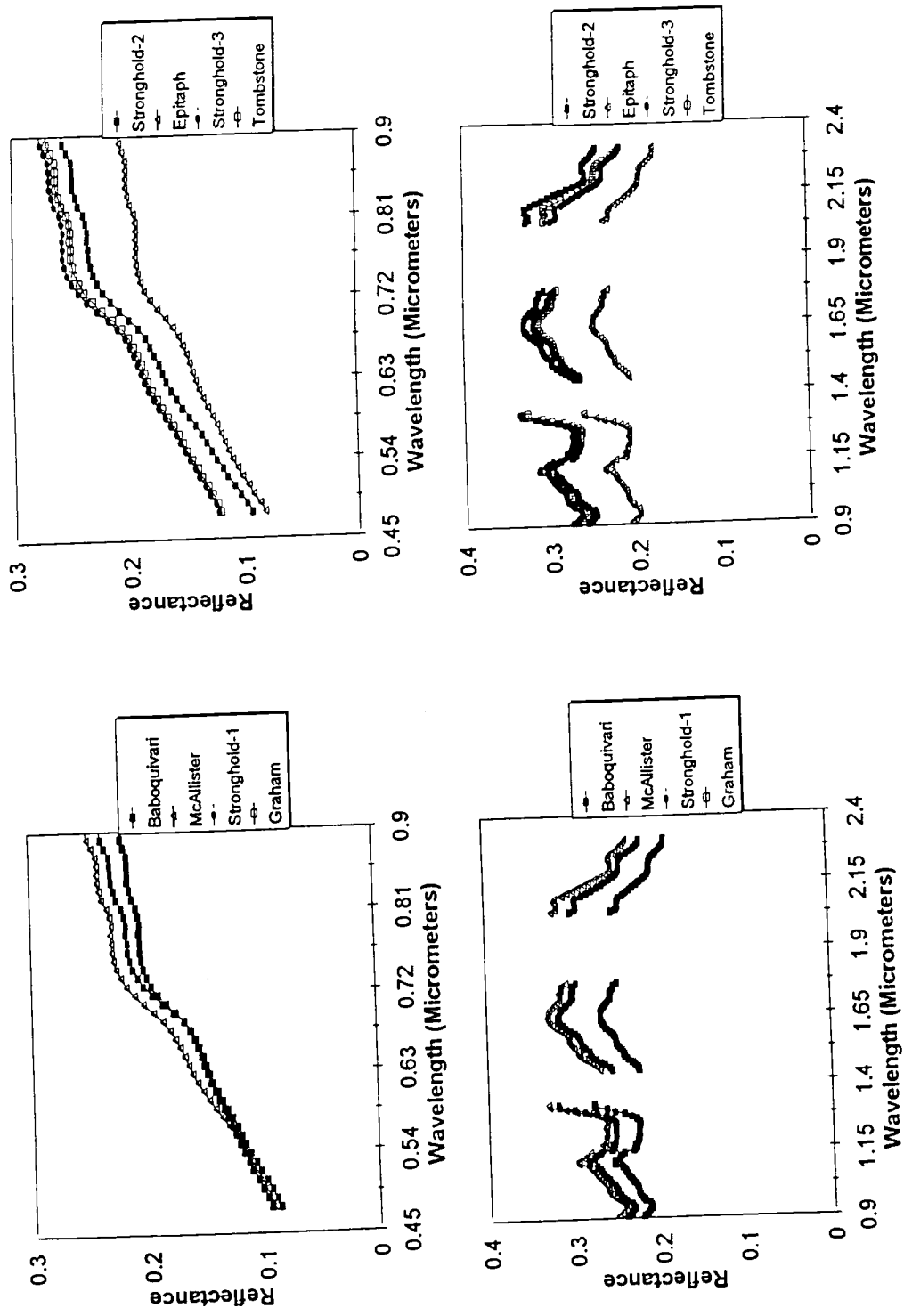


Figure 3-6. Soil spectral curves extracted from AVIRIS after smoothing for 0.45 to 0.90 micrometers (upper) and for 0.90 to 2.40 micrometers (below)

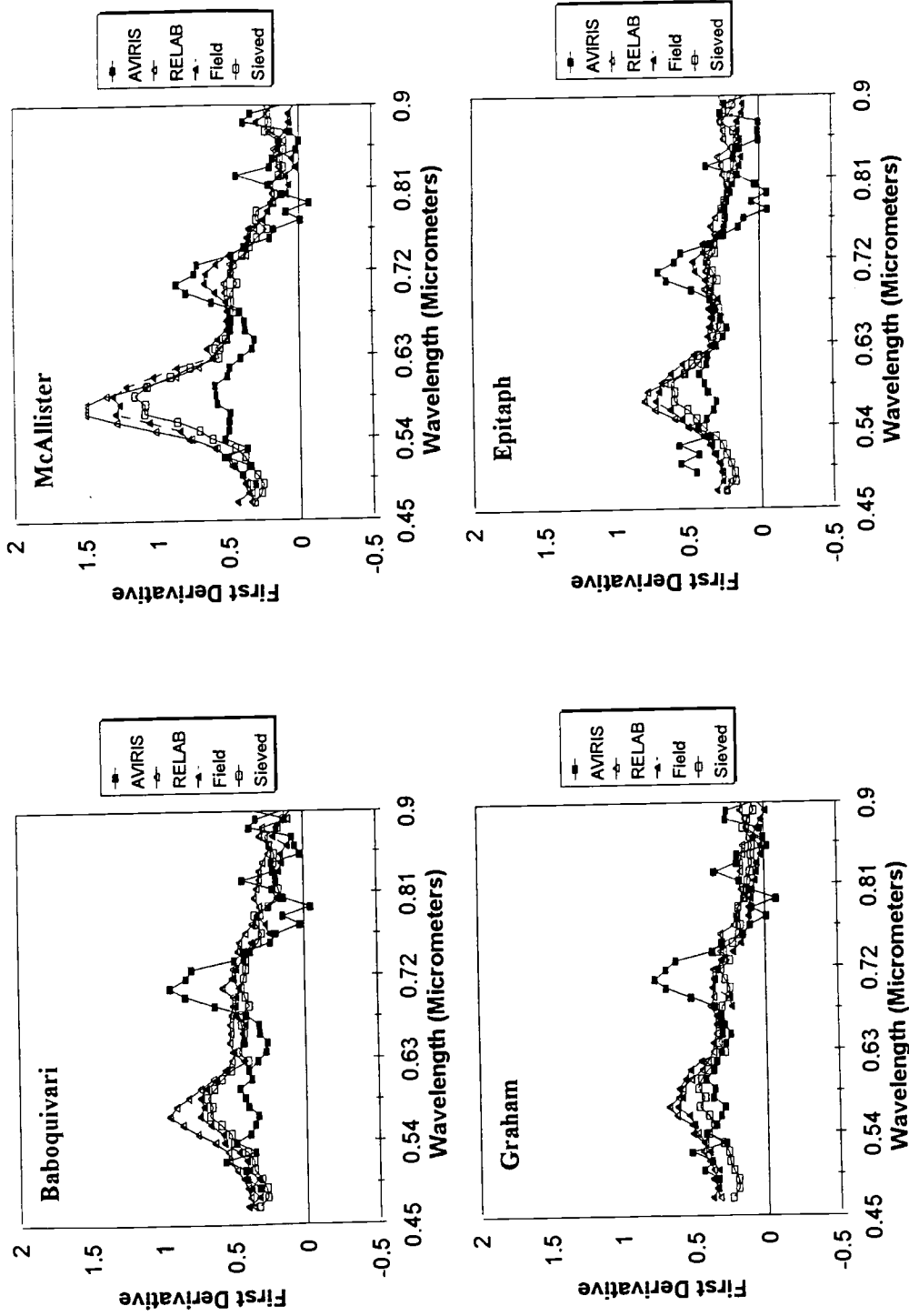


Figure 3-7. Comparison between the first derivative for AVIRIS, RELAB, field, and sieved sample for the interval 0.45 to 0.90 micrometers

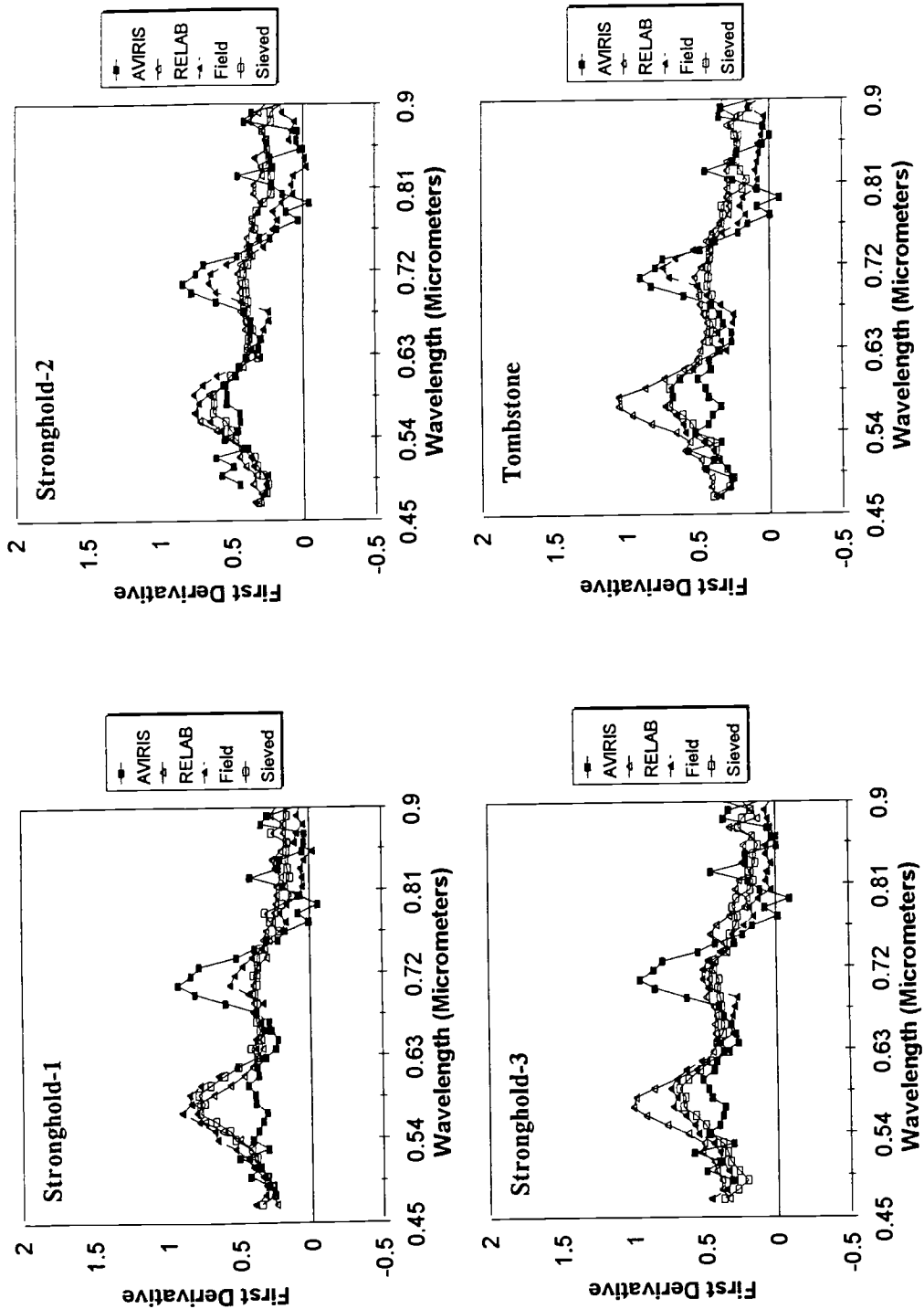
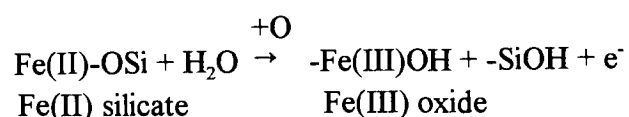


Figure 3-7. Comparison between the first derivative for AVIRIS, RELAB, field, and sieved sample for the interval 0.45 to 0.90 micrometers (cont.)

(Torrent et al., 1983). Goethite (yellowish brown) and hematite (red) are very common in soils, whereas ferrhydrite (reddish brown), lepidocrocite (orange), and maghemite (reddish brown) are less abundant (Torrent et al. 1983). In a negative sense, the lack of Fe(III) oxides indicates the important pedogenic processes of Fe reduction and subsequent removal, thereby leaving the grey colors of the silicate matrix behind (Schwertmann, 1985). Schwertmann (1985) shows that the primary reaction through which Fe(III) oxides are formed is the hydrolytic and oxidative decomposition of Fe(II)-containing primary minerals (mainly Fe(II) silicates):



The degree to which this irreversible reaction has taken place is useful for characterizing the degree of weathering. It varied widely between weakly and strongly developed soils and can be measured by the ratio of dithionite-soluble Fe to total Fe (Schwertmann, 1985). The formation of hematite-goethite is associated with rapid decomposition of organic matter due to higher temperatures, neutral pH (calcareous soils) and good aeration (Schwertmann and Taylor, 1977).

Soils containing exclusively, or almost exclusively, goethite have yellowish brown colors (10YR to 2.5Y Munsell hue; Munsell Color Co. 1975), but, when hematite is present colors usually become reddish (7.5 YR and redder) (Bigham et al., 1978), because the red color of hematite is very effective in masking the yellow color of goethite. Resende (1976) reported that the Munsell hue of a yellow Oxisol was altered from 10YR to 5YR when 1%

fine hematite was added. Escadafal (1994) showed that the size of the peaks observed in the region between 0.50 and 0.60 μm in the first derivative of iron affected soils is related to the "concentration" of the iron oxide considered (goethite or hematite). Escadafal (1994) stated that the first derivative expressed only the apparent content, since the size and distributions of oxides grains vary largely among soils, but, when considering a limited range of soils, quantitative relationships can be established.

Figure 3-8 shows the spectral response and the first order derivative spectra for samples of goethite, hematite, and, also, for a green leaf, convolved to AVIRIS bands in the interval between 0.45 to 0.90 μm . The spectra were obtained from the splib04c.spl spectral library file from the USGS and corresponds to the samples WS222, GDS76, and ABSREF950, for goethite, hematite, and green leaf of walnut tree, respectively.

Comparisons between the intensity of the feature present in the first derivative spectra at about 0.57 μm (Figure 3-7) to that of hematite for the same wavelength (Figure 3-8) agrees with the fact that McAllister is the reddest (and the oldest) soil series in the Walnut Gulch Watershed landscape. On the other hand, the much less pronounced peak in 0.57 μm wavelength agrees with the fact that Graham soil series has color hue much more toward the yellowish color than any other soil. For Graham, and in some extent also for Epiaph, the first derivative curves tend to be much flatter throughout the 0.45 to 0.90 μm interval than any other soil first derivative spectra. On the other hand, Tombstone and Stronghold soil series have mixed calcareous fan alluvium as their parent material and are among the oldest soils in the Walnut Gulch Watershed landscape which also could imply relatively more iron oxide content than what would be expected for Graham and Epiaph soil series. The two soil series

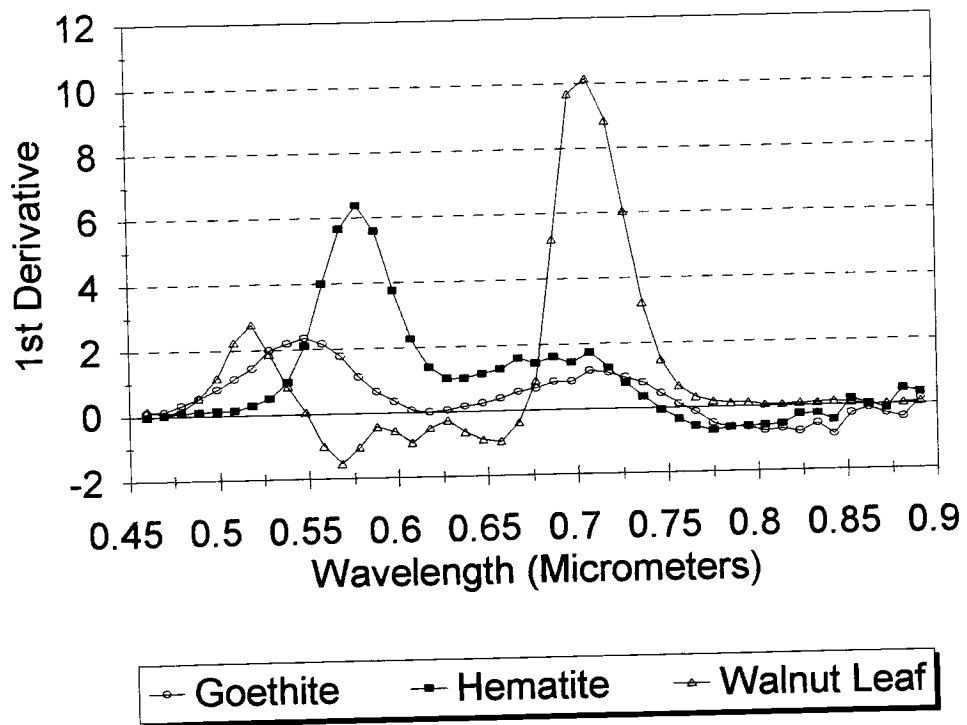


Figure 3-8. First derivative spectra for Goethite (Sample WS222-USGS), Hematite (Sample GDS76-USGS), and walnut leaf (Sample ABSREF950-USGS)

(Tombstone and Stronghold) also presented for RELAB, field and sieved sample first derivative spectra a pronounced peak in the region at the wavelength of 0.57 μm . Even though the atmospherically corrected AVIRIS curves showed some differences in the behavior of spectral curves for these two extreme cases (McAllister x Graham), the differences in the intensity of peak at 0.57 μm for these two soil was much less than that obtained for RELAB, field or sieved sample spectra. These results show clearly a loss of information related to the iron influences on soil first derivative spectra when moving from a large scale data set (RELAB, sieved sample, and field spectra) to a small scale data (AVIRIS).

Another major feature is enhanced by the first derivative spectral curves in the region of 0.70 to 0.75 μm . This feature appeared in a variable degree of magnitude for the first derivative spectra from AVIRIS and from field. This feature was attributed to the high sensitivity of the first derivative spectra to vegetation conditions. Although field sites were selected in a way to obtain the best representative bare soil spot, a few remains of vegetation (in which removal or clipping could cause more damage to soil information extraction) were allowed as long as they represented less than 5% of the field of view of the instrument. The results presented in Figure 3-7 for field first derivative spectral curves, show how great is the enhancement of the red edge when first derivative spectra were used. The red edge detection was minimal for Baboquivari, Graham, and Epitaph field samples, and maximum for Tombstone, and Stronghold-2 samples. To compare the graphical presentation of the variation in vegetation in field samples given by the first derivative spectra with two of the most traditional vegetation indices, Table 3-4 presents the values for NDVI and SAVI data

Table 3-4. NDVI and SAVI values for the field samples. Field spectral responses were convolved to TM and AVIRIS bands.

Field Soil Sample	NDVI		SAVI	
	AVIRIS	TM	AVIRIS	TM
Baboquivari	0.117	0.122	0.088	0.091
MacAllister	0.110	0.119	0.086	0.092
Stronghold-1	0.091	0.095	0.070	0.072
Graham	0.069	0.075	0.048	0.052
Stronghold-2	0.098	0.101	0.074	0.077
Epitaph	0.126	0.133	0.080	0.084
Stronghold-3	0.084	0.089	0.065	0.068
Tombstone	0.105	0.113	0.080	0.086

convolved to AVIRIS bands and to the broad TM bands for field spectral curves taken under dry conditions. NDVI and SAVI (Huete, 1987) are defined as follow:

$$\text{NDVI} = (\text{NIR} - \text{Red}) / (\text{NIR} + \text{Red}) \quad 3.16$$

$$\text{SAVI} = [(\text{NIR} - \text{Red}) / (\text{NIR} + \text{Red} + 0.5)] * 1.5 \quad 3.17$$

Gamon et al. (1995) procedures were followed when deciding to select bands number 28 (0.667 μm) and band 49 (0.833 μm) from AVIRIS data as the best choice for the red and NIR bands, respectively.

As can be seen, both vegetation indices appear to have low sensitivity to very low amounts of vegetation. As an example for Tombstone field sample the first derivative spectrum indicated this soil had more green vegetation than any other soil. However, the NDVI and SAVI indices indicated that Tombstone had less green vegetation than Baboquivari which had virtually no presence of red edge in its field first derivative spectrum.

As would be expected AVIRIS first derivative spectra presented pronounced peaks at about 0.70 μm as a result of the presence of vegetation at the pixel scale. Further comments on AVIRIS results as related to the amount of vegetation are presented in Chapter 4.

Figure 3-9 presents a comparison between AVIRIS and RELAB first derivative reflectance curves for the spectral range of 0.9 to 2.4 μm . Most of the AVIRIS features located in the interval from 0.9 to 1.4 μm are due to remains of water vapor bands not completely removed from the ATREM code. As can be seen in RELAB's first derivative curves no absorption feature occurred in the interval of 0.9 to 2.4 μm for soil spectra. The only exception is the absorption feature in 2.2 to 2.3 μm .

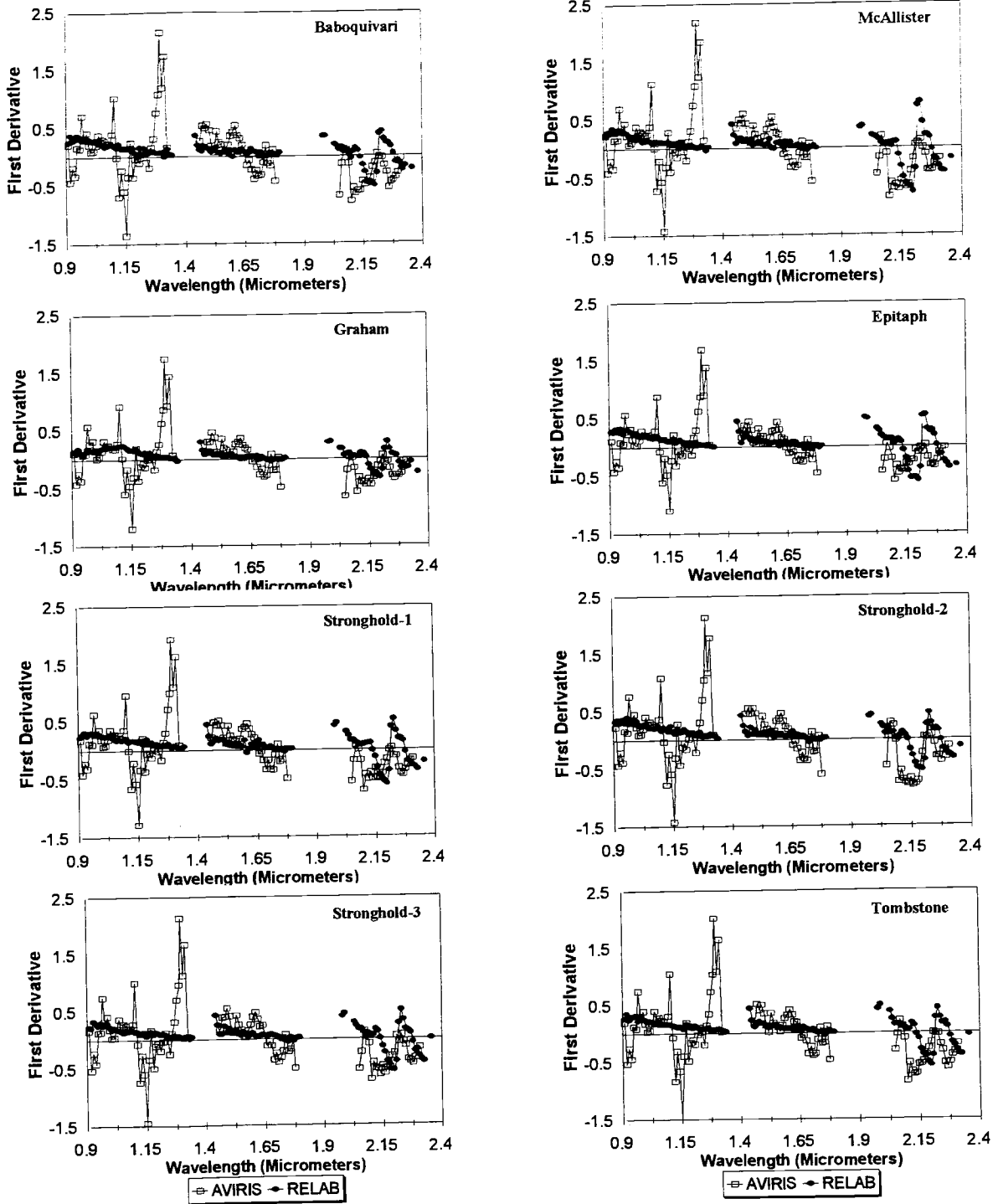


Figure 3-9. Comparison between the first derivative for AVIRIS and RELAB for the interval 0.9 to 2.4 micrometers

Grouping the Soils in Spectral Classes

Figures 3-10 through 3-13 show the dendograms resulting from clustering soil spectra measured under dry and wet conditions for field and sieved sample spectra. In these figures small distances mean a high degree of similarity, and the greater the distance, the greater the difference between samples. Soil spectral curves obtained under dry and wet conditions were clustered together for nadir (Figure 3-10), -30 degree view angle (Figure 3-11), and 30 degree view angle (Figure 3-12), to compare the effect of the view angle on the spectral classification of the eight soils. In these figures two main classes are well discriminated when considering field results for nadir and 30 degree view angles in both, forward and antisolar directions, and for sieved sample results. The euclidian distance that separates these two clusters is about 1.2 in all cases. These classes represent the difference in brightness that exists between most of the dry (bright) and wet (dark) soils. For nadir and -30 degree view angles these two clusters, are composed of the same group of soil samples. The first cluster contains all soil samples under dry condition, except Epitaph. On the other hand, the second group contains all soil samples under wet condition plus Epitaph under dry condition. For 30 degree viewing angle (forward scattering direction) (Figure 3-12) and for sieved sample spectra (Figure 3-13), however, the number of soil samples in the first cluster dropped from 7 to 6, while the second cluster contains, in addition to all the wet soil samples, Graham and Epitaph samples under dry condition.

Under dry condition one group of soils composed by Stronghold-1, 2, and 3, and Tombstone appeared in the same cluster (with slight differences in the way they are clustered) either for field (for any viewing angle) and sieved sample results. Both Stronghold and

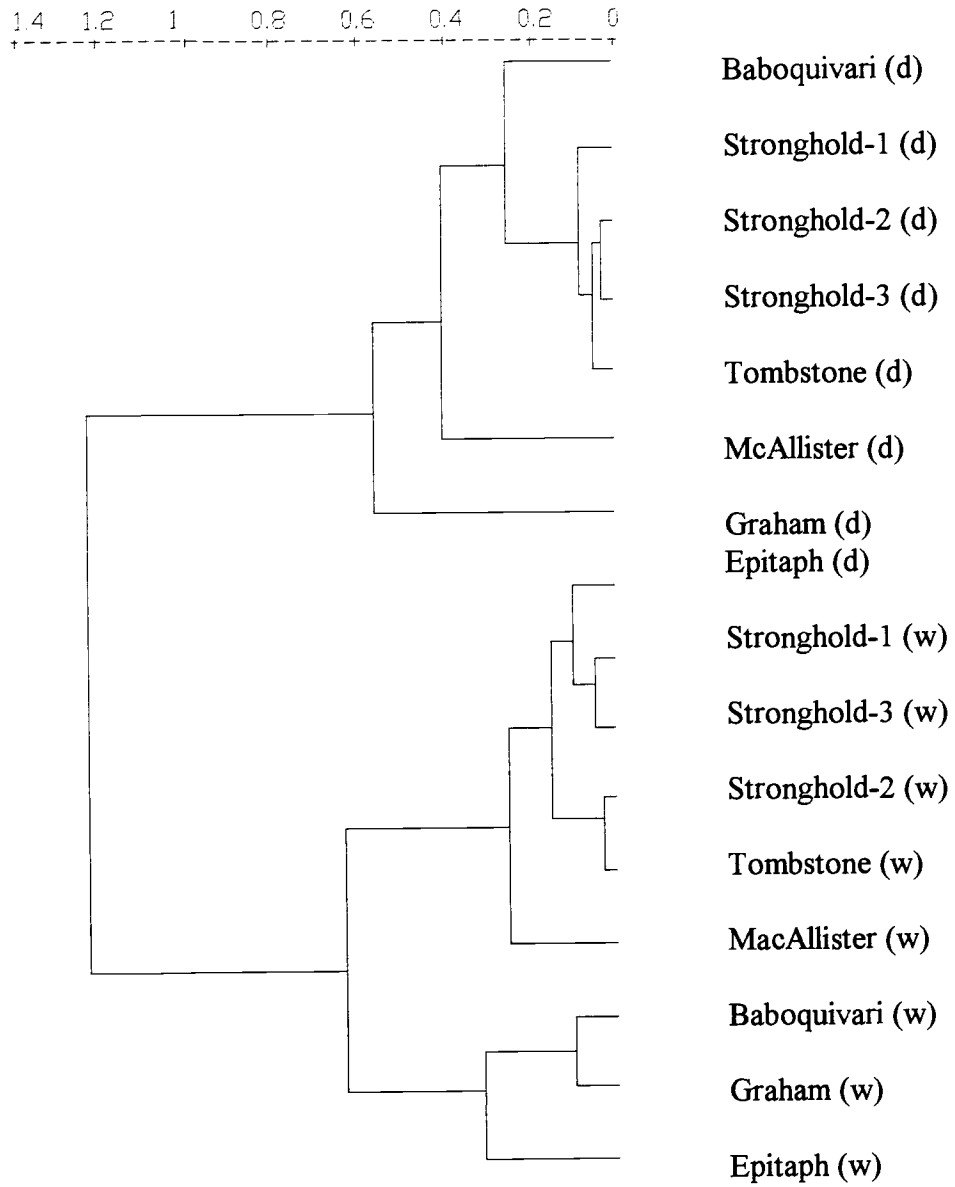


Figure 3-10. Dendrogram for field spectra taken at nadir view angle for soil under dry (d) and wet (w) conditions.

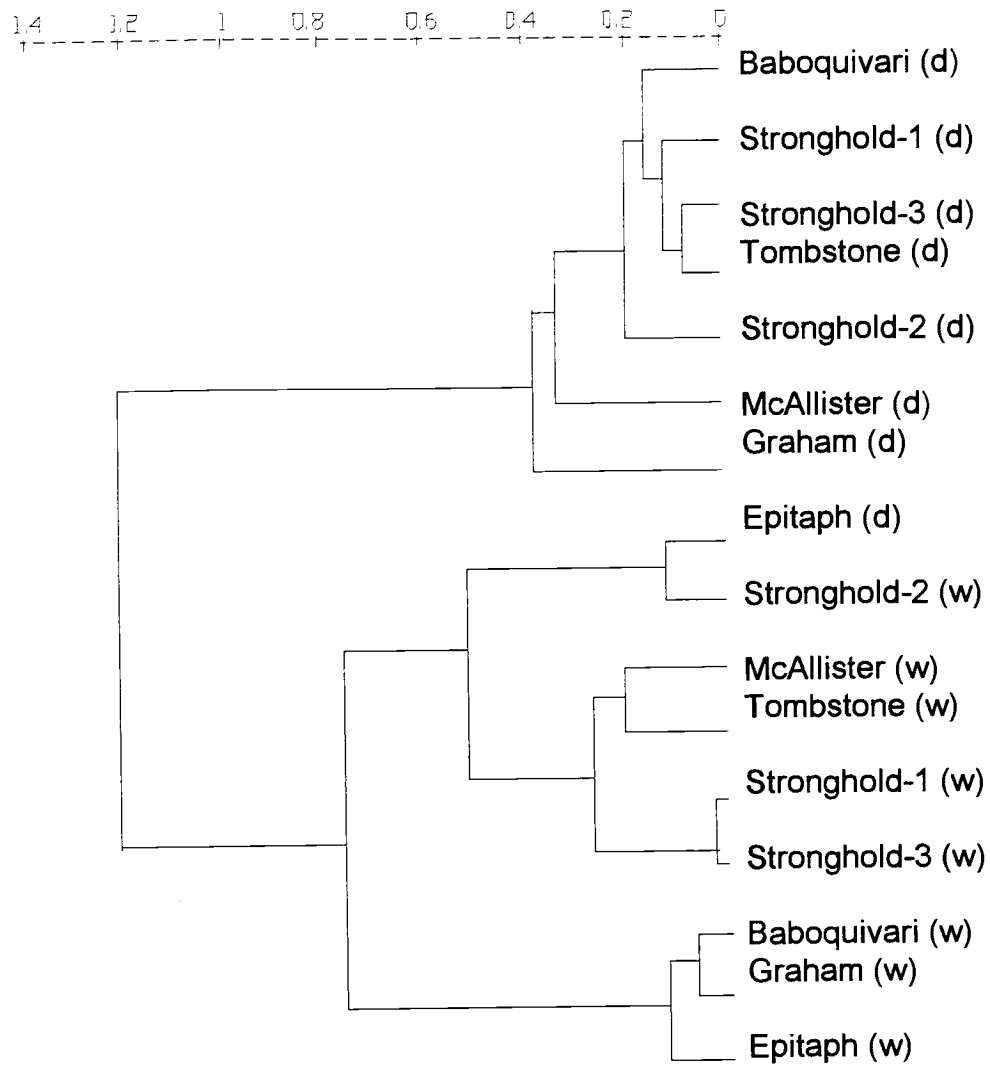


Figure 3-11. Dendrogram for field spectra taken at -30 degree view angle for soil under dry (d) and wet (w) conditions.

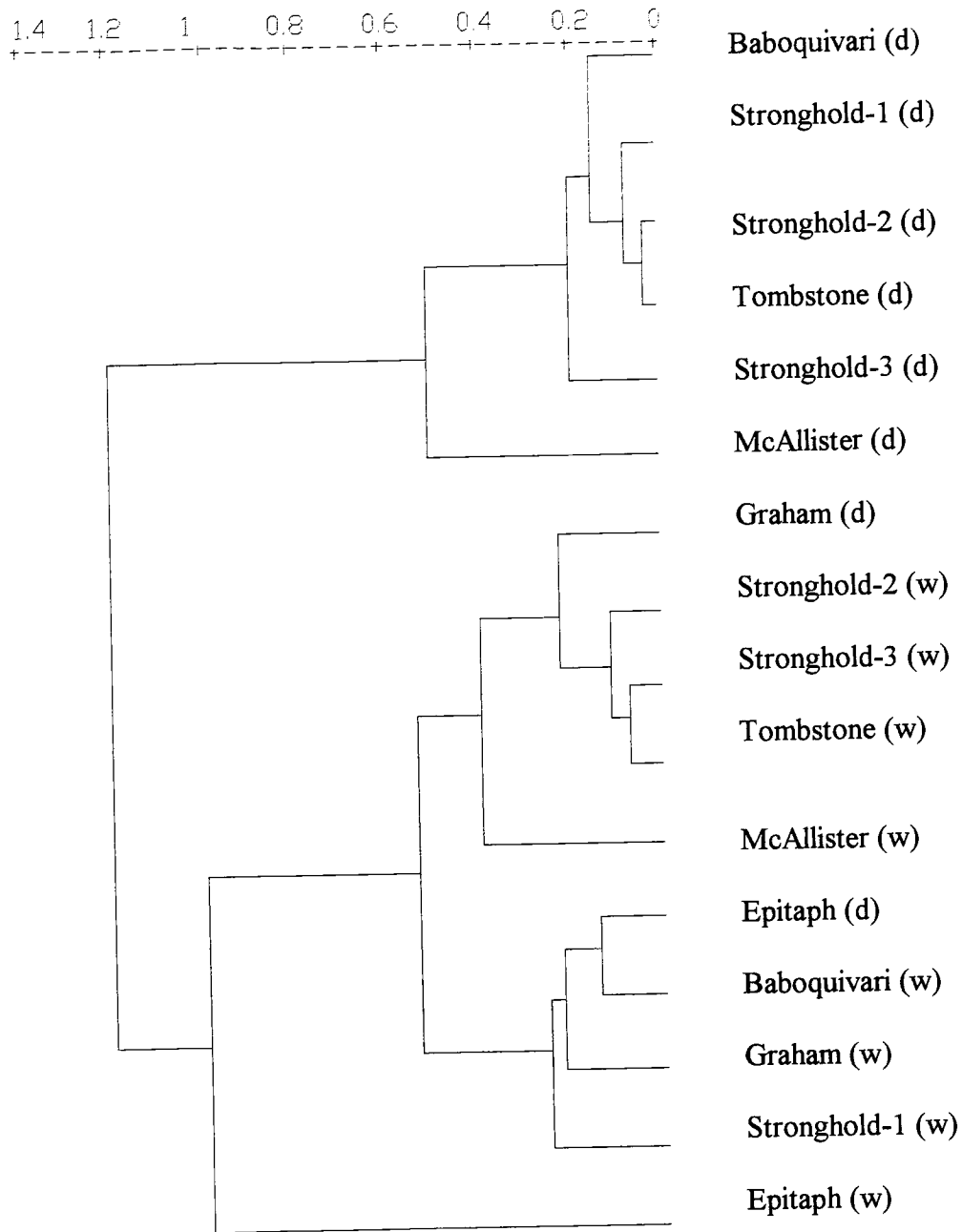


Figure 3-12 Dendrogram for field spectra taken at 30 degree view angle for soil under (d) and wet (w) conditions

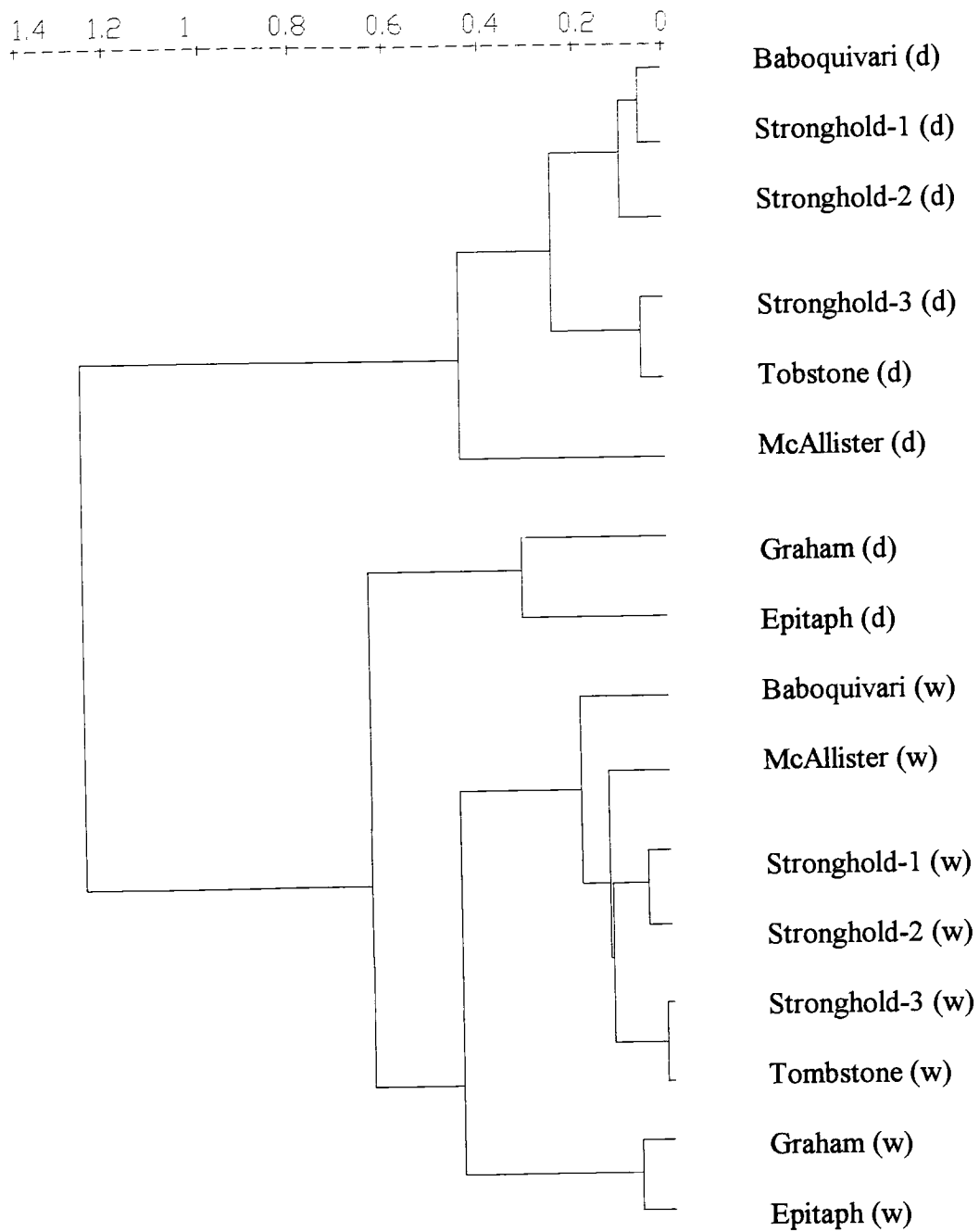


Figure 3-13. Dendrogram for sieved sample spectra taken under dry (d) and wet (w) conditions

Tombstone soil series differs only in the class textural of the control section when considering their classification at the family level. They also occupy the same landform (fan terrace) and are originated from the same parent material (mixed calcareous and fan alluvium). On the other hand, although Baboquivari and McAllister present the same classification at the family level (see Table 2-1), they are different in terms of age. Baboquivari is the youngest soil located in the fan terrace landform and as a result the effects of weathering on the development of this soil is much less than in McAllister soil series. Iron oxide was expected to have a much more important role on the characteristics of McAllister soil series than on the Baboquivari soil series. The redder color of McAllister, as compared to Baboquivari, can be attributed to these factors. Much harder to explain, however, is the similarities that appeared between McAllister and Graham under dry condition when they were clustered for -30 degree viewing angle (Figure 3-11).

The subgroups of classes presented in the group of dark soils (represented by wet soils and some dry soils) were much more variable than the subgroups of bright soils when comparing field results (nadir, -30 and 30 degree viewing angles) with sieved sample results. Thus, samples from Stronghold soil series and Tombstone soil series under wet conditions were clustered in a similar way when comparing field results for the nadir viewing angle and sieved sample results. These clusters are in agreement with the results presented when considering the same samples under dry conditions. However, when considering off-nadir viewing angles, the samples from these two soils were clustered differently from nadir field and sieved sample results. Thus, for a -30 degree viewing angle (antisolar direction), the four samples (3 from Stronghold and 1 from Tombstone soil series) were clustered in 3 different

groups (Figure 3-11). The first group was composed of Epitaph under dry condition and Stronghold-2 (wet) and presented higher degree of dissimilarity when compared to the other two groups. The second and the third groups were composed of wet samples of McAllister and Tombstone, and Stronghold-1 and Stronghold-3, respectively (Figure 3-11). For 30 degree viewing angle (forwardscatter direction), Stronghold-2, Stronghold-3, and Tombstone, all under wet condition, presented a high degree of similarities. By contrast Stronghold-1(wet) sample was left in a different cluster composed of Epitaph (dry), Baboquivari (wet), and Graham (wet). Notice also, that Graham under the dry condition presented close similarities to Stronghold-2 (wet), Stronghold-3 (wet) and Tombstone (wet). Changes in color parameters after wetting the soils under field conditions can justify these results.

Figures 3-10 and Figure 3-11 also show that another group of soils (under wet condition), composed of Baboquivari, Graham and Epitaph were clustered in the same way either for nadir and for the -30 degree viewing angle when considering the field results. However, for the 30 degree viewing angle (Figure 3-12), Epitaph soil series under wet condition is distinguished from any other group of soils by a higher degree of dissimilarity given by the distance that separates this soil series from the others. On the other hand, Graham and Baboquivari were clustered in the same group as Epitaph (dry condition) and Stronghold (Figure 3-12).

These results indicated that, to some extent, the information content from nadir and the -30 degree viewing angle for field results were comparable each other. On the other hand, the information content from the 30 degree viewing angle (forwardscatter direction) was

much less comparable with the results obtained for nadir and the -30 degree viewing angles. These results also show that the spectral classification of the soils depend on the viewing angle.

Sieved sample results for cluster analysis presented, along with the groups already discussed, two distinguished groups composed of Graham and Epitaph soils series under dry and wet conditions, respectively (Figure 3-13). These two soils have in common the fact that they have slope alluvium and residuum of basalt as their parent material, and the fact that in their clay fraction predominates montmorillonite. The picture presented in Figure 3-14 shows the soil samples used to obtain the sieved sample cluster. The first row in Figure 3-14 represents the brighter group of soils composed of 6 samples of dry soils, while the second and the third rows represent the darker soil samples composed of 8 samples under wet conditions and 2 under dry conditions. The space between the plates containing soils gives us an idea of how the soils are grouped in the dendrogram presented in Figure 3-13.

The RELAB data set was clustered first for each viewing angle separately (Figure 3-15a, b, and c) and then combined in the same cluster analysis for all three viewing angles (Figure 3-16). The soils were grouped in a similar way for the nadir viewing angle and for 35 degrees (forward scatter direction) (Figure 3-15a, and c). In both cases four clusters are visualized; the first one composed of Baboquivari, Tombstone and Stronghold-3 soils; the second one composed of McAllister and Stronghold-2; the third one composed of Stronghold-1 and Graham and the last one composed of Epitaph alone. As shown in Figure 3-15b, clustering the RELAB data for - 35 degrees (antillumination direction) produced somewhat different results compared to clustering the data for nadir and 35 degree viewing



Figure 3-14. Picture of the soil samples used to obtain the sieved sample spectral classes presented in Figure 3-13. The first row represents the bright soils while the second and the third rows represents the dark soil samples. The capital letter D means dry, and W means wet sample.

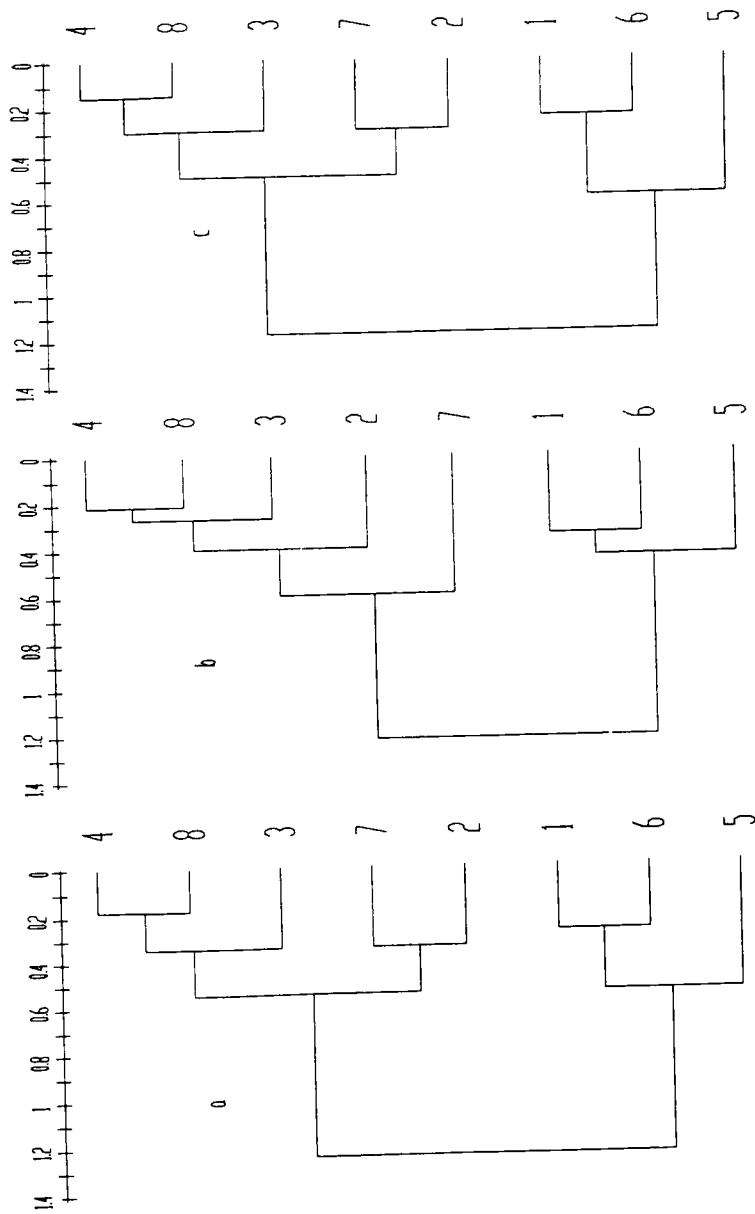


Figure 3-15 Dendrograms from clustering RELAB's data set for nadir (a), -35 (b), and 35 (c) degree viewing angles. The numbers represent: 1 = Stronghold-1, 2 = Stronghold-2, 3 = Stronghold-3, 4 = Baboquivari, 5 = Epitaph, 6 = Graham, 7 = McAllister, 8 = Tombstone.

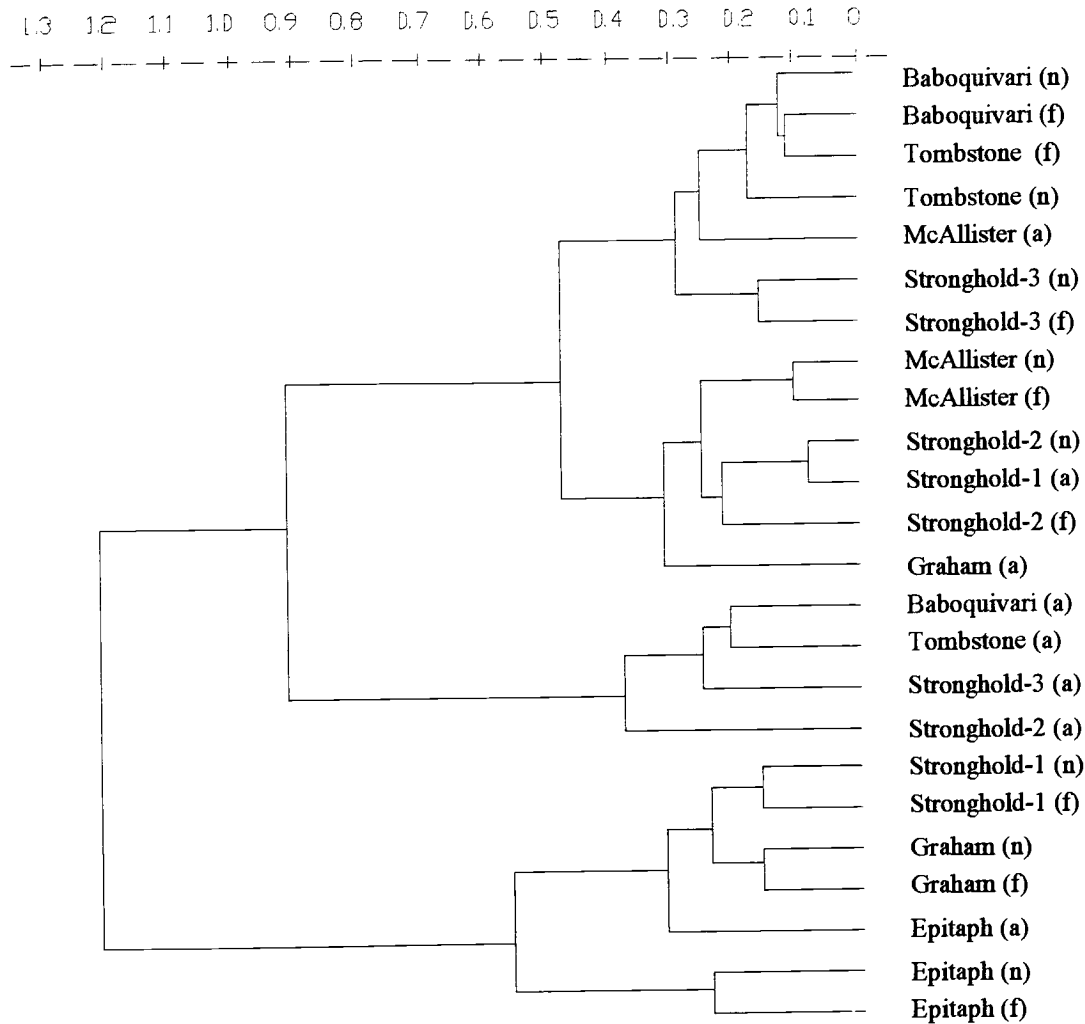


Figure 3-16. Dendrogram from clustering RELAB's soil spectral curves for nadir (n), -35 (a), and 35 (f) degree viewing angles.

angles. In the antilumination direction Stronghold-2, McAllister, and Epitaph all tended to be isolated and constituted an individual group.

Figure 3-16 shows how the soils are grouped when considering all three viewing angles together. Five soil groups are visualized in Figure 3-16. The first group composed of Baboquivari (n, and f; where n stands for nadir and f stands for forward scatter direction), Tombstone (n, and f), Stronghold-3 (n, and f), and McAllister (a, where a stands for antilumination direction). The second group is composed of McAllister (n, and f), Stronghold-2 (n, and f), Stronghold-1 (a), and Graham (a). For a given soil the spectral response in both, nadir viewing angle and 35 degree viewing angle (forward scatter direction) tend to fall in the same group. In some of the 5 groups, however, there are soils that present different characteristics from the other constituents of the group but, due to the particular spectral response in a given viewing angle, they could mistakenly be grouped together with different soils. For RELAB's data set we can point out two of these cases. In the first case the McAllister soil, which constitutes an individual group in the dendrogram for the -35 degree viewing angle and is clustered together with Stronghold-2 for 35 degree and nadir viewing angles (Figure 3-15a, b, and c), is grouped together with Baboquivari (n and f), Tombstone (n) and Stronghold-3 (n and f). Typically McAllister is redder in color than any other soil of the group and its deep absorption feature toward the blue is evidence of its higher iron oxide content compared to the other soils present in its group. The second misclassification refers to Epitaph. This Vertisol is grouped by itself for all the viewing angles (Figure 3-15a, b, and c) but when considering its spectral response in the backscatter direction, it falls in the same group as Graham (n and f) and Stronghold-1 (n and f) (Figure 3-16).

To allow a comparison between RELAB's results and field results under dry condition the RELAB's spectral bands were resampled to match the spectral interval and spectral range of the Spectron instrument (0.45 to 0.90 μm with 10 nm bandwidth). The dendograms for RELAB's resampled spectra for each viewing angle is show in Figure 3-17a, b, and c for nadir, 35 degrees (forward scatter direction) and - 35 degrees (backscatter direction), respectively. Figure 3-17d, e, and f also shows the dendograms for field spectra for nadir, 30 degrees (forward scatter direction), and - 30 degrees (backscatter direction), respectively. Comparison of the soil groups in different viewing angles shows the same tendency pointed out on spectral data being clustered in a similar way when considering nadir and 35 degrees for RELAB data (Figure 3-17a, and b) or 30 degrees for field data (Figure 3-17d, and e). However in the backscatter direction (- 35 degrees for RELAB data, and - 30 degrees for field data), soil spectra are clustered differently when compared to nadir and 35 degree view angles (Figure 3-17c and f). The differences in the way the soils are grouped for - 35 degrees in relation to nadir and 35 degrees are greater for RELAB's data than for field spectral data.

Comparison between the way the soils were grouped for RELAB's data with the way the soils were grouped for field data can also be made using Figure 3-17. For any viewing angle the soils were grouped differently in RELAB compared to field spectral data. For example, the two main clusters for nadir and 35 degree viewing angles (or 30 degree viewing angle for field data) have four soils in each of the two clusters for RELAB data (Baboquivari, Stronghold-3, Tombstone, and McAllister in the first cluster, and Stronghold-1, Graham, Stronghold-2, and Epitaph in the second cluster) while for field data, Epitaph soil was

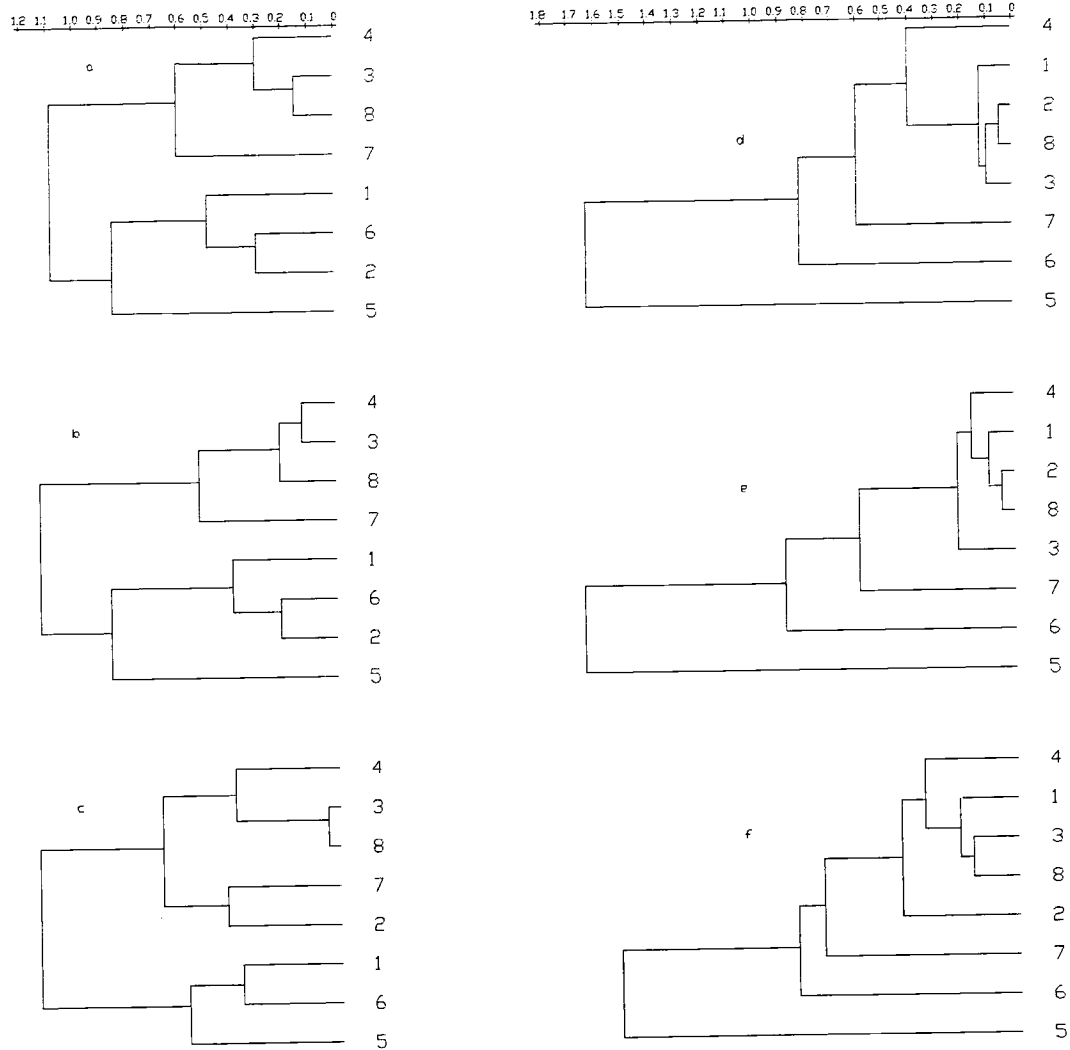


Figure 3-17. Dendrograms showing how the spectral curves were clustered after resample RELAB's data for nadir (a), 35 (b) and -35 (c) degree viewing angles and for field data for nadir (d), 35 (e) and -35 (f) degree viewing angles respectively. The correspondent numbers represents: 1 = Stronghold-1, 2 = Stronghold-2, 3 = Stronghold-3, 4 = Baboquivari, 5 = Epitaph, 6 = Graham, 7 = McAllister, and 8 = Tombstone.

separated from the other seven soils when considering the same two main clusters. For RELAB's data at - 35 degree view angle the two main clusters were now composed of Baboquivari, Stronghold-3, Tombstone, McAllister, and Stronghold-2 in the first cluster and Stronghold -1, Graham, and Epitaph in the second cluster while for field data the two main clusters were the same as for the other viewing angles.

Considering now clusters separated for less centroid distances, differences in the composition of each cluster can be seen when comparing RELAB data with field data. In field data, for example, for nadir and 30 degree view angles, Baboquivari, Stronghold-1, Stronghold-2, Stronghold-3 and Tombstone appeared in the same cluster, while for nadir and - 35 degrees in RELAB data, these soils appeared in different clusters. Still for nadir and 30 degree view angles for field spectral data, Graham constituted one group of soil by itself, while for RELAB data for the equivalent view angles, Graham soil is clustered together with Stronghold-2. Differences in clusters at low distance centroids are also shown by cluster analysis for RELAB's data and field data for view angle in the backscatter direction (Figure 3-17c and f). These results show that the spectral classification of soils depends on the way the data is obtained (field vs RELAB) and also emphasizes the importance of knowing the spectral behavior of soil surfaces to avoid misclassification due to the interaction of the sun-viewing angle geometry with these surfaces.

Spectral Dimensionality of the Data Set.

Table 3-5 presents the results of the eigenvalue analysis and some error parameters recommended by Malinowski (1991) to find the number of factors. The variance explained for the first factor accounted for almost the total variance. The real error for the first factor also represented only 1% reflectance. When there is no knowledge of the experimental error, Malinowski and Howery (1980) stated that the factor indicator function (IND) is more sensitive than other functions (such as imbedded error function - IE) in its ability to pick out the proper number of factors. Another advantage of the IND over other estimators of the factor space, such as the real error, is that it reaches a minimum value for the proper number of factors. Table 3-5 shows that the factor indicator function reaches a minimum when considering 4 factors, meaning that this should be the dimension of RELAB's data set.

A more detailed analysis of the error for determining the number of meaningful factors is done using a stepwise reconstruction of the original data matrix considering different numbers of factors as presented in Table 3-6. This table presents only the 10 largest errors found trying to reconstruct the original data set using from 1 to 5 factors. The exemplification of the reconstruction of the data matrix is shown in this section for the four key soil spectral curves obtained when considering that a four factor space can represent RELAB's data set. The key set of soils represents the typical soil vectors that best account for the complete variability between soil samples. The key soil spectral curves in order of importance were: Epitaph, Graham, McAllister, and Baboquivari. Notice that these soils are present in different clusters shown in Figure 3-15a. Thus, Epitaph soil alone constitutes one class; Graham is the key soil that represents the class formed by itself and Stronghold-1;

Table 3-5. Eigenvalue analysis for 340 bands (from RELAB data set) measured in 8 soil samples

Factor (n)	Eigenvalue (λ)	Variance (%)	Error Parameters		
			RE	IE	IND
1	282.96	99.87	0.01	0.00346	0.002
2	0.14962	0.00	0.006	0.00311	0.00173
3	0.05947	0.00	0.003	0.00207	0.00135
4	0.01406	0.00	0.0002	0.0014	0.00124
5	0.00354	0.00	0.0001	0.00105	0.00148
6	0.00147	0.00	0.00007	0.00061	0.00175
7	0.000222	0.00	0.00005	0.00053	0.00571
8	0.000111	-	-	-	-

Table 3-6. Influence of the number of factors on the ten largest error present in the reconstructed matrix. Soil numbers are: 1 = McAllister, 2 = Baboquivari, 3 = Graham, 4 = Stronghold-1, 5 = Epitaph

1 Factor					2 Factors					3 Factors				
Band	Soil	Measured	Absolute	Relative	Band	Soil	Measured	Absolute	Relative	Band	Soil	Measured	Absolute	Relative
μm	#	Value	Error	(%)	μm	#	Value	Error	(%)	μm	#	Value	Error	(%)
0.440	1	0.068	0.028	40.59	0.450	1	0.073	0.031	42.03	2.400	2	0.410	0.017	4.12
0.435	1	0.066	0.028	41.88	0.485	1	0.086	0.031	35.63	2.395	2	0.410	0.016	3.83
0.430	1	0.064	0.028	43.17	0.440	1	0.068	0.031	44.85	2.390	2	0.411	0.016	3.77
0.450	1	0.073	0.028	37.77	0.435	1	0.066	0.031	46.28	2.385	2	0.412	0.015	3.67
0.425	1	0.062	0.028	44.50	0.460	1	0.077	0.031	39.61	2.380	2	0.413	0.015	3.58
0.460	1	0.077	0.027	35.58	0.480	1	0.084	0.031	36.35	2.370	2	0.415	0.014	3.42
0.445	1	0.071	0.027	38.81	0.430	1	0.064	0.030	47.72	2.365	2	0.416	0.014	3.36
0.420	1	0.060	0.027	45.33	0.445	1	0.071	0.030	43.06	2.375	2	0.414	0.014	3.38
0.485	1	0.086	0.027	31.54	0.490	1	0.088	0.030	34.66	2.350	2	0.418	0.014	3.32
0.480	1	0.084	0.027	32.42	0.425	1	0.062	0.030	49.19	2.355	2	0.417	0.014	3.26

Table 3-6. Influence of the number of factors on the ten largest error present in the reconstructed matrix. Soil numbers are: 1 = McAllister, 2 = Baboquivari, 3 = Graham, 4 = Stronghold-1, 5 = Epitaph (Cont.)

4 Factors					5 Factors				
Band	Soil	Measured	Absolute	Relative	Band	Soil	Measured	Absolute	Relative
μm	#	Value	Error	(%)	μm	#	Value	Error	(%)
1.000	3	0.269	0.006	2.34	2.400	4	0.302	0.003	1.13
0.990	3	0.267	0.006	2.32	2.345	4	0.315	0.003	1.02
0.985	3	0.266	0.006	2.26	2.350	4	0.314	0.003	1.02
1.020	3	0.272	0.006	2.21	2.340	5	0.275	0.003	1.13
0.995	3	0.268	0.006	2.24	2.345	5	0.274	0.003	1.13
0.980	3	0.265	0.006	2.22	2.335	5	0.277	0.003	1.08
1.010	3	0.271	0.006	2.18	2.340	4	0.317	0.003	0.91
1.015	3	0.271	0.006	2.15	1.180	4	0.309	0.003	0.91
1.005	3	0.270	0.006	2.16	1.355	4	0.313	0.003	0.90
0.960	3	0.262	0.006	2.15	2.335	4	0.319	0.003	0.88

McAllisters is the key soil that represents the class that also has Stronghold-2 soil, and Baboquivari is the key soil that represents the class formed by itself, Tombstone and Stronghold-3 (Figure 3-15a).

The one factor model gave us 2.40 μm as the key band needed to separate the 8 soil samples. The separation of the eight soil samples on the base of one factor gave us 8 curves that differ only in the magnitude of response. In 2.40 μm band the difference in magnitude of response was higher than in any other part of the RELAB's measured spectrum. Figure 3-18 shows the reconstruction of the four key soil curves or four basic soil curves and the error generated when one factor was used. Most of the error is in the interval between 0.4 and 0.8 μm and above 2.1 μm regions of the spectrum and that Epitaph, Graham and McAllister were key soils most affected by the spectral reconstruction using only one factor model. The one factor model overestimated the BRDF values for McAllister in the interval of 0.4 to 0.8 μm and also above 2.1 μm while underestimating the BRDF in the interval between 0.6 and 1.0 μm .

For Epitaph soil the one factor model overestimated the BRDF in the interval between 0.4 and 1.0 μm , while for the rest of the measured spectrum, the error was maintained close to zero. For Graham, however, the one factor model underestimated the BRDF in the interval between 0.4 and 0.8 μm . The error for the one factor model is concentrated in the interval of 0.42 - 0.45 μm , with 7 out of 10 values in this region of the spectrum (Table 3-6). The departures from the original reflectance values for one factor reconstruction in the blue region varied from 31% to 45% (Table 3-6). Thus, the one factor model can reproduce the original data matrix at the expense losing information given by the curve shape, mostly in the blue region of the spectrum.

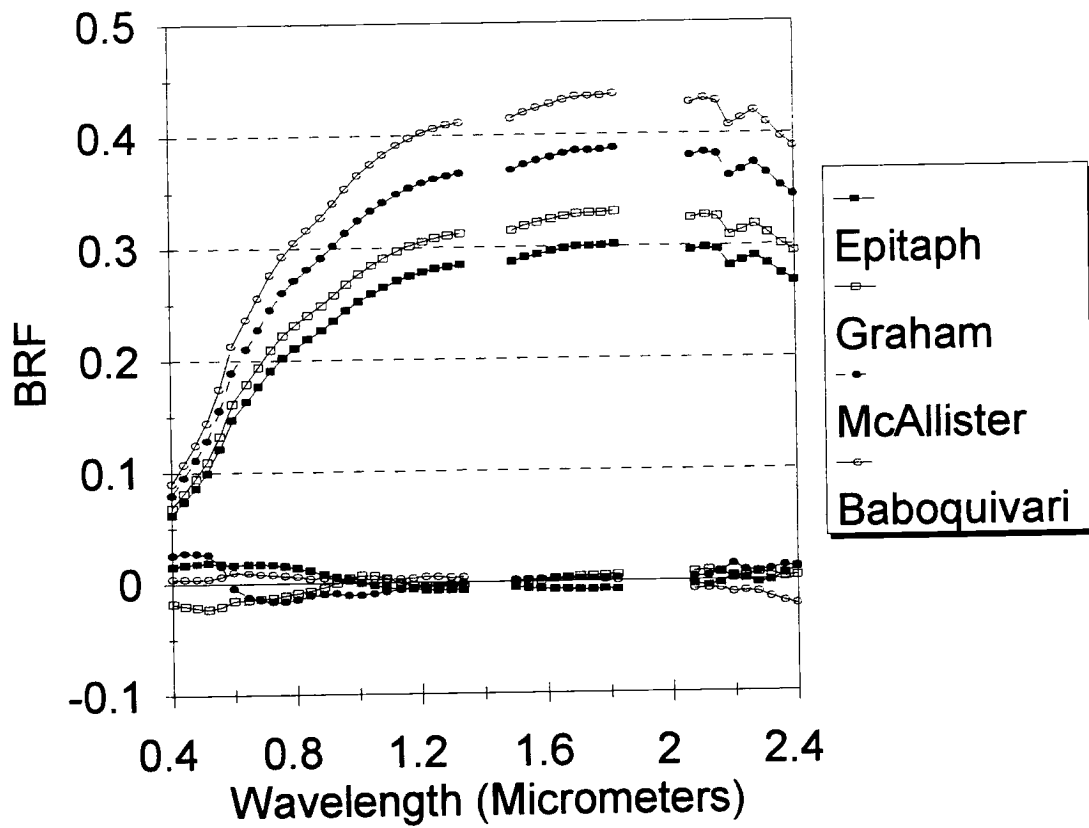


Figure 3-18. Spectral recomposition and error using one factor for the four soil basic curves

Figure 3-19 shows the spectral reconstruction of the four key or basic soil curves for a two factor model. The bands located at 0.405 μm and 2.110 μm are the key bands for a 2 factor model. As in the one factor model, the recomposition of the spectral curves in the two factor model presents unacceptable error for reflectance concentrated in the half end of the blue region (0.450 - 0.480 μm). The ten largest errors (which varied between 35 and 47%) in a two factor model shows that a band in the blue region is still needed (Table 3-6).

Although there is some error beyond 2.100 μm for Baboquivari and McAllister soil series, McAllister soil was by far the most affected soil by the spectral curve reconstruction using the two factor model. The other basic soil curves (Epitaph and Graham) presented little deviation from the original spectral curves when considering reconstruction of their spectral curves using two factors (Figure 3-19). As shown in Figure 3-19, the two factor model improves the curve shape by adding the information contained in the region between 0.420 and 0.450 μm of the spectrum. Even though the two factor model improves the reconstruction model of the original spectral curves, iron affected soils, such as the McAllister soil series, were still among the most sacrificed in terms of information extraction when considering one or two factor models.

With the three factor model most of the information content in the visible and NIR region of the spectrum was recovered for all the four key soil curves (Figure 3-20). Some errors still remain in the middle infrared region, and Baboquivari is the most affected soil. Thus, for Baboquivari soil the three factor model underestimated the BRFR in the interval between 2.200 and 2.400 μm . The ten largest errors drop to the range of 3% to 4% of the measured reflectance and they are concentrated in the interval 2.350 - 2.400 μm (Table 3-6).

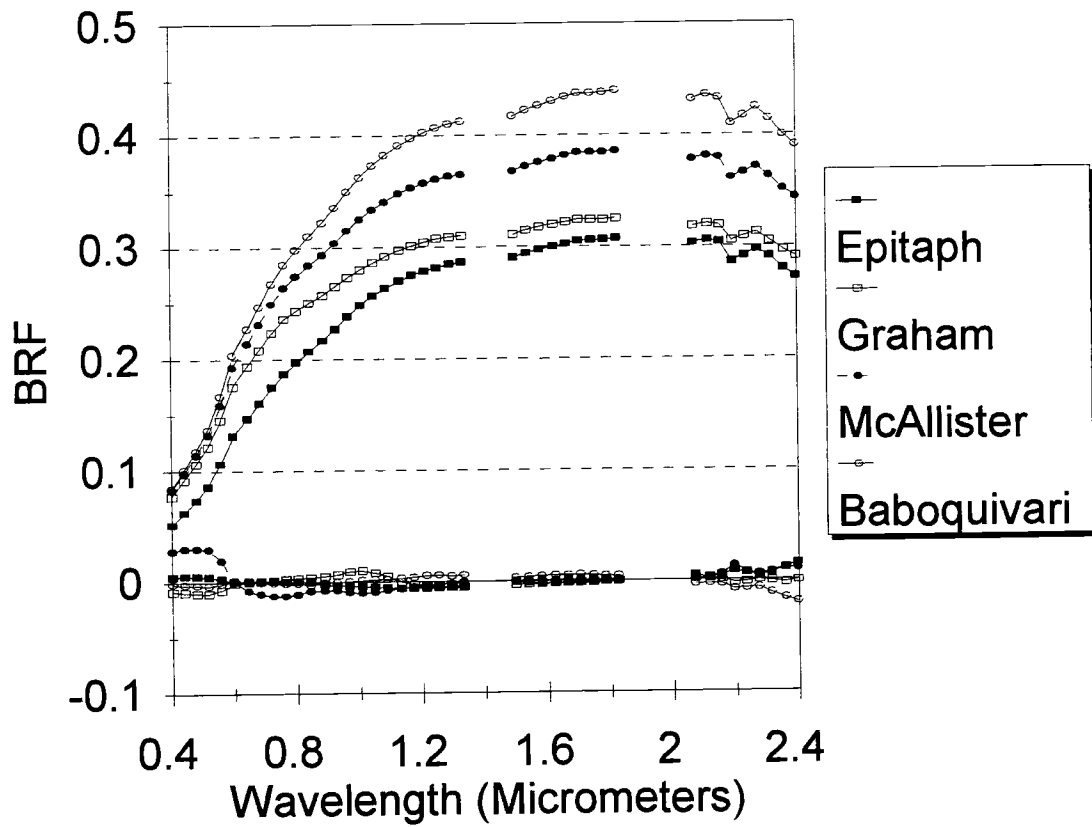


Figure 3-19. Spectral recomposition and error using two factors for the four soil basic curves

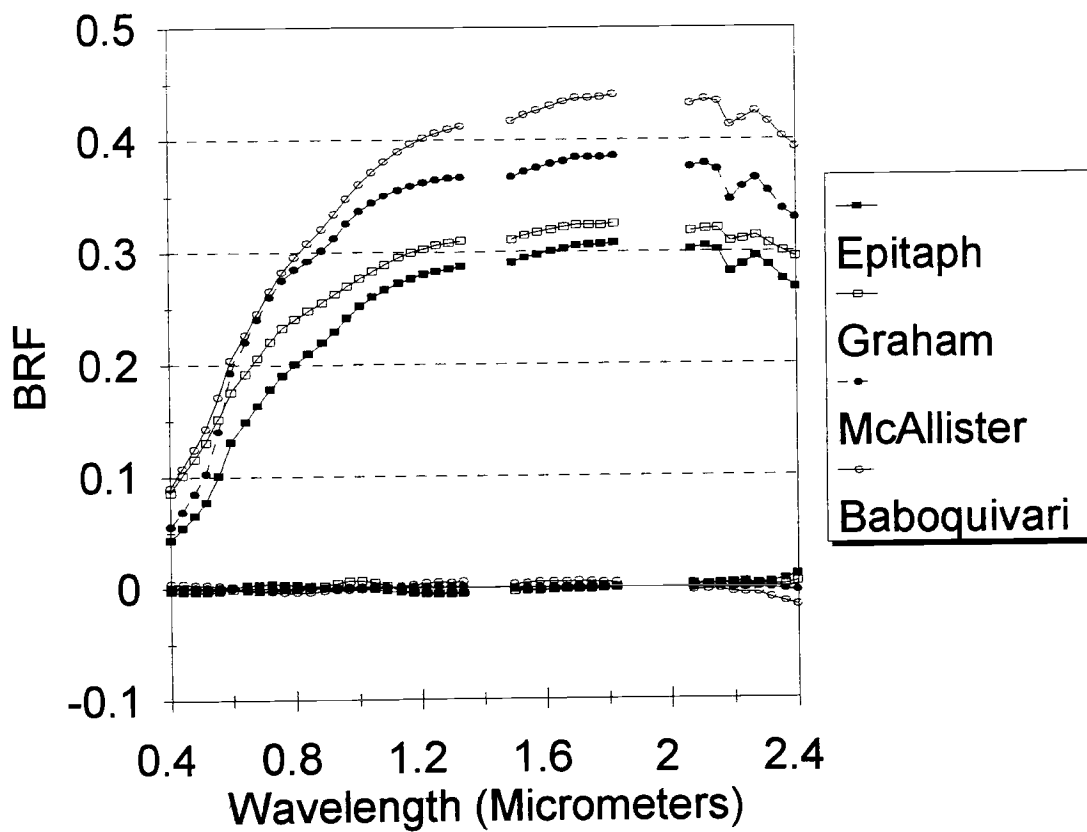


Figure 3-20. Spectral recomposition and error using three factors for the four soil basic curves

The key bands for a three factor models are located in 0.400, 2.320 and 0.640 μm .

Figure 3-21 shows the spectral recomposition curves for the four key soils using a four factor model. In a four factor model, the shape of the spectral curves are well modeled and they approximate to the original spectral curves. The errors concentrate in the NIR, but they drop to an acceptable amount of about 2% of the RELAB's measured reflectance (Table 3-6). The option for a four factor model also agrees with the factor indicator function which reaches a minimum at that number (Table 3-5). The key bands obtained in a four factor model are in order of importance: 0.410, 1.310, 0.650, and 2.400 μm . The key bands located at 0.410 μm and 0.650 μm agree with the results obtained by Huete and Escadafal (1991), which found, among others, that the first three key bands in order of importance were 0.410, 0.900 and 0.610 μm , respectively. Condit (1972) also found that only five bands were needed to represent 35 bands from 0.300 to 1.000 μm . These bands were in order of importance: 0.400, 0.920, 0.640, 0.540, and 0.740 μm . These authors, however, did not go beyond the NIR in their studies of the dimensionality of their data set.

Four groups of broad spectral bands resulted after using a combination of cluster analysis and factor analysis for four factors (Table 3-7). As show in Table 3-7 each of the key bands is the most representative band present in a cluster given by the spectral range. Figure 3-22a shows how the soils are grouped considering RELAB's data for nadir viewing angle using 340 bands. To compare the spectral group of soils obtained from the original RELAB's data set with the results after applying data reduction techniques, Figure 3-22b shows the spectral classes using the average response for each spectral range given in Table 3-7 while Figure 3-22c shows the soil spectral groups after applying factor analysis, which reduced the

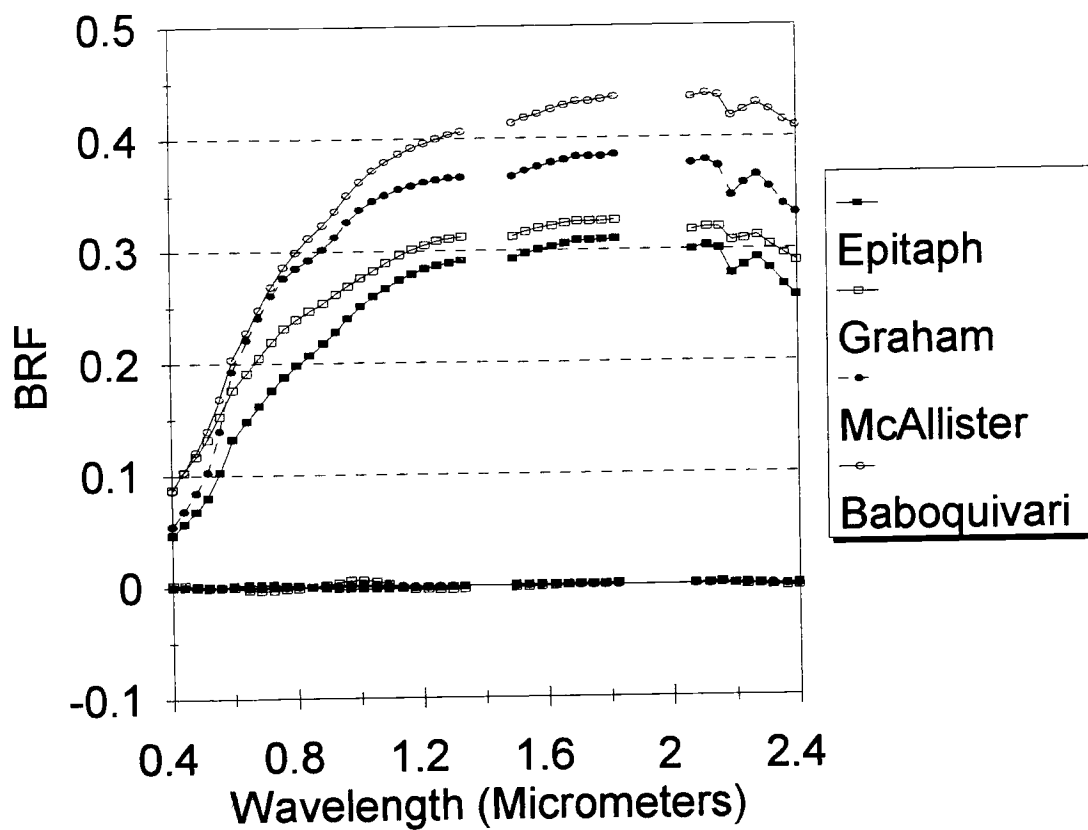


Figure 3-21. Spectral recomposition and error using four factors for the four soil basic curves

Table 3-7. Results of clustering 340 spectral bands using the option for 4 factors. Data from RELAB's soil spectra for nadir view angle.

Cluster #	Spectral range (μm)	Key band (μm)
1	1.355 - 2.400	2.400
2	0.400 - 0.570	0.410
3	0.575 - 0.870	0.650
4	0.875 - 1.350	1.310

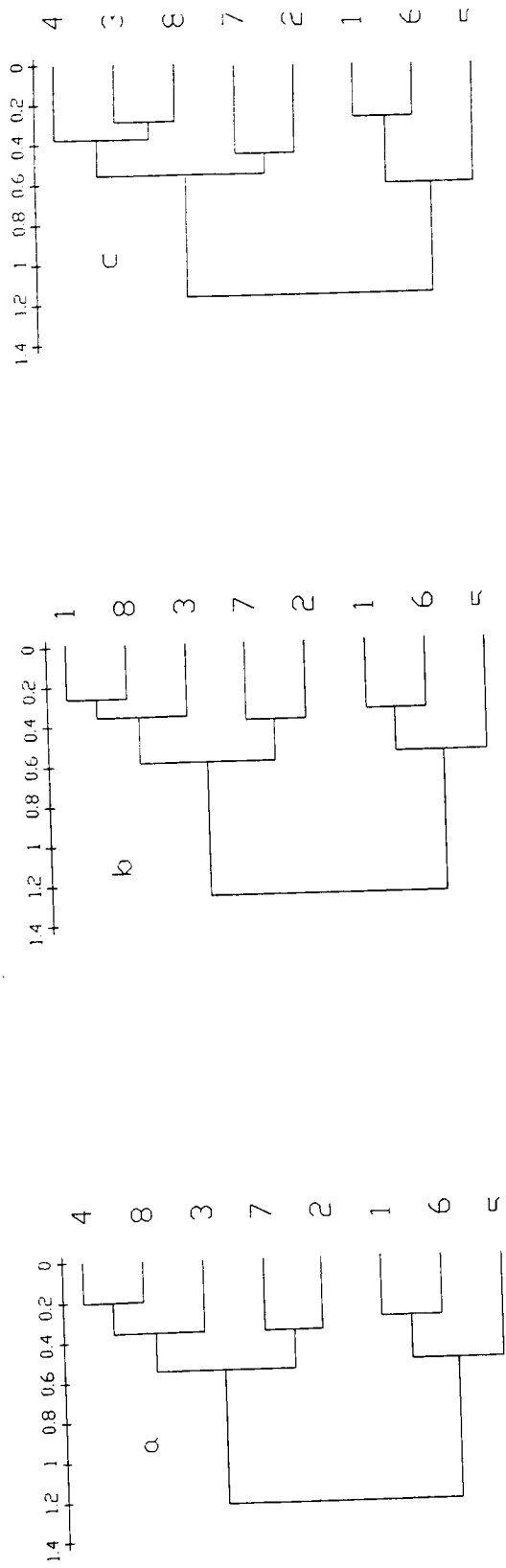


Figure 3-22 Dendrograms resulting from clustering RELAB's data for 340 bands (a), average from each one of the spectral range shown in Table 3-7 (b), and using the four key bands given by the four factor model (c). The numbers represent:

- 1 = Stronghold-1, 2 = Stronghold-2, 3 = Stronghold-3, 4 = Baboquivari, 5 = Epitaph, 6 = Graham, 7 = McAllister, 8 = Tombstone.

original data set to four bands.

Clustering the eight soil spectral curves for the nadir view angle from RELAB, using the average spectral response for each of the four spectral range obtained after clustering the bands, produced the dendrogram presented in Figure 3-22b.

Although the cluster results did not show differences, generally, the use of broad bands (as given by the spectral range in Table 3-7) means an increased in signal strength with a resulting improvement in the signal to noise ratio (Price, 1975). The use of broad bands, however, can also result in more in interferences (cross talk) from variables which are strongest in other parts of the spectrum (Price, 1975). Thus, Price (1975) showed that interference due to absorption lines of water vapor appeared in almost all of the spectral bands of the Iris instrument (wave numbers 400 to 1600 cm^{-1}). As shown in Figure 3-22, the soils were grouped in a similar way either using the average spectral response from the four broad bands (Figure 3-22b), using the original RELAB's data set (Figure 3-22a) or using the four key set of bands given by factor analysis (Figure 3-22c).

Figure 3-23 presents the spectral curves of the four key soils using the four key bands (0.410, 1.310, 0.650 and 2.400 μm). Clearly, the four key soil curves can be discriminated by using these four bands instead of the 340 RELAB's bands.

Conclusions

When compared to atmospherically corrected AVIRIS data, soil spectral curves derived from apparent reflectance tended to overestimate reflectance values in short wavelengths (blue) and underestimated reflectance in the NIR and MIR and these effects were

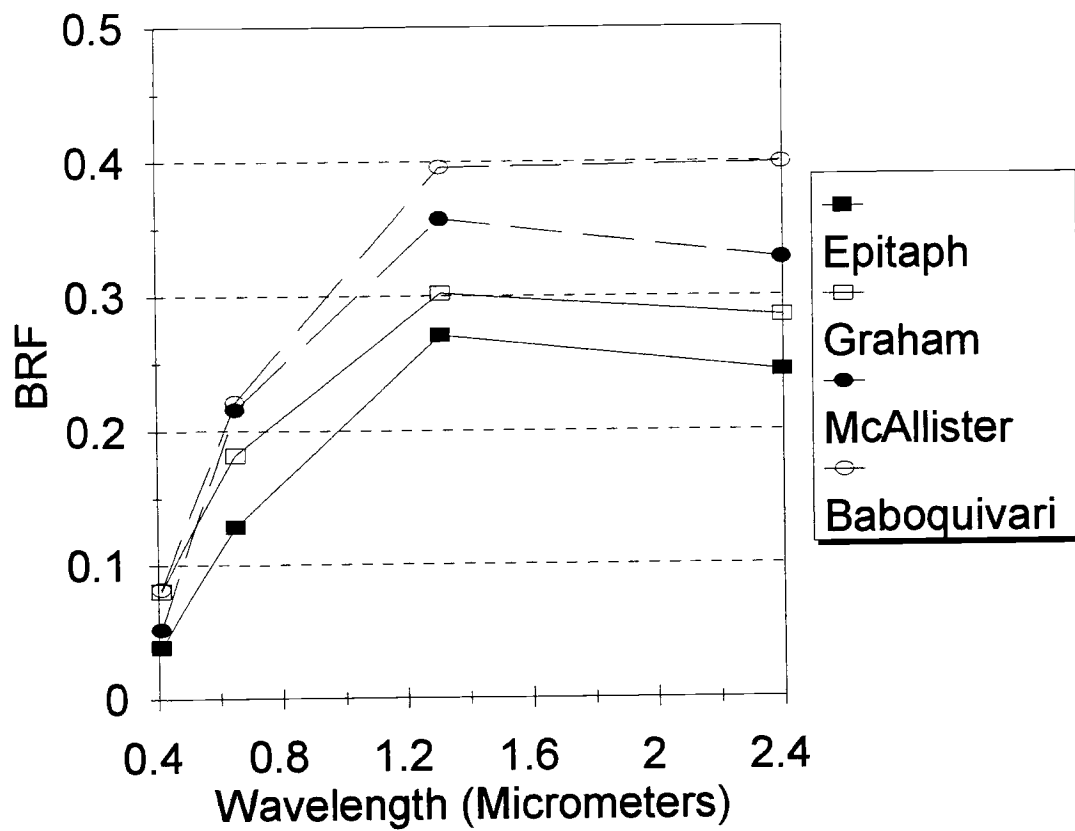


Figure 3-23. Spectral curves considering the four key bands for the four basic soil curves

more pronounced in dark (Epitaph) than in bright (Tombstone) soils.

RELAB, and the spectra from sieved samples presented higher reflectance values than field spectra but their spectra were featureless compared to field spectra.

The first derivative spectra for well developed soils, such as McAllister, Stronghold, and Tombstone, presented a pronounced peak in the region of 0.55 to 0.60 μm due to the higher content in secondary Fe oxides (hematite) compared to the other soils. First derivatives were highly sensitive to the spectral contribution of the small amount of green vegetation present in field spectra. The first derivative also revealed loss of information when moving from large scale data set (RELAB, sieved sample, and field spectra) to small scale data set (AVIRIS).

Cluster analysis showed that the spectral classification of soils depended on the wet conditions (dry versus wet), viewing angle, and where the spectra comes from (RELAB, sieved sample or field). Soil brightness was the main characteristic in separating the group of soils. Thus, for field spectra, bright soils such as Baboquivari, Stronghold-1, Stronghold-2, Stronghold-3, Tombstone, and McAllister under dry conditions appeared in one great group while these same soils under wet conditions appeared in another great group. Spectral subgroups of soils, however, varied according to the viewing angle. For a given soil, the spectra measured in nadir or 30 degrees in the forward scatter directions tended to be grouped in the same class, while the spectrum in 30 degrees in the backscattering direction was grouped in a different class. The source of the data also influenced the classification of soil spectra. Thus, different soil spectral classifications were obtained when considering soil spectra measured under field condition and under RELAB conditions.

The study of the dimensionality of the data set using factor analysis showed that the key soil spectral curves were in order of importance: Epitaph, Graham, McAllister, and Baboquivari. Factor analysis showed that RELAB's original spectra can be reconstructed for these four key soils by using four factors. The results also showed that the key bands in order of importance were: 0.410, 1.310, 0.650, and 2.400 μm and that these key bands were the most representative vectors of the following band intervals: 0.400 - 0.570 μm , 0.875 - 1.350 μm , 0.575 - 0.870 μm , and 1.355 - 2.400 μm , respectively. The soils were grouped in the same way whether using the 340 original RELAB bands, the average spectra obtained for each of the intervals given before, or the key bands.

CHAPTER 4

SPECTRAL MIXTURE ANALYSIS USING AVIRIS DATA

Introduction

Due to its capacity for covering large areas in a single image (also called synoptic view) repeatedly in short time, remote sensing presents an ideal tool for mapping soils classes and monitoring soil processes.

Satellite imaging has been used since the early seventy's for soil mapping. Since then, spectral maps have proven to be useful in evaluating soil properties, such as color (Post et al. 1994; Post, 1984), delineating boundaries between soils, and in assessing the homogeneity of soil map units (Weismiller et al., 1979). For some authors' opinions, however, the successful delineation of soil mapping units based on spectral characteristics of surface soil requires homogeneity of the soil units and dissimilarity among them (Cihlar and Protz, 1973). These authors also reported that spectral responses alone are not sufficient to accurately map the soils found in their study area, but spectral differences provide additional information on soil distribution. Indeed, as both surface and subsurface properties are used for differentiating soil categories, such as soil series, the use of aircraft and spacecraft images to identify soils has been questioned (Kristof and Zachary, 1971). Agbu et al. (1990), however, state that no soil map perfectly partitions soil variability, and hence soil maps are an imperfect standard for comparison with spectral maps.

There are two basic objectives when surveying soils. The first is to minimize the variations in significant soil properties within a given soil unit and, at the same time, maximize the variations among soil units. The second is to effectively characterize the mapping units in terms of significant soil properties. Agbu et al. (1990) state that it is inappropriate to use a field soil map as the only standard by which satellite-derived maps are evaluated and suggest evaluation of both the field soil maps and the imagery-derived maps independently, according to the degree to which they contribute to those objectives.

Although most of the applications of spectral mixture analysis have considered the soil component, in almost all cases the emphasis (as seen in the next section) in the discussion have been on the vegetation endmember with few dealings with the use of the soil fractions in actual soil surveys. The general objective of this chapter is to derive the soil spectral map of the AVIRIS scene of the Walnut Gulch Experimental Watershed using mixture analysis. The specific objectives are to: (a) evaluate the dimensionality of AVIRIS data (i.e., how many endmembers); (b) find the meaning of the dimensions (i.e., what feature in the ground each endmember represents); (c) determine the spatial abundances of the endmembers throughout the AVIRIS scene of the Walnut Gulch Experimental Watershed.

Background

Depending upon the field of view of the instrument and the spatial complexity of the ground features, the processed signal produced by a remote sensor often represents the integrated radiance of at least two and, frequently, more than two components present in the FOV of the sensor. Spectral target mixtures may contain diverse and spatially varying

components such as soil, green vegetation, rocks, and litter. Mixture analysis (also known as factor analysis, principal component analysis and correspondence analysis) is a general mathematical inversion technique useful in the interpretation of complex multivariate response problems in the field of chemistry and optics (Huete, 1986).

As applied to remote sensing, one purpose of mixture models is to decompose the measured spectra from experimental data or pixels into the spectra of their reflecting components. It also identifies the unique components present in a spectral mixture and assesses their relative contributions toward measured responses. SMA is a special model of image classification that allows classification of targets at the subpixel level. Subpixel targets can only be detected, however, under certain conditions of spectral contrast between targets and sensor characteristics such as spectral resolution (spectral range, and sampling interval) and instrumental noise. The spectrum of a subpixel target mixed with the spectrum (or multiple spectra) of the background results in a combined spectral signal. For an isolated pixel out of context, it may not be possible to decompose the combined spectra into their unique spectra. However, in the context of a multispectral image, where in most of the cases the spatial variability can be represented by a limited number of materials (between 2 and 5), the target spectrum commonly can be estimated using spectral mixture analysis. Thus, spectral mixture analysis can be used to detect and in some instances identify targets at the subpixel scale.

Techniques for "unmixing" pixels were developed in the early 1970's for use in Landsat MSS data. At that time, two statistical methods for estimating the proportion of components in a mixed pixel were established: maximum likelihood classification (Horwitz

et al., 1971) and linear regression (Richardson et al., 1975). The linear regression method was first applied for extracting plant, soil, and shadow reflectance components of cropped fields from Landsat MSS data. Richardson's model was used to study the relationship between fractional plant, shadow cover and leaf area index (LAI) for 23 planted fields to Landsat composite reflectance (R_c). The model produced regression lines with multiple correlation coefficients (in each band) statistically significant at the 0.01 probability level. These regression models could then be used to determine the component reflectance of the plant, soil, and shadowed areas. Horwitz et al. (1971) developed a complex maximum likelihood algorithm which is based upon the weighted combinations of component class mean vectors and covariance matrices. This method was particularly important to separate the proportion of pixel components that have highly differentiated spectral behavior.

Work and Gilmer (1976) have used the maximum likelihood approach to help inventory prairie ponds and lakes with Landsat MSS data. Using this technique, they were able to recognize a great number of small ponds not previously identified in images from dark prairie soils located in eastern North Dakota. Marsh et al. (1980) used an approximate maximum likelihood technique for resolving the percentage of component terrains within a pixel. In their work Marsh et al. (1980) tested five cases and in every case their methodology proved to be superior to single band weighted average and linear regression techniques developed by Richardson et al. (1975). Marsh et al. (1980) found that their technique could estimate the total area occupied by component terrains (endmembers) to within ± 6 percent of the true area covered and suggested that this accuracy is good enough for geologic applications of Landsat data. Forshi (1994) reviewed several methods of handling mixed

pixels and stated that statistical methods for estimating the proportions of components are most successful when the constituent classes are well separated.

In recent years, several modifications to the linear mixture model have been proposed with that suggested by Smith et al. (1987), which integrated laboratory spectra to correct for atmospheric effects, being one of the most utilized for different kinds of applications.

Mixture analysis has been applied to compute the abundance of soil or mineral components as well as green vegetation in a surface cover (Huete et al., 1985; Huete, 1986; Smith et al., 1990a; Roberts, 1991). Mixture analysis was used by Hlavka and Spanner (1995) for detecting, quantifying, and mapping three different stages of forest disturbance in Oregon: newly disturbed or clearcut areas (most of which is represented by bare soil surfaces), areas with substantial regrowth (where successional vegetation dominates), and areas where the reestablishment of coniferous canopy cover is greater than 75%. These authors found promising results in mapping forest disturbance using SMA with AVHRR data set.

Mixture analysis has also been applied to estimate vegetation biophysical parameters, such as leaf area index (LAI), plant biomass, net primary productivity (NPP), and the fractions of absorbed photosynthetically active radiation (fAPAR) (Dereck et al., 1996; Leeuwen et al., 1997). Dereck et al. (1996) found that scene fractions from spectral mixture analysis were superior to NDVI in terms of their relationship to LAI, biomass, and NPP. The overall r^2 values ranged from 0.70 to 0.80 for SMA, while NDVI results ranged from 0.4 to 0.47. Goodin and Henebry (1966) suggested that mixture analysis can be applied to monitor changes (due to natural and anthropogenic disturbances) in plant species composition including shifts in abundances of c3 vs. c4 lifeforms.

Due to its ubiquitous presence in almost every scene, soil has been present in almost all applications of SMA. In these studies, however, most of the interest is given to the fractions of the vegetation endmembers and their relationship to plant biophysical parameter as seen before. An example is given by Smith et al. (1994). In their research, soil spectral variability was studied by using SMA (and the results were compared to vegetation indices, such as NDVI) as a way to overcome the problem of the background effect on vegetation detection and quantification of abundance. One of the few examples of application of mixture analysis directly to soil was given by Huete and Scadafal (1991). These authors used SMA for soil biophysical information extraction in the region of 0.40 to 0.90 μm . They found that the variability of 46 soils from different types of environments could be explained by four independent basis curves, which, in linear combination, were able to reconstitute the experimental data set. With these four independent basis curves Huete and Scadafal (1991) isolated weak and broad absorption features from the dominant brightness component of each soil spectra.

Compared to other traditional methods of image classification, mixture analysis has been shown to present advantages mainly when the within pixel surface cover variability is high. Fernandes et al. (1996) compared the accuracy of linear least squares mixture analysis with maximum likelihood supervised classification for three different cases: pure pixels, boundary mixing and complete mixing. When complete mixing occurs in the scene, they found that the linear mixture model was significantly more accurate than per-pixel maximum likelihood classification. Maximum likelihood classification technique uses the average spectra and the covariance matrix of each spectral training site to map image data into categories or

classes of land cover while mixture analysis uses only the average spectrum for each endmember. In a maximum likelihood classifier all pixels, whether they are mixed or not, are treated as being pure pixels. This assumption repeatedly results in mixed pixels being assigned to constituent or extraneous classes (Foschi, 1994). Table 4-1 summarizes the main differences between maximum likelihood classifier and mixture modeling.

Along with the reasons pointed out above, scale related issues and spatial variability (which are intimately related) also play an important role when deciding upon the use of mixture analysis instead of other traditional image classification techniques. For example, the spatial resolution of AVHRR, about 1.1 km, precludes monitoring land cover or mapping landscape features with the traditional techniques of image classification because patterns of land cover types are typically of a similar or smaller size (Hlavka and Spanner, 1995).

Methods

Site Description

The study site (Figure 2-1) is located within the Walnut Gulch Experimental Watershed. This Watershed encompasses an area of 150 square kilometers in southeastern Arizona (31 degrees and 43 minutes North and 110 degrees and 41 minutes West) surrounding the historical western town of Tombstone.

The first survey at the level of soil series of the soils of the Walnut Gulch Experimental Watershed took place in 1970 (Gelderman, 1970). Gelderman (1970) found six soil associations and 23 soil series in the Watershed.

Table 4-1 Comparison between supervised maximum likelihood classifier and mixture modeling.

Maximum likelihood	Mixture modeling
<p>1- Class</p> <p>2 - Class are defined using training sites. To satisfy the statistical requirements many pixels are necessary for each site and several sites per class</p> <p>3- Classes are theoretically homogeneous</p> <p>4- The number of classes is limited only by the analyst's experience in finding ground cover classes of importance for the context of the analysis</p> <p>5- Pixels are forced to be classified to that class with the largest probability</p> <p>6- Classification at the pixel level</p> <p>7- Shade could be a class. However, if not eliminated (by using, for example, band ratio images), shade could be responsible for large differences in spectral responses of one class</p> <p>8- Uses estimatives of statistical parameter (mean, standard deviation) under the assumption that the samples have gaussian (normal) shape for the probability distribution function</p>	<p>1- Endmember</p> <p>2-Endmember can be defined using only one pixel from the image cube</p> <p>3- Because image endmembers are modeled by "reference endmembers" the image endmember are not necessarily "pure pixel" for that particular image feature. This is important when dealing with images where it is not possible to find pixels with a unique type of cover such as vegetation in a semiarid grass or scrubland</p> <p>4- The number of endmembers is limited by the number of bands. Thus, the maximum number of endmembers should be lesser than the number of bands</p> <p>5- Pixels are presented as a mixture of endmembers. Fraction images can be generated on the base of the concentration of each endmember in each pixel</p> <p>6- Classification at subpixel level</p> <p>7- Shade is always present as an endmember</p> <p>8- Uses mathematical models most often under the assumption that the response follows a multivariate linear model. However, non-linear spectral mixing is known to occur in intimate mineral mixtures in rocks, particulates and powders when strong absorptions are found in at least one of the minerals present. Non-linear spectral mixing among vegetation, soil, and shade primarily result from NIR transmission/scattering of light by leaves. Because leaves transmit/scatter NIR light, they behave as secondary light sources illuminating both shadowed and unshadowed soils</p>

Recently, Breckenfeld (1995) accomplished a new soil survey (scale 1:24,000), also at the level of soil series. In his survey Breckenfeld found 30 soil units with the major soil unit being Elgin-Stronghold, Luckyhills McNeal, McAllister-Stronghold, and Tombstone.

The soils of the Watershed are diverse in relation to their genesis. When considering the parent material, some of the major soils, such as Stronghold and Tombstone were largely influenced by the presence of limestone, while others, such as Baboquivari and McAllister have as their parent material mixed fan alluvium. In relation to the influence of the time on the development of the soils of the Watershed, these soils varied from very young (as those located in on flood plains, such as Combate soil series) to very old, such as the McAllister soil series. Old soils such as McAllister have an argillic horizon while other such as Stronghold presents petrocalcic horizons. Graham and Epitaph soil series are dark soils originating from slope alluvium and residuum from basaltic rocks. Epitaph is a Vertisol and, as such, has a high potential of shrink-swell. This properties is not present in Graham soil series.

Changes in climate related to elevation also affect the development of the soils at the Walnut Gulch Experimental Watershed. Thus, ustic aridic thermic conditions (mean annual temperature between 17 and 19 °C, and precipitation between 300 and 400 mm) are presented at elevations of 1,200 to 1,500 m, where most of the soil series occur (such as McAllister and Stronghold). The aridic ustic thermic conditions occurs at higher elevations where the annual average temperature is between 14 and 17 °C and the annual average precipitation is between 400 and 500 mm. These are conditions that favor the presence of Mollisols, such as the Budlamp soil series. Throughout the Watershed precipitation occurs as summer thundershowers and gentle winter rains.

Inside the area imaged by AVIRIS there are 14 (Figure 4-1) of the 26 soil series mapped by Breckenfeld (1995) are found at the Watershed. Six of the fourteen soil series represents more than 90 percent of the area of the Watershed covered by AVIRIS image. The classification at the family level and some of the physical and chemical characteristics of these six soils are presented in Table 2-1 and Table 2-2 (on Chapter two), respectively.

Historically, the area of the Walnut Gulch Experimental Watershed was occupied by grass about one hundred years ago. At the present time, grassland represents one third of the Walnut Gulch Experimental Watershed while the remaining area is occupied by shrubs. Among the shrubs, the most important species are represented by: Creosotebush (*Larrea tridentata*), Tar-bush (*Flourensia cernua*), Snakeweed (*Gutierrezia* sp.), Burroweed (*Isacoma tenuisecta*) and, Bear grass (*Nolina microcarpa*), which is particularly important in the area imaged by AVIRIS. The major grass species are: Black grama (*Bouteloua eriopoda*), Blue grama (*Bouteloua gracilis*), Sideoats grama (*Bouteloua curtipendula*), Lehmanns lovegrass (*Eragrostis* sp.), Sacaton (*Sporobollus wrightii*).

Pre-processing AVIRIS Data

The AVIRIS scene of Walnut Gulch Experimental Watershed was pre-processed as described in Chapter 3. For calibration purposes ATREM (as described in Chapter 3) was also used.

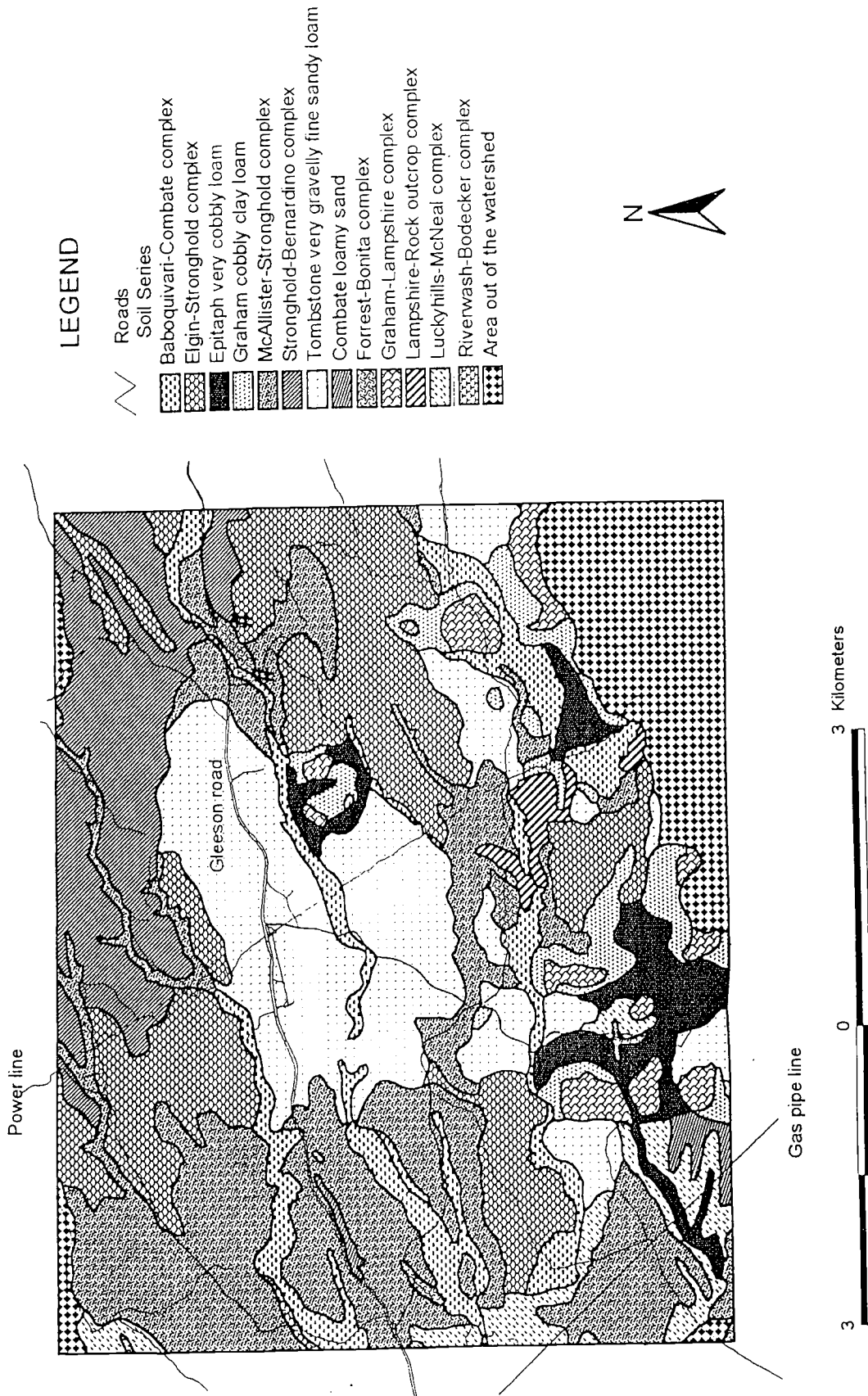


Figure 4-1 Soil map of the area of the Walnut Gulch Experimental Watershed imaged by AVIRIS

Spectral Mixture Analysis

There are two varieties of spectral mixtures: macroscopic and intimate (Farrand et al, 1994; Huete and Scadafal, 1991). Macroscopic mixtures result when there is a single set of interactions between surface materials and photons. That is, a given photon will be reflected (or absorbed) by only one type of material. Intimate mixtures occur when individual photons interact with more than one type of material. The reflected radiance of macroscopic mixtures combine in an additive fashion producing a linear set of equations. Intimate mixtures are nonlinear.

Although non-linear mixing models have been reviewed in some papers (Johnson, et al., 1992; Johnson, et al., 1983; Shipman and Adams, 1987), the methodology reviewed here deals only with linear models, in particular with that developed by Smith et al. (1987) and presented in several publications (Adams et al., 1989; Adams et al., 1993; Smith et al., 1990a; Roberts, 1991; Roberts et al., 1993; Farrand et al., 1994). One modification in this methodology with respect to target detection of reference endmembers is presented in the item "mixture analysis using reference endmembers" of this chapter.

Image Endmembers. The objective of SMA is to identify the materials in the scene in which spectra are the main contributors for the spectral response in each pixel. In the model suggested by Smith et al. (1987), this is done in two steps. In the first step the whole image is modeled using the spectra extracted from selected pixels. The selected pixels are representative of features in the scene and are called "image endmembers". As in most images, endmembers are non pure pixels a second step is needed in which the image is modeled on

the basis of "pure" spectra of the representative constituents of the image endmembers. These "pure" spectra are called "reference endmembers".

In dealing with mixture analysis, one of the first questions to be asked is: how many image endmembers are in a particular scene? The answer to this question gives us the dimensionality of a given image in terms of image endmembers. One way to find the image endmember dimensionality on the AVIRIS image is to use the principal component analysis. The abstract solution of equation 3.6 (Chapter 3) gives the number of image endmembers. Although principal component analysis also give clues about where those image endmembers are located, the knowledge of the area imaged by AVIRIS in the Watershed was used to pick up the best pixels for image endmembers. In a spectral mixture model the selection of image endmember constitutes the basic step toward pixel spectral decomposition. This is because, when appropriately selected, those image endmember pixels reproduced all or most of the pixel spectra of AVIRIS scene. Hence, image endmembers were selected on the registered and atmospherically (ATREM) corrected AVIRIS image. Well registered AVIRIS images allowed picking up of the correspondent pixels of features of interest in connection with ground inspection, while the atmospherically corrected data allowed picking up of the spectrally less "contaminated" pixels in relation with those features.

To account for natural variations in illumination, the spectra for each image endmember was selected from areas that received maximum illumination. A mandatory image endmember in mixture analysis is "shade". The shade image endmember (taken from "pure" pixel in a shadow cast by topographic features, or from other dark areas in scene, or even

from a modeled spectrum) can mix in all proportions with each of the other endmembers or with their mixtures, thereby modeling the spectrum of the endmember material when it is not fully illuminated (Adams et al., 1993). To model shade endmember, dark pixels located in areas of volcanic rocks and a modeled shade spectra with a constant reflectance of 10 percent as used by Farrand et al. (1994) were tested.

Once the spectra of the image endmembers have been defined, the spectra of any mixture of the endmembers can be calculated by applying the following equation:

$$P_c = \sum_{i=1}^N F_i R_{i,c} + E_c \quad 4.1$$

with the constraint that

$$\sum_{i=1}^N F_i = 1 \quad 4.2$$

In equation 4.1 P_c is the relative reflectance value in channel c of an image pixel; F_i is the fraction of the endmember i ; $R_{i,c}$ is the relative reflectance of the endmember i in channel c ; N is the number of endmember; and E_c is the error for channel c of the fit of N spectral endmembers. If there are M spectral channels, there can be M or fewer endmembers. The equation requires that the fractions of the endmembers sum to one.

We used the three criteria suggested by Adams et al. (1993) to test the model on the base of the image endmembers. In the first criteria we used the average rms error (ϵ) for the 167 AVIRIS bands utilized in this work,

$$\epsilon = [M^{-1} \sum_{c=1}^M E_c^2]^{1/2} \quad 4.3$$

Where M is the number of bands (in this case M = 167)

A small value for ϵ implies a good agreement between the predicted spectrum on the base of the image endmembers and the spectrum of the correspondent pixel in AVIRIS image. An average rms error image can be generated in which higher values of error are displayed as lighter pixels.

As a second criteria, the variability in the model is examined in a spatial context by using "fraction images" (F_i). If patterns of F_i in the fraction images are consistent with ground or other observations, then the model may have been constructed correctly. In the third criteria the fractions of endmembers are checked to determine if they fall in the range of zero to one. If the mode is inadequate the computed image endmember fractions may fall outside this range. If the initial model does not fit the data satisfactorily, one or more additional endmembers can be selected by using light pixels in the rms-error (ϵ) image.

Fraction Images. Once the multispectral image data are expressed as fraction of endmembers, information can be selected and deleted which is necessary to arrive at units that are consistent with field observation and field maps. Another useful way to present the

fractions of the endmember (either image or reference endmembers) is by color coding ranges of fractions. For example, three different colors for ranges of fractions can be assigned that vary from 0 % to 33 %, 34 % to 63 %, and 64 % to 100 %. Significantly, combinations of selected fraction images can be displayed while leaving out others. Since this is concerned with the spatial distribution of the soil spectral classes, fraction of shade or any other endmember other than soil (or even more than one endmember) can be deleted by rescaling all fractions so that the fractions of the different soil endmembers sum to unity. For example a pixel with the following fraction distributions: 0.33 vegetation, 0.33 soil, and 0.33 shade and can be rescaled by deleting the shade fraction. The new fractions in the rescaled pixel will be 0.5 vegetation and 0.5 soil. Fractions can be rescaled by the following equation:

$$S_i F_s = S_i F / (1 - \text{Shade}F) \quad 4.4$$

Where:

$S_i F_s$, is the scaled fraction of the soil i endmember,

$S_i F$, is the fraction of the soil i endmember, and

ShadeF, is the shade fraction (or the fraction of any other materia to be deleted)

As a result of applying equation 4.4, a scaled soil fraction image will be produced.

Fraction images are a powerful tool for isolating parts of the image data and for quantifying the amount of the materials that are present. Thus, they are substantially important in detecting temporal and spatial changes in several biomes.

Reference Endmembers. To compare image endmembers with the laboratory of field spectra, or if there are no pure pixels in the image that represent the desired materials (for example, in a semiarid scrubland where, in most of the cases, every pixel has vegetation, soil and shadow), it is necessary to define new endmembers from laboratory or field reference spectra (Smith et al., 1990). These new endmember spectra are termed "reference endmembers". To use reference endmembers, the image data must be converted to reflectance. This can be done by using the model proposed by Smith et al. (1987) in which the calibration is performed without knowing the ground reflectance spectra. In this case, the combination of the best endmembers derived from laboratory of field spectra and the most plausible gains and offsets for each channel that are needed to make the reference endmember spectra fit are used. However, the same calibration can be done by using any radiative transfer model. In this case calibration was done by using the ATREM as describe in Chapter 3.

The spectral library prepared to test the fitness of the reference endmember in the model was composed by field, sieved samples, and RELAB spectra. Chapter 2 presents the details on how soil spectra were obtained for field, sieved samples, and RELAB conditions.

Along with soil spectra, other field reference endmembers were selected on the basis of their importance as detected by the percent of cover (Table 3-3). The spectra for materials other than soil were obtained in the field except for the rocks which were sent to RELAB. Table 4-2 presents a summary of the spectral library obtained from different conditions. In addition to spectral library from this research the spectra from the USGS spectral library was used.

Table 4-2. Spectral library utilized for the identification of potential reference endmembers

Category	Total Number of Samples	Conditions ⁽¹⁾	Remarks
Soil	30	Field ⁽²⁾ , Lab ⁽³⁾ , RELAB ⁽⁴⁾	
Rocks	22	Field, and RELAB	16 Field spectra 6 RELAB spectra
Vegetation	Ephedra=5 Dry Forbes = 14 Grass = 8 Bear Grass = 5 Creosote = 1	Field Field Field Field Field	
Litter	5	Field	

⁽¹⁾ Conditions under which the spectra were obtained.

⁽²⁾ Field spectra were obtained with Spectron SE590 for the range of 0.45 to 0.90 μm .

⁽³⁾ Lab spectra were obtained with Spectron SE590 for the range of 0.45 to 0.90 μm for sieved samples.

⁽⁴⁾ RELAB spectra were obtained for the range of 0.40 to 2.40 μm for sieved samples in the case of soil samples.

Problems Inherent in Selection of Endmembers. One of the problems in selecting endmembers is that some endmembers are spectrally indistinguishable. Smith et al. (1990a), using Landsat TM data from Owens Valley - CA, found that the reference endmember Artemisia was similar to that of several other species of bajada vegetation. Smith et al. (1990a) also found that the spectral ambiguity between dry grass and "tan" soil enabled them to resolve the mixture problem for these two classes.

Another problem associated with selection of endmembers is the completeness of the collection of reference spectra. Smith et al. (1990a) states that is not feasible to collect the spectra of all possible materials which implies that eventually unknown materials on the ground may masquerade as spectral mixtures of the reference endmembers that have been selected for the image. Goetz and Boardman (1989) emphasized the importance of spectral contrast between endmember spectra in obtaining accurate spectral fractions, particularly with noisy data.

A complicated factor in selecting endmembers is that for some materials, it is not possible to obtain a linear combination of the component spectra. Non-linear spectral mixing is known to occur in intimate mineral mixtures in rocks, particulates and powders when strong absorption are found in at least one of the minerals present (Roberts, 1991). For instance, Roberts (1991) found that the primary effect of leaf transmission/scattering of light was to produce non-linear spectral mixing between leaves and a background.

Another problem that can occur in selecting endmembers is related to the spectral variability inherent to the endmembers. In spectral mixture analysis, each endmember is used to describe the spectral contribution of an individual component in an image that may, in fact,

be spectrally variable within the scene. This variability can be a source of uncertainty in determining target detection thresholds (Sabol et al., 1992.)

Results and Discussion

Principal Component Analysis

Table 4-3 presents the distribution of the total variance between the component images after applying principal component analysis (PCA) on the AVIRIS image. Although the first component (99.75% of the total variance) explains most of the total variance, some information remains in other components (Table 4-3). The importance of the remaining information in adding a higher dimensionality to AVIRIS data can be analyzed in several ways. Malinowski (1991), presents empirical methods such as the imbedded error. The imbedded error function reaches a minimum for four components which means that the number of primary vectors that should be included in the model is also equal to four. Another practical way to define the number of components is through the visual inspection of the PCA images. The visual analysis of the component images presented in Figures 4-2 through 4-4 also reveal that the dimensionality of the AVIRIS data is given for the first four component images.

The first component image (Figure 4-2a) presents an idea of the how spatial brightness varies and carries the information of the average albedo of the AVIRIS image. As reported in Chapter 3 - for the reconstruction of the soil spectral curves - one factor generates soil curves that differ only in brightness magnitude. Thus, the reconstruction of the spectral curve for each pixel on the basis of the first component will generate spectral curves that are parallel

Table 4-3. Summary of the principal component analysis for the first 6 components

PCA Number	Eigenvalue	Percent of the total variance explained by the component	Real Error	Imbedded Error
1	1.62×10^{12}	99.75	1.21	0.940
2	2.45×10^9	0.15	0.76	0.830
3	7.55×10^8	0.046	0.55	0.732
4	2.08×10^8	0.013	0.47	0.729
5	9.22×10^7	0.006	0.43	0.752
6	4.44×10^7	0.003	0.42	0.788



(a)



(b)

Figure 4-2 First (a), and second (b) component images

to each other with differences only in terms of brightness magnitude.

Although difficult to interpret on the basis of spatial variation, a great deal of information can be extracted from the other component images. Thus, the second component image (Figure 4-2b) enhances the contrast between bright soils (mainly Tombstone and Stronghold-3 which appear in light tones of grey), red soils (McAllister and other soils outside Walnut Gulch Watershed, which appear bright) and dark areas (represented by cinder cone, Graham soil, and shade, which are dark).

The third component (Figure 4-3a) enhances the contrast between washes, green vegetation (which is also a feature associated with the presence of washes) appears in light tones of gray and other features in the image now appear in dark tones of grey. On the other hand, for the fourth component (Figure 4-3b) areas of green vegetation appear dark instead of bright (as it appears in the third component). These differences in contrast when comparing the same features in different components are an expression that the component images are highly uncorrelated. This is also true when comparing the cinder cone/Graham soil areas in the component two image (Figure 4-2b) (where cinder cone/Graham areas appear in very dark tones) to the same areas in component four image (Figure 4-3b) (where these areas appear in light tones of gray). The enhancement of other features in component four image, however, is even more difficult to interpret. For this component, image bright and dark shades of grey are mixed in patterns almost impossible to associate with ground features present in the AVIRIS scene. Thus, in the component four image, the enhancement effect over washes and roads, which are clear in component images one and two, almost disappear.

The fifth and sixth component images (Figures 4-4a and 4-4b) contains less image



(a)



(b)

Figure 4-3 Third (a), and fourth (b) component images

structure than the other components and typically represent instrumental noise.

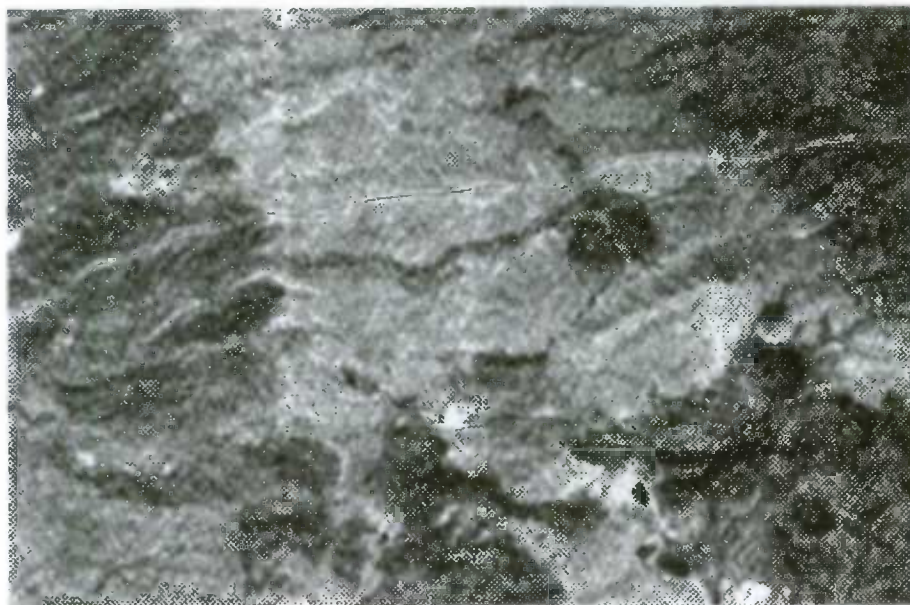
The uncorrelated eigenvectors (referred to as eigenspectra from here on) for components one through six are presented in Figure 4-5a and Figure 4-5b. In Figure 4-5a the first eigenspectrum resembles the shape of most of the soil spectra extracted from the AVIRIS image as shown in Chapter 3. Except for the average albedo given by eigenspectrum one curve (discussed above), the other eigenspectrum curves are difficult to interpret. The curve for eigenspectrum two could be associated with dark features in the image, such as the dark cinder cones and Graham soil series. The positive-negative effect described by Schowengerdt (1983) for the first two component images can also be seen in Figure 4-5a. Thus, these two eigenspectrum curves present a mirror-like form where the first eigenspectrum curve increases with the wavelength while the second eigenspectra curve decreases with the wavelength. The third eigenspectrum curve resembles the monotonic and concave shape of Tombstone and Stronghold-3 soils while the fourth eigenspectrum curve resembles mirror-like curves for green vegetation. The eigenspectrum curves five and six do not present much information and seem to be associated with instrumental noise.

Mixture Analysis Using Image Endmembers

Once the dimensionality of the data set is determined by the PCA, the next task is to discover what the endmembers are and where they are spatially located. Data from Chapter 3 was used to give an indication of the spectral groups of soils. Chapter 3 (see Figure 3-17d) reveals that for soil spectra collected under field, for nadir viewing angle, and under dry conditions three to four groups of soils are present. One reasonable approach is to divide the



(a)



(b)

Figure 4-4 Fifth (a), and sixth (b) component images

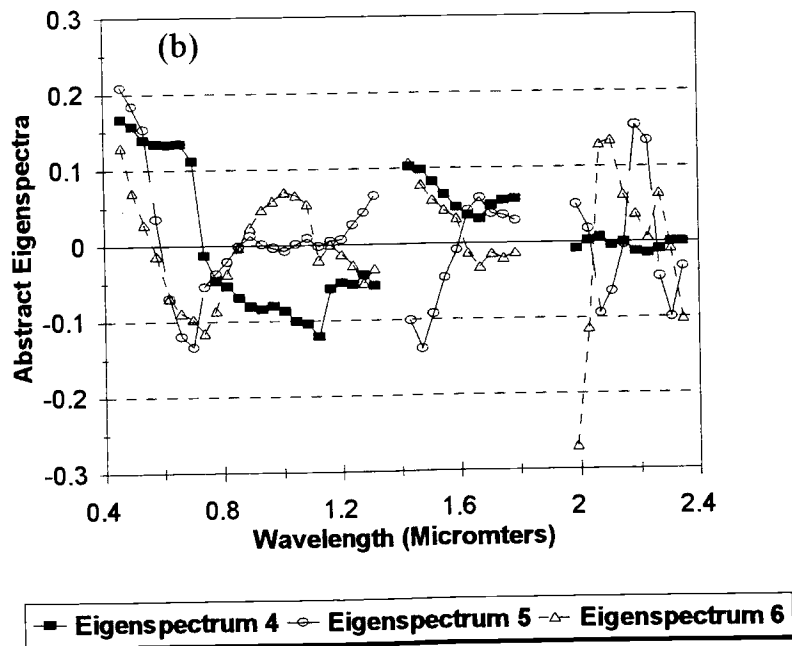
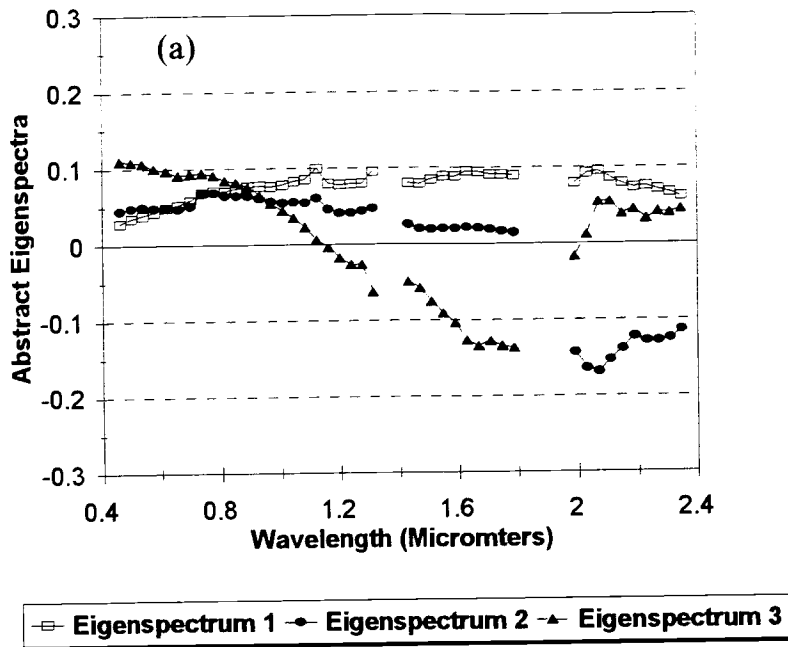


Figure 4-5 The first six abstract eigenspectrum curves following the decomposition of AVIRIS image using PCA

soils into three groups with Stronghold-1, Stronghold-2, Stronghold-3, Tombstone, and Baboquivari in one group, Epitaph and Graham in the second group, and McAllister isolated in a third group. Similarly Figure 4-6 shows the final grouping of the soils, if now the average spectra of the selected window for each soil from the AVIRIS image is clustered (see methodology in Chapter 3 for details).

Four groups of soil spectral classes can be visualized in Figure 4-6; the first group contains Baboquivari and Stronghold-1; the second group contains Graham and Epitaph; the third is composed of McAllister and Stronghold-2 and the fourth is composed of Stronghold-3 and Tombstone. The fact that the three Stronghold sites (Stronghold-1, Stronghold-2, and Stronghold-3) are now in three different clusters emphasizes the initial idea of sampling this soil series in three different locations and also shows that other types of surface cover (such as vegetation, litter and rocks) in addition to bare soils, play an important role in extracting soil spectral information in semiarid environments.

The use of the average curve of each cluster as a potential endmember was considered; however, this procedure has no physical meaning once the average curves do not pertain to any of the soil series on the map. Therefore each of the spectrum from each of the four soil clusters presented in Figure 4-6 were tested in different combinations. The test of the physical meaning of the four image endmembers defined by the principal component analysis was done by using four spectra that included in addition to soil spectra the modeled shade spectrum and a "pure" spectrum of green vegetation. The visual analysis of the residual image provided the answer for the best combination of the four spectra (image endmembers) need to model the entire AVIRIS imagery.

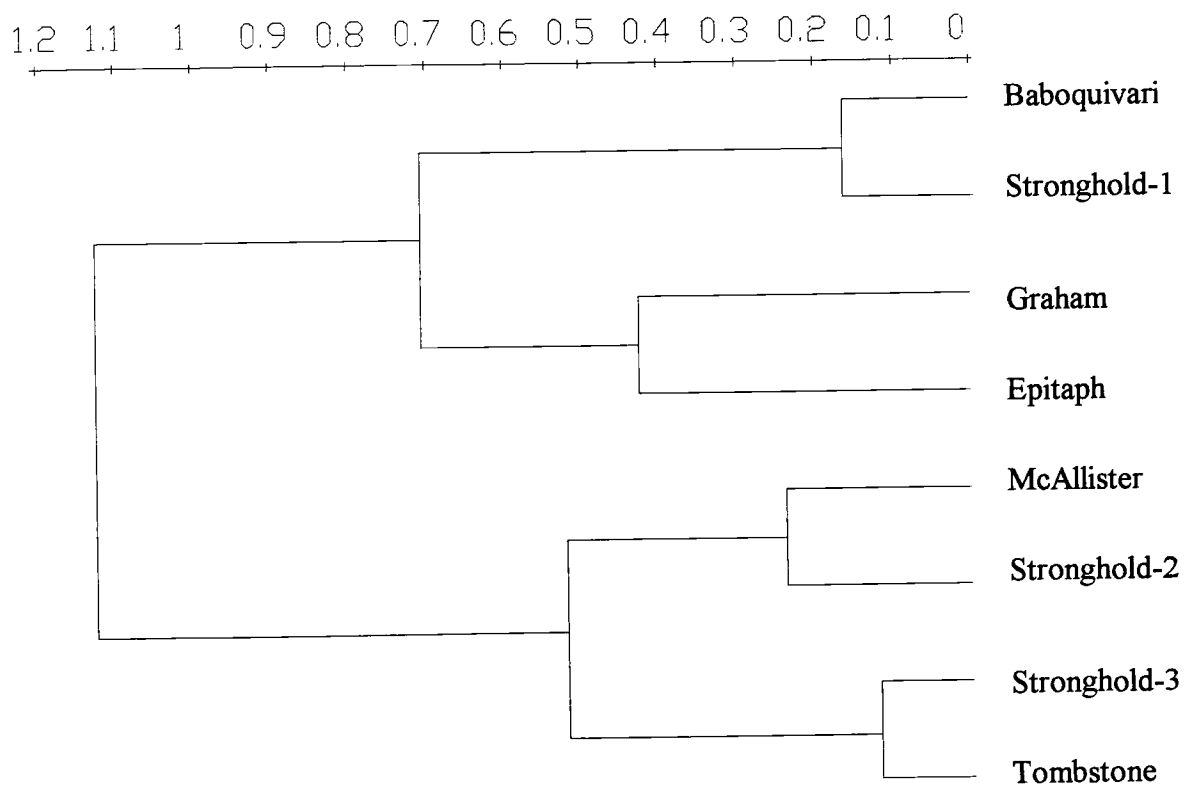


Figure 4-6 Dendrogram obtained after applying cluster analysis to the average spectra extracted for each soil from AVIRIS imagery

These were: McAllister soil, Stronghold-3 soil, Graham soil and green vegetation. The fact that Graham, Epitaph and cinder cone (at the level of soil series, areas with cinder cone were classified as Graham Rock Autocrops) are spectrally too dark made the modeled shade spectra useless in all combination of image endmembers used in the mixture model of AVIRIS image. Also, no difference was found when using the model for the spectra from either Graham, Graham Rock Autocrops or Epitaph soil. Thus, the visual inspection of the error images from the models that included modeled shade, Graham, Graham Rock Autocrops or Epitaph soils, presented no significant differences when in combination with the other selected image endmembers (McAllister, Stronghold-3, and green vegetation).

Figure 4-7 shows the atmospherically corrected AVIRIS spectra for each of the selected image endmembers, while the spatial pattern and variability of the combined rms error after applying mixture modeling using these image endmembers is shown in Figure 4-8. The combined average rms error after applying mixture analysis to the 167 AVIRIS bands was 0.026 or 2.6 % reflectance. For a better visual interpretation of the distribution of the error, the rms image was linearly stretched. The combined rms error image displays high values of rms error in light tones of gray, while the dark portions of these images represent the parts of the AVIRIS image where the model fits well. Features in AVIRIS image that were not well modeled by mixture model are represented by roads (most of Gleason Road can be seen near the middle portion of the image), part of the cinder cone areas (in the middle of the bottom of the image), and other areas located outside of the Walnut Gulch Experimental Watershed (seen in the bottom left of the rms error image).

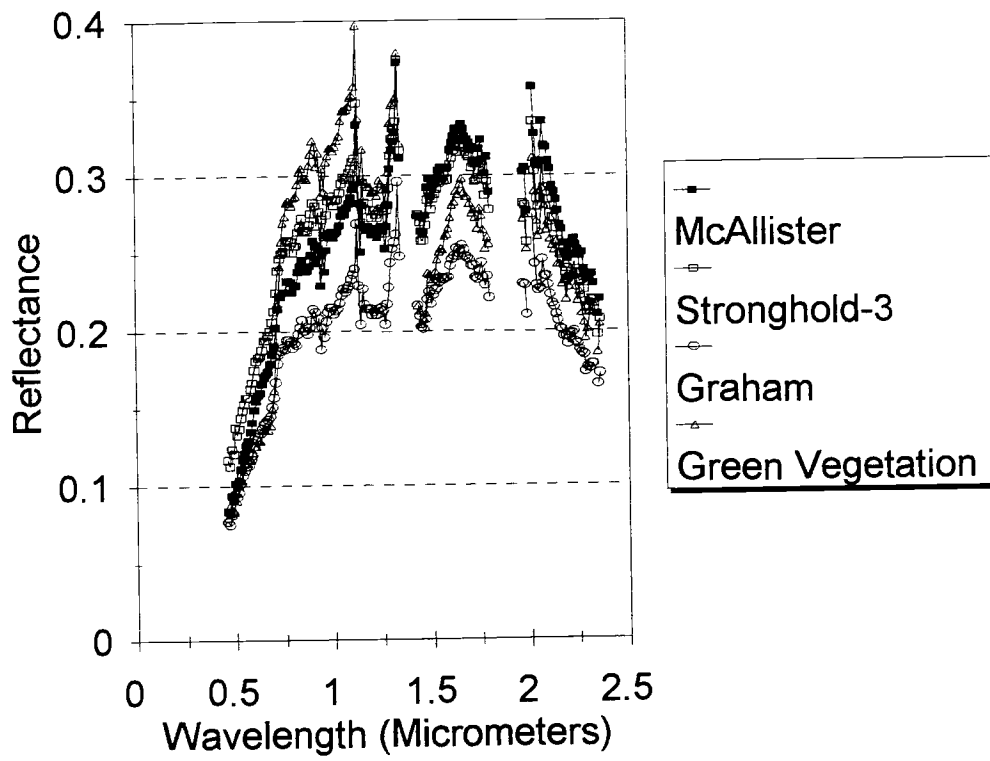
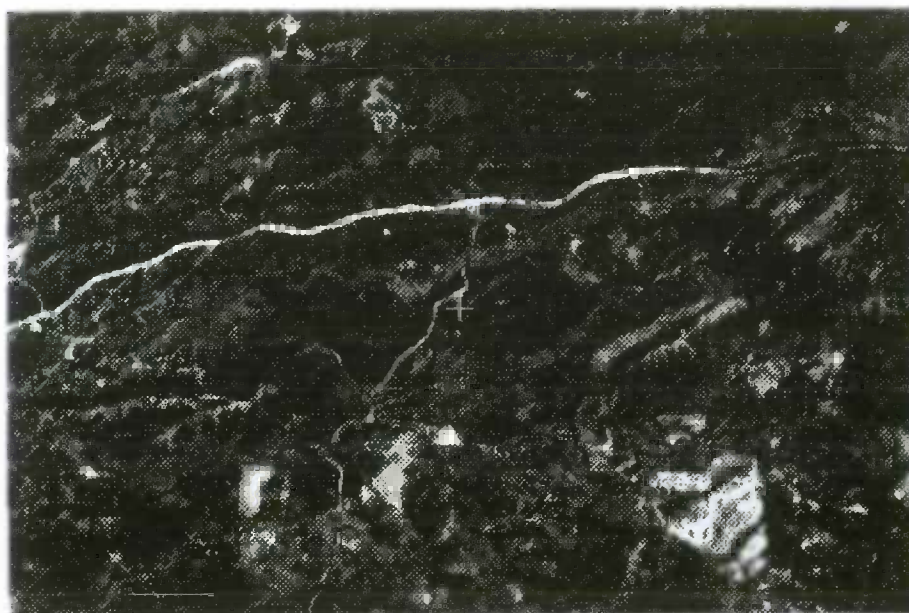


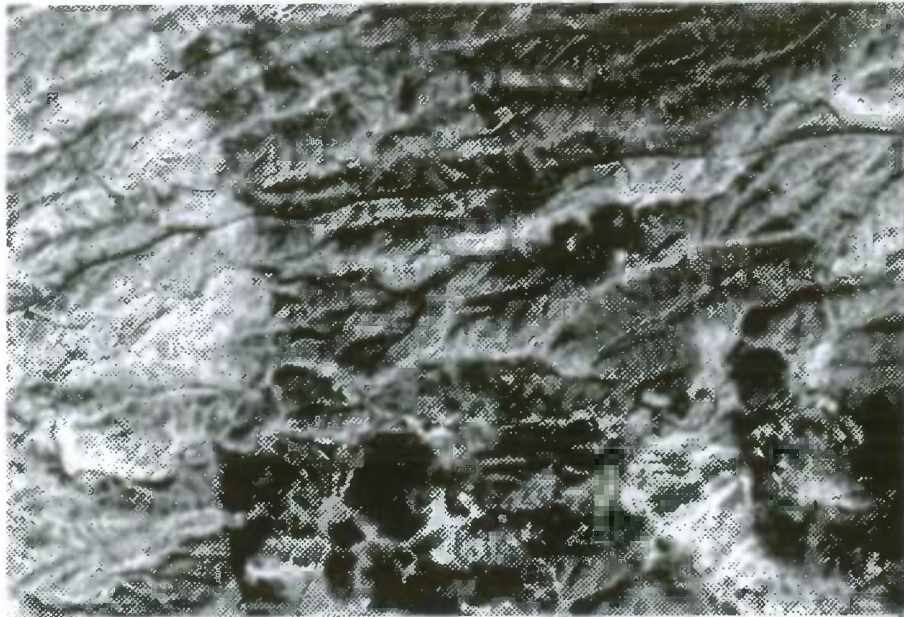
Figure 4-7 Spectral curves for each of the selected image endmembers



**Figure 4-8 Error image after applying mixture
analysis using image endmembers**

Figures 4-9 and 4-10 present the fraction images for the four image endmembers model. In these images the higher the pixel brightness the higher the fraction of a given image endmember. McAllister fraction dominates the left third of the AVIRIS scene and also parts of the area outside the Watershed (Figure 4-9a). Once Graham and Graham Rock Autocrops present soil characteristics (mainly related to parent material, soil surface color, and type and distribution of soil textural fractions) that are different from that of McAllister and Stronghold-3 soils, it can be assumed that light gray tones in areas of occurrence of these two soils and shown in the Graham/shade fraction image (Figure 4-10a) are due to topographic effects. Thus, the gentle slope of McAllister soil causes a decrease in the shade fraction of this soil (Figure 4-9a). McAllister soil occupies areas of fan terraces which are the oldest landform in the Walnut Gulch Experimental Watershed. In this landform weathering had enough time to give rise to this deep and well developed soil. Under these conditions, comparatively, McAllister soils are much less affected by topographic shadows than Stronghold-3 and Graham soils. Due to small differences in the spectral contrast between McAllister soil and other soils present in the AVIRIS scene, soils, such as Stronghold-1, Stronghold-2, and Baboquivari, were misclassified as containing a high fraction of McAllister (Figure 4-9a).

The middle portion of the AVIRIS imagery is dominated by Stronghold-3 fraction (Figure 4-9b). This area encompasses not only Stronghold-3 soil but also most of the area of Tombstone soil (compare to the soil map of the Walnut Gulch Experimental Watershed present in Figure 4-1). The Stronghold-3 fraction is also more affected by topographic shadows than McAllister fraction as shown in Figure 4-10a.



(a)



(b)

Figure 4-9 McAllister (a) and Stronghold-3 (b)
fraction images



(a)



(b)

Figure 4-10 Graham/Shade (a), and green vegetation (b) fraction images

Although the basalt rocks and their associated Graham, Graham Rock Autocrops, and Epitaph soils cannot be distinguished spectrally from the shade pattern, these feature can be spatially distinguished in their fraction image (Figure 4-10a). Graham Rocks Outcrops, Graham, and Epitaph soils appear concentrated in the middle/bottom of the image and also in the left/bottom and in two spots near Gleason Road and the power line. Those areas are very bright and their pattern (bowl-like shape) are quite different from the pattern of the shade that appears in other areas (such as those occupied by Stronghold-3 and Tombstone) which are due to topographic effect (a variegated pattern of bright and dark pixels present in Figure 4-10a).

Higher fractions of green vegetation are concentrated along the washes in some north facing slopes and in the button/left side (area outside the Watershed) of the green vegetation fraction image (Figure 4-10b). Higher fractions of green vegetation are present in areas occupied by Stronghold-Bernardino, Tombstone, and Baboquivari-Combate soil series than in other soil series present in the area imaged by AVIRIS (see the map of soils in Figure 4-1). The effect of north face slope could be associated with the presence of more green vegetation in areas such as Stronghold-Bernardino and Tombostone soil series, while the presence of washes in the nearby Combate soil series can favor the presence of green vegetation in dry period of the year.

Since a main objective of this study is the spatial distribution of the soil spectral classes, all the fractions were normalized in terms of soil spectral endmembers. As already described, this is easily done by subtracting the green vegetation contribution from each pixel and rescalling the other fractions. For a better visualization of the subpixel distribution of each

soil endmember, maps were generated (Figures 4-11a, Figure 4-11b, and Figure 4-12) by color coding pixels, using ranges of the scaled soil fractions.

The color coded map for McAllister fraction image (Figure 4-11a) shows that most of pixels containing more than 70 % of this soil are located in the left portion of the AVIRIS image. Pixels having less than 30 % of McAllister soil are located in the upper left corner, and in the middle bottom of the AVIRIS image. The color coded fraction image of Graham/shade endmember (Figure 4-11b) shows that pixels with more than 70% of the area covered by this endmember correspond to areas occupied by Graham, Graham Lampshire soil series and Epitaph soil series. The color coded map of Stronghold-3 (Figure 4-12) fraction reveals for certain areas a smaller contribution of this soil in some pixels than what was expected. There are two reasons for this. First, the area dominated by Stronghold-3 soil (and other spectrally similar soils, such as Tombstone) is highly affected by the topography. Second, certain areas where Stronghold-3 dominates (such as in the upper left corner of the AVIRIS image) have a high density of dry vegetation (areas surrounded by fences, which can be seen clearly in the color contrast of the color coded fraction image of Stronghold-3 soil - upper left corner of the image). Both, the topography and the high amount of dry vegetation contribute to the increase of the shade fraction and, as a result, only small fractions of Stronghold-3 soil are distinguished in some areas where this soil dominates.

To exemplify the effect of shade in Stronghold-3 soil Figure 4-13 presents a window (170 x 100 pixels) extracted from the upper left corner of the AVIRIS image. The fence line dividing the windows extracted from the scaled fraction image (without green vegetation) and from the color coded representation of this fraction image (Figure 4-13C, and Figure 4-13D)

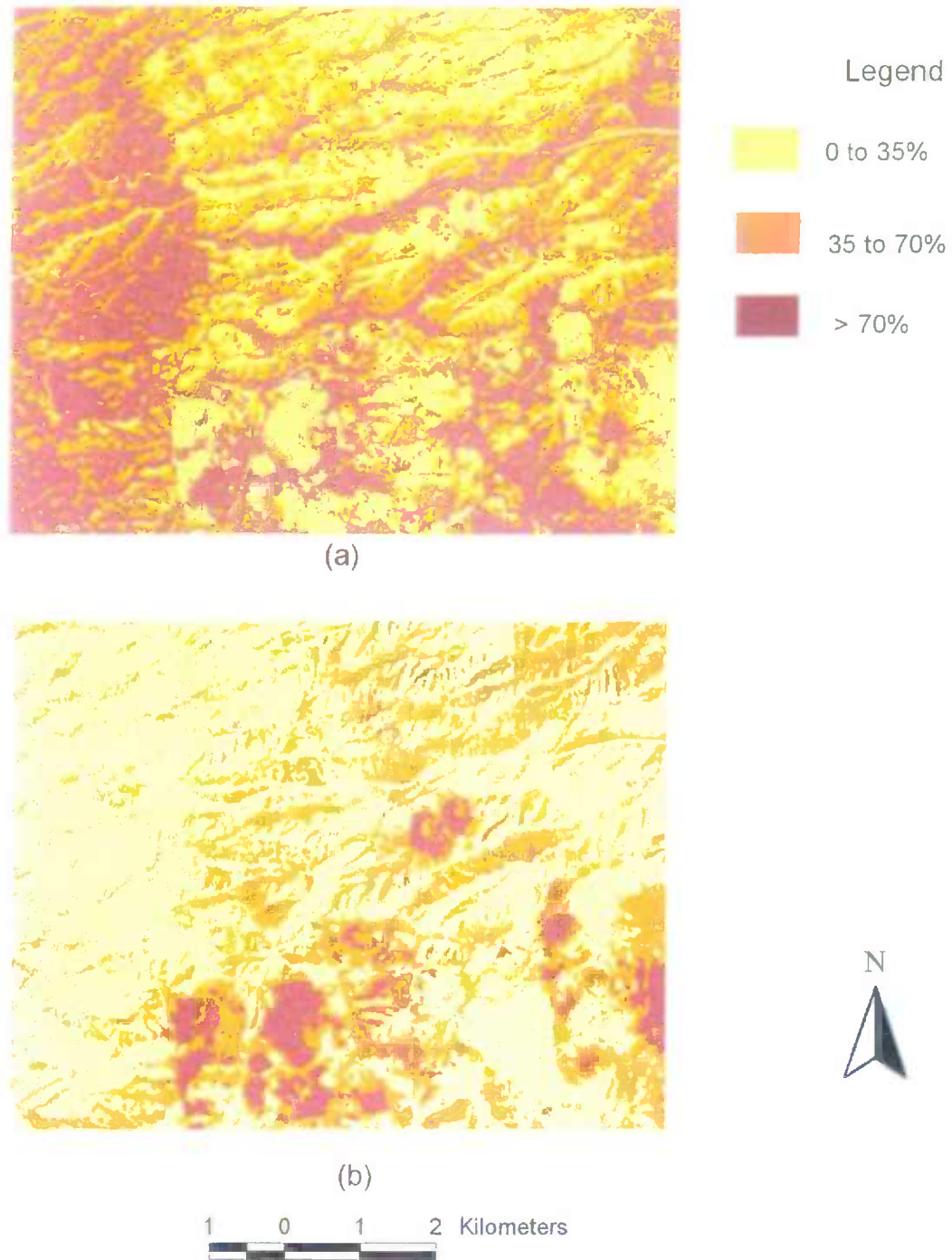
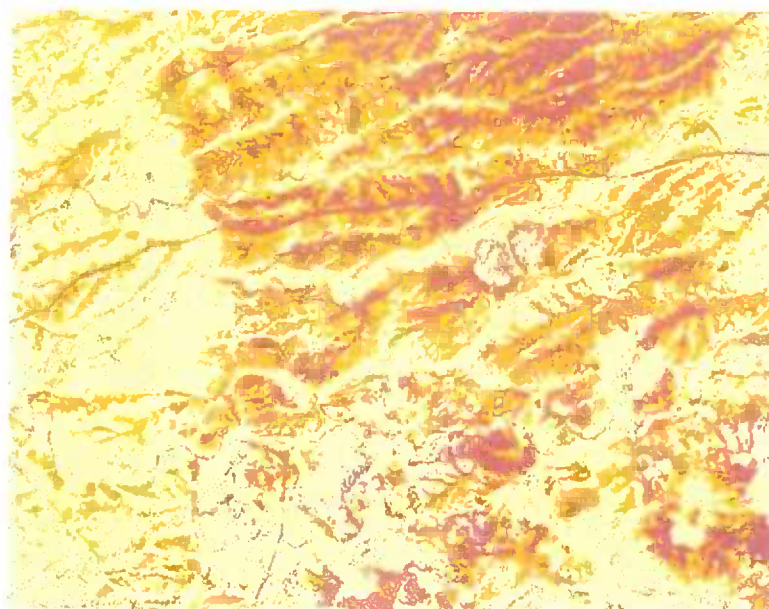


Figure 4-11. Color coded maps presenting the distribution of the fractions for McAllister (a) and for Graham/Shade (b) image endmembers



1 0 1 2 Kilometers

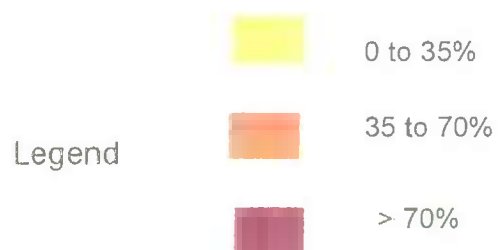


Figure 4-12. Color coded map presenting the distribution of the fractions for Stronghold-3 image endmember



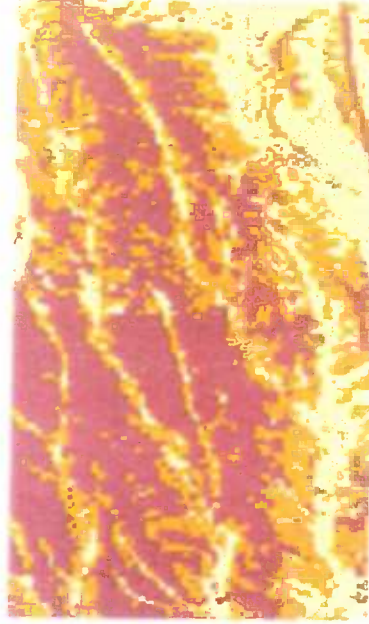
(A)



(B)



(C)



(D)

Figure 4-13. Scaled fraction images and color coded fraction images. (A) Fraction image with shade; (B) Fraction image without shade; (C) Color coded fraction image with shade; (D) Color coded fraction image without shade. The legend for colors is the same as for Figure 4-11.

can be seen clearly. The right side of the AVIRIS windows present in Figure 4-13 is dominated by a denser dry vegetation than the left side of those windows. Although differences in topography between the two sides of the fence have a role in the shade effect on the Stronghold-3 fraction, it seems that most of the shade effect is due to the higher amount of dry vegetation on the right side of the fence line. Thus, when subtracting the shade contribution from the image presented in Figure 4-13A, the resulting image (Figure 4-13B) presents almost no sharp contrast between the two sides of the fence line.

Figure 4-13B and Figure 4-13D show that areas close to the fence and located on both sides, which much the same topography, present comparable contributions of Stronghold-3 image endmember. Thus, as long as the terrain topography is known, the shade effect caused by dry vegetation can be eliminated from fraction images of soils of semiarid environments. To do the above normalization, along with the similar topography it is assumed that there is no differences in terms of species composition of the dry vegetation for the both sides of the fence.

Mixture Analysis Using Reference Endmembers

Selection of Potential Reference Endmembers. To model the AVIRIS scene of Walnut Gulch Experimental Watershed on the basis of the image endmember was a relatively easy task considering that on the basis of field experience pixels that are representative of each of the environment found in that image can be located. Pixels used as image endmembers, however, are composed of different materials and represent by themselves a mixture of these materials. Although the model using image endmembers presented good results in producing useful

spectral maps, the ultimate objective of mixture modeling is to generate fraction images on the basis of "pure" spectra (reference endmembers) obtained from lab or field studies. This two-step model, in which the spectral data are first modeled by using endmembers selected from the image which are in turn modeled as mixtures of library endmembers, has been used by several authors (Smith et al., 1990a; Farrand, et al., 1994).

Since most of the spectral library (including all spectra other than soils) was collected only for the spectral range of the Spectron SE590 spectroradiometer (0.45 to 0.90 μm) this study was done in the same spectral range for the AVIRIS data for modeling the image on the basis of reference endmembers.

A common problem faced in applying spectral mixture model is related to the selection of the reference endmembers. The problem is aggravated when a great number of different materials are present at the pixel scale as occurs in semiarid environments.

In addition to the type of soil, the percent of cover present in Table 3-3 gives an idea of the diversity of other materials that constitute potential reference endmembers to model the AVIRIS image of the Walnut Gulch Experimental Watershed, while Figure 4-14 shows the spectral curves taken in the field for these materials. Even though field surveys of the percent of cover and field spectra of these materials constitute the basic information for deciding the inclusion of a particular reference endmember in a spectral mixture model, it is still important that those field spectra can be discriminated in the AVIRIS signal. One way to avoid the test of every possible combination of "pure" spectral signatures is to test for the presence of suspected reference endmembers in the AVIRIS scene prior to their inclusion in the spectral mixture model.

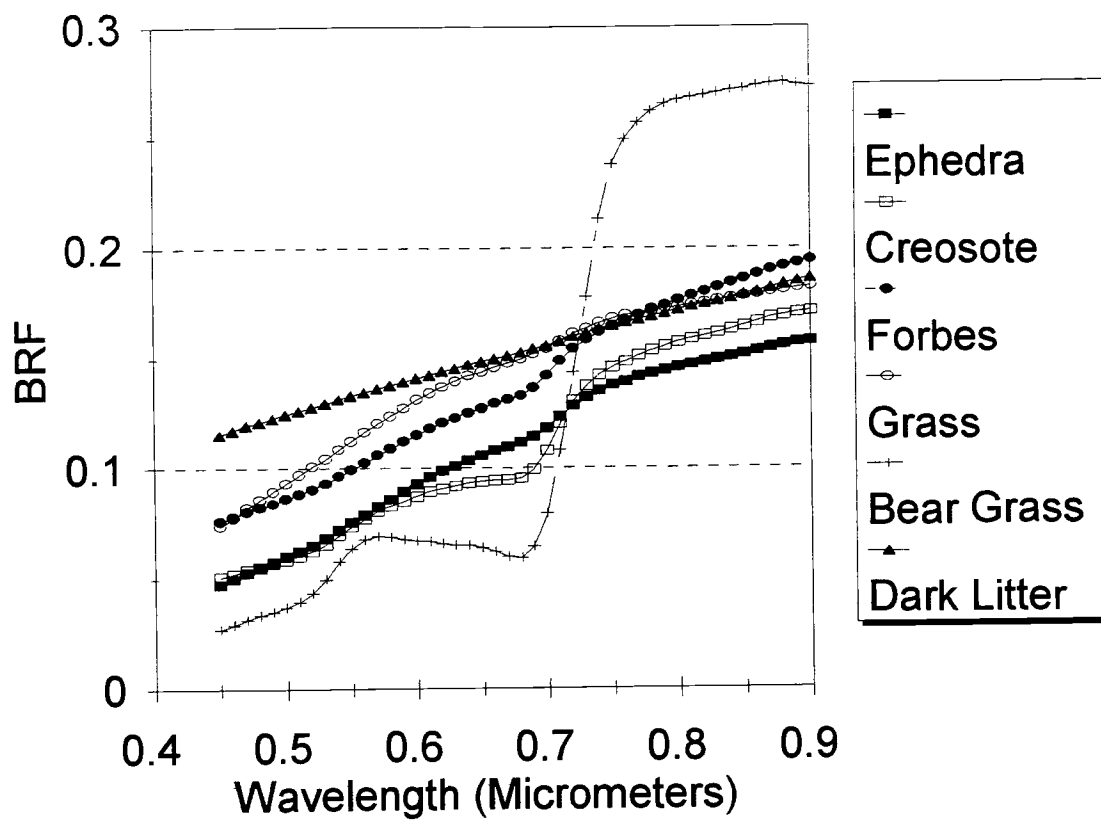


Figure 4-14 Field spectral curves for potential reference endmembers others than soils

The test for the presence of a suspected reference endmember in the AVIRIS image can be done by using the target test proposed by Malinowski and Howery (1980) and applied by Huete (1986). Once the suspected reference endmembers are detected by target test, they can be used to spectrally decompose the AVIRIS image. In the target test the abstract matrix, presented in the methodology of Chapter 3 (equation 3.7), is transformed through target rotation, utilizing the spectral curves of suspected reference endmembers. Transformations are accomplished by carrying out the following mathematical operations (Malinowski and Howery, 1980):

$$[\mathbf{R}]_{\text{real}} = [\mathbf{R}]_A [\mathbf{T}] \quad 4.5$$

$$T_i = [\lambda]^{-1} [R]_A^T R_i \quad 4.6$$

Where $[\mathbf{R}]_{\text{real}}$ is the real factor matrix (abstract factor matrix converted into physically-based factor matrix), $[\mathbf{R}]_A$ is the abstract factor matrix, $[\mathbf{T}]$ is the transformation matrix, T_i is a least square column vector transformer for each of the n endmembers, and R_i is the associated target test column vector, containing the spectral signature of the suspected reference endmembers.

To determine if the spectral signature of test vector (reference endmembers) is present in the data set, the predicted spectral signature R_p was computed.

$$R_p = [\mathbf{R}]_A T_1 \quad 4.7$$

If each element of the predicted spectral signature is equal to the corresponding element of the test signature, within the experimental error, then the suspected endmember is present in the data set and the column vector transformer T_1 is included in the transformation matrix. Target testing continues until all (n) endmembers are identified.

The target test was applied to the AVIRIS image to detect the presence of reference endmembers depicted in Table 4-2. Figures 4-15 through 4-18 present the results of applying the target test for determining the presence of selected reference endmembers. The potential soil reference endmembers were successfully predicted (Figure 4-15, and Figure 4-16), i.e., the predicted and tested spectra were much alike for all wavebands. Much of the error is concentrated in the NIR region of the spectra and can be attributed to the uneven atmosphere correction given by the ATREM code. The spikes presented by the predicted spectra in the region between 0.7 and 0.9 μm are associated with secondary absorption bands and with the oxygen absorption band near 0.76 μm (Huete, 1996). There is also one spike near 0.5 μm that could be attributed to overcorrection of the ozone absorption band. For the three soils, the RMS error is less than 6% of reflectance in any of the 46 bands and, specifically, for the visible region the RMS error for the predicted spectra is close to zero percent of reflectance. These results show that the soil reference endmembers were successfully predicted using the target test proposed by Malinsowki and Howery (1980).

The target test was also used to test for the presence of materials other than soils (see Table 4-2) in the AVIRIS imagery. Figures 4-16 through 4-18 present the fitness of the field spectra for dry forbes, litter, dry grass, and green vegetation (Bear grass, and Walnut leaf), to the predicted spectra extracted from the AVIRIS scene.

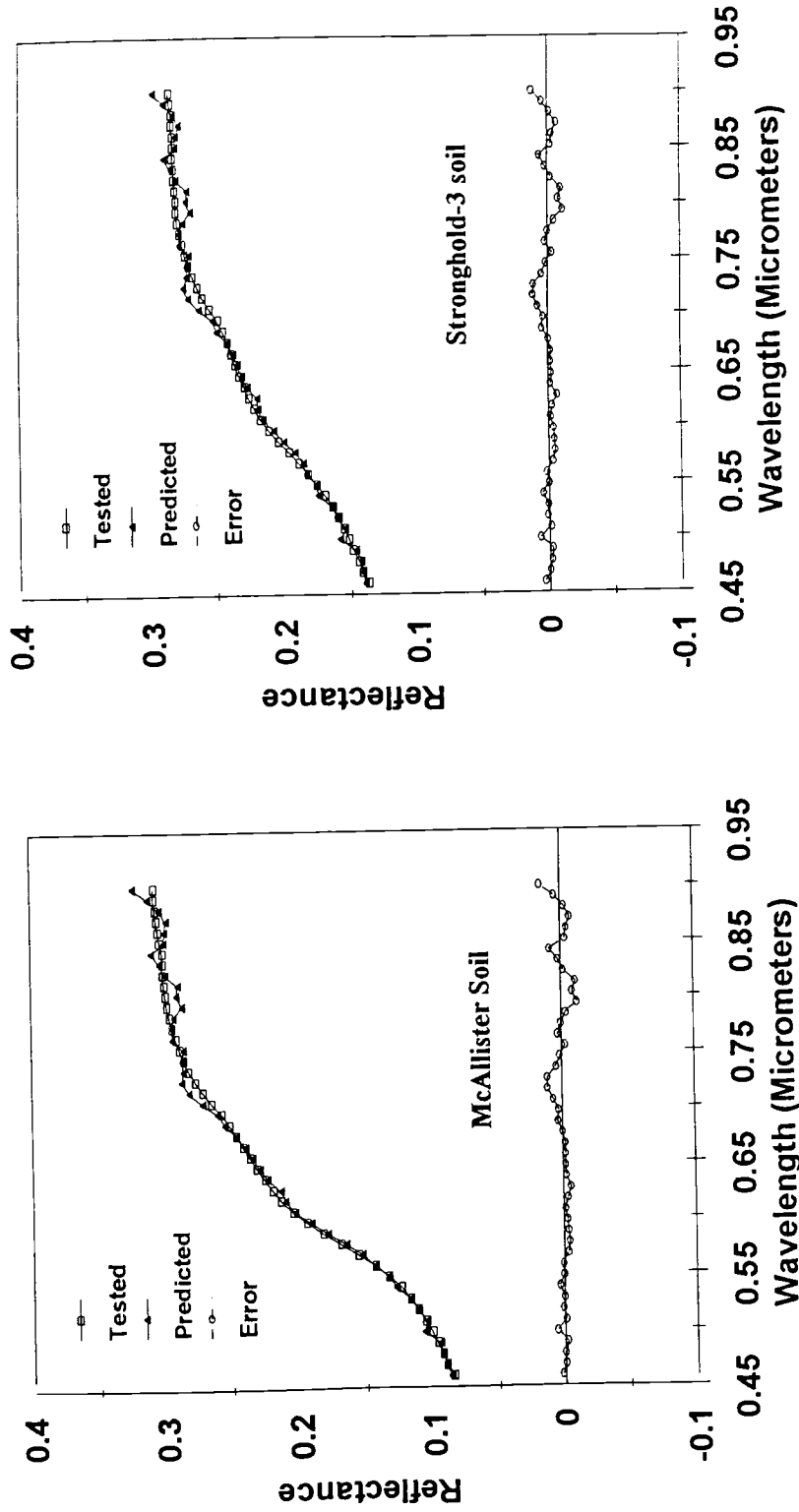


Figure 4-15 Target test results for McAllister and Stronghold-3 soils

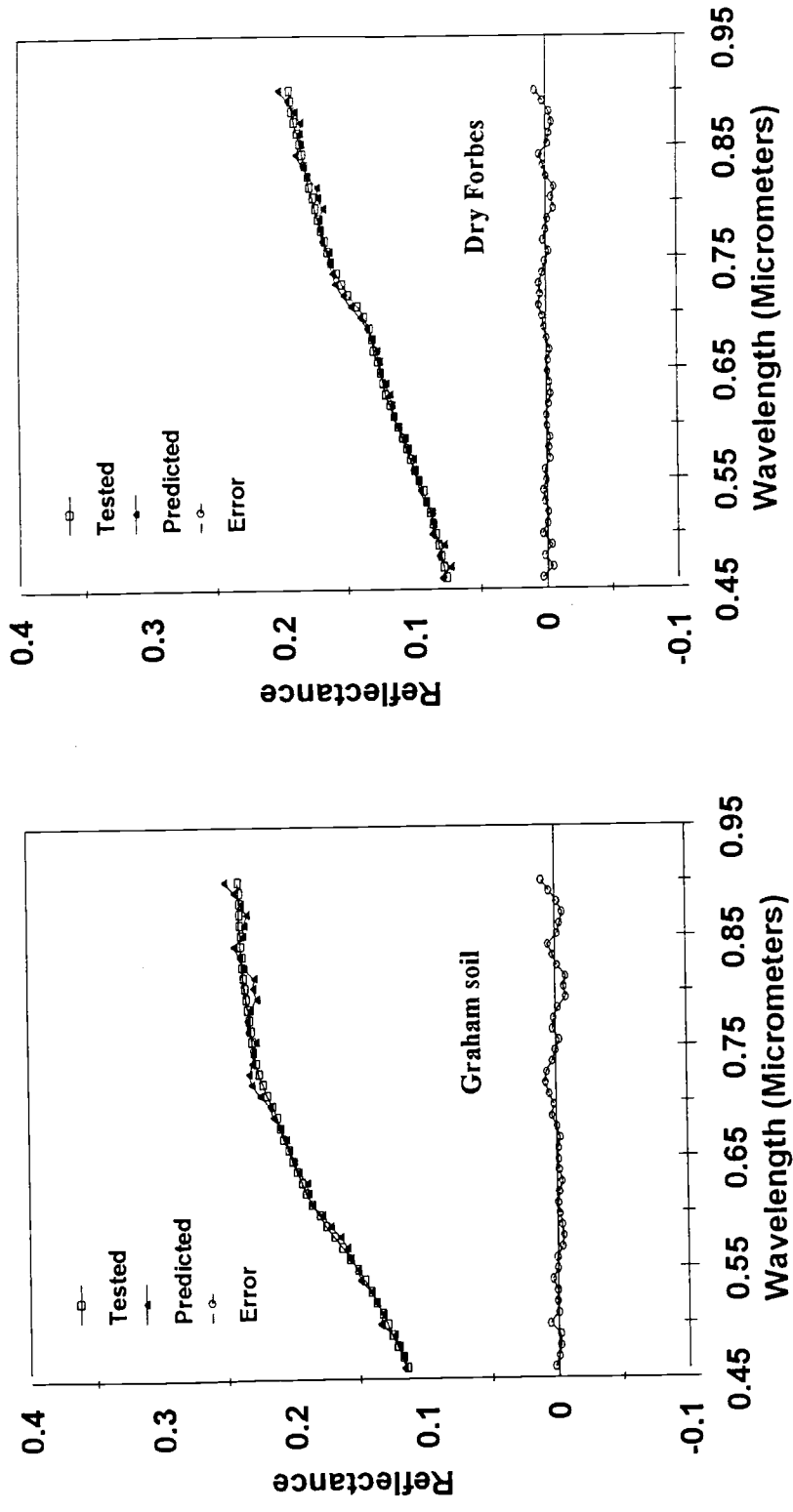


Figure 4-16 Target test results for Graham soil and dry forbes

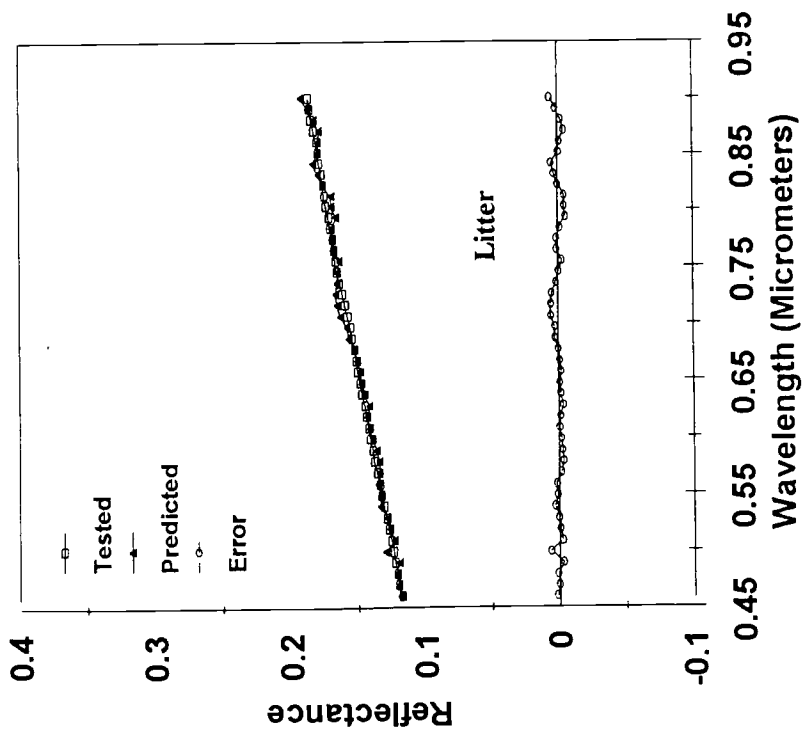
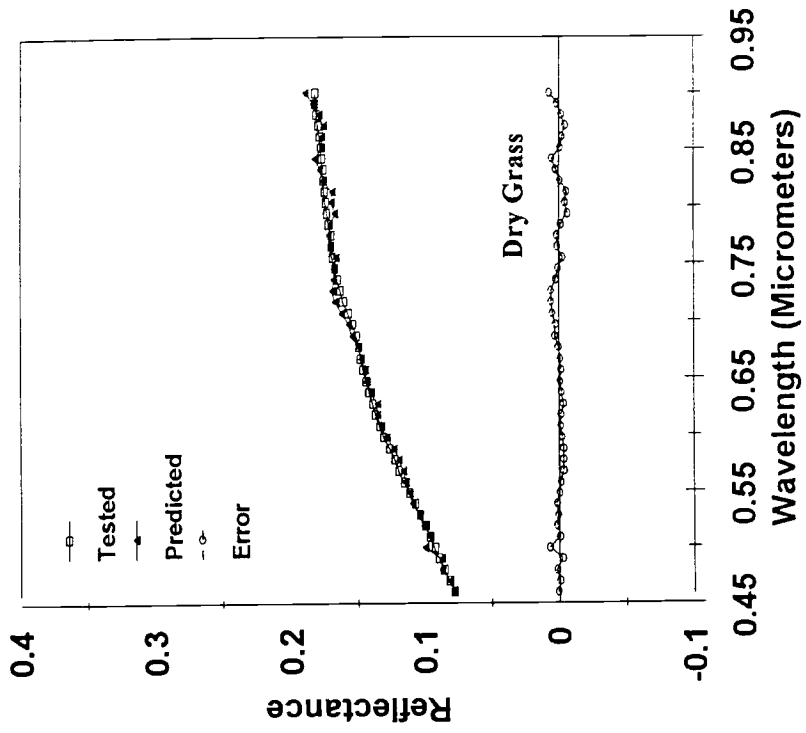


Figure 4-17 Target test results for litter and dry grass

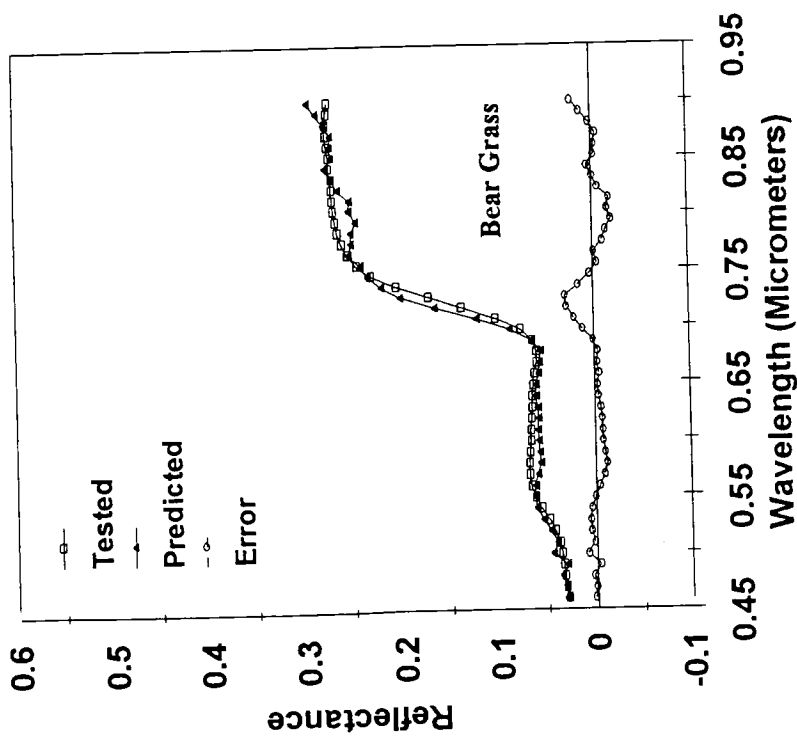
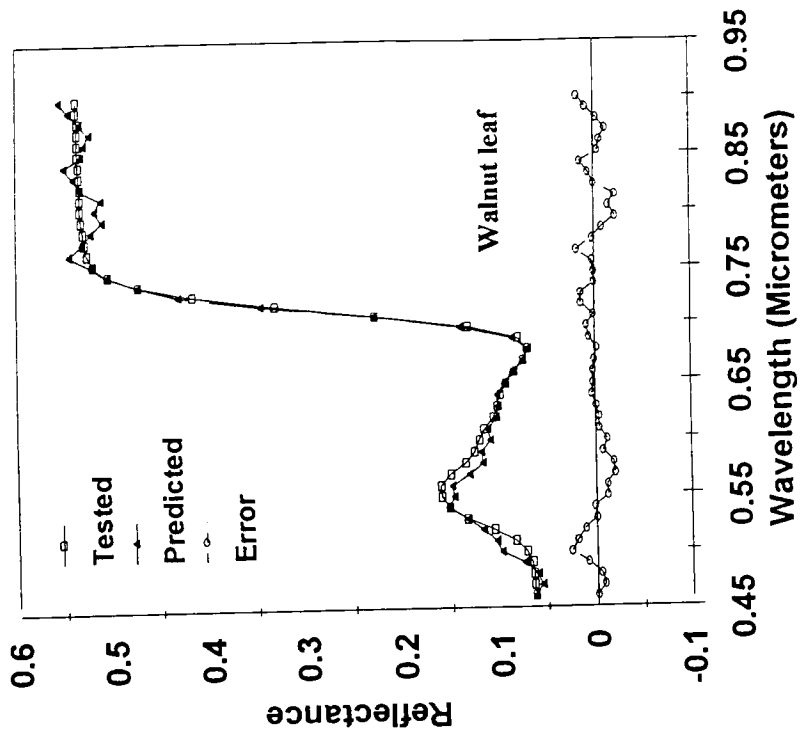


Figure 4-18 Target test results for bear grass and walnut leaf

For any of these materials the predicted spectra, as in the case of the test of soil reference endmembers, were affected by the uneven correction of the atmospheric effect by the ATREM radiative transfer code mostly in the NIR. The predicted spectra for dry forbes presented a higher percentage of error in the blue region of the spectrum than in other bands of the visible or in the near infrared region of the spectrum (Figure 4-16). The highest error represented 6% of the predicted reflectance values for the dry forbes and occurred at 0.469 μm . The behavior of the RMS error for the predicted spectra for litter and for dry grass is much like that found for the three soil reference endmembers with higher values in the water absorption bands and also a peak at 0.5 μm (ozone absorption band). For litter (Figure 4-17) the error reaches a maximum of 4.5% of the predicted reflectance at 0.5 μm while in the NIR region the error is about 3% of the predicted reflectance in the intervals between 0.71 and 0.73 μm , 0.79 and 0.81 μm and in the wavelength of 0.90 μm . The error for predicting the presence of dry grass as a reference endmember (Figure 4-17) was 7.2% of reflectance at 0.5 μm and between 3 and 4% for the intervals between 0.71 and 0.73 μm , 0.79 and 0.81 μm and in the wavelength of 0.90 μm .

Although green vegetation was assumed to be a pure image endmember, its physical meaning in terms of the identification of the type of green vegetation present in the AVIRIS scene of Walnut Gulch Experimental Watershed is important for the definition of the potential reference endmembers. Two common vegetation types that stay green during the warm summer in this Watershed is the Bear Grass (*Nolina microcarpa*) (which is present mainly in the Stronghold and Tombstone soil series) and the walnut tree (*Juglans major*) present in areas where there are some accumulation of water during part of the year. The field spectra

of Bear Grass was used as the target test for determining if this type of green vegetation represents a potential reference endmember in the AVIRIS image.

Figure 4-18 presents the results of applying the target test for Bear Grass. Although there is a general agreement between the tested field spectra and the predicted spectra using the target test, the error is still high for some of the 46 bands. Thus, in the visible region of the spectrum, the error is above 5% of the predicted reflectance for almost all the bands and reaches a peak at 0.5 μm with a value of 19% of reflectance. In the NIR region the error drops to values below 7% except for the interval between 0.70 μm and 0.73 μm where the differences between the predicted and the tested spectra are between 13 and 17% of the reflected energy. For the walnut tree the leaf spectra from the USGS spectral library (splib04c, spectrum ABSREF950) was used. Figure 4-18 shows how the predicted and the tested spectra for the walnut leaf matches. As in the case of the Bear grass the error is higher in the visible region of the spectra, with a maximum of 18% of the predicted reflectance for the 0.5 μm band. In the NIR, however, the predicted spectra of Walnut leaf present a good agreement with the tested spectra. Hence, for this region of the spectrum, the error does not exceed 4% of the predicted reflectance in any band.

The best fit presented by the Walnut leaf in the target tested model makes it the best candidate for the green vegetation reference endmember. Notice that, except for the green vegetation target, the best fit for the other targets were obtained using "pure" spectra collected in the field.

Spectral Decomposition of AVIRIS Data Using Reference Endmembers. The results of applying the target test on the AVIRIS image indicated that the number of reference endmember can be at least seven. These reference endmembers are: McAllister, Stronghold-3, and Graham soils, green vegetation (walnut leaf), litter, dry grass, and dry forbes. All these spectra were considered for the wavelength interval from 0.45 to 0.90 μm , and all came from the field except the spectra for the walnut leaf. The seven reference endmember spectra were used for modelling 46 bands of AVIRIS data in the interval from 0.45 to 0.90 μm . Spectral mixture analysis, however, could not be successfully applied to the combination of the seven reference endmembers. The model was then tested for a decreasing number of reference endmembers under different combinations. The models with more than three reference endmembers failed, and no output was obtained for the fractions of each reference endmember. Smith et al. (1994a, and 1994b) pointed out that the input of a high number of reference endmembers to equation 4.1 can result in an unstable solution for the fraction due to the loss of contrast between endmembers. Roberts et al. (1992) suggested the use of a subset of AVIRIS data in mixture analysis as one way to work with the high number of reference endmembers. Roberts et al. (1992) also utilized subsets of the AVIRIS image to optimize endmember detectability.

Figures 4-19 and Figure 4-20 present the fraction images for the best fit of the model for 3 reference endmembers. McAllister soil fraction image presented a relatively good agreement with the spatial distribution of this soil in the field (Figure 4-19a). When compared to the fraction image obtained using image endmembers (Figure 4-9a), the fraction image obtained using McAllister reference endmember was able to avoid misclassification with areas



(a)



(b)

Figure 4-19 Fraction images obtained using McAllister
(a) and Graham (b) reference endmembers



**Figure 4-20 Fraction image obtained using green
vegetation (Walnut leaf) reference
endmember**

occupied by Baboquivari soil series. On the other hand, the clear transition between McAllister and Graham soil that appear in the bottom of Figure 4-9a is taken place by a much more gradational transition in the McAllister reference endmember fraction image (Figure 4-19a).

Graham reference endmember fraction image (Figure 4-19b), however, shows great differences from what should be expected from field observations. Higher fractions of Graham are now located in areas occupied by Stronghold and Tombstone soils series while areas of Graham soil series and others, such as Epitaph and the Graham Lampshire soil series (that are spectrally similar to Graham) have relatively less of this reference endmember fractions. Figure 4-19b also shows that the shade effect present in the area with the fence (that can be seen clearly in top left of Figure 4-9b) disappear in the Graham reference endmember fraction image.

The green vegetation reference endmember (walnut leaf) fraction image (Figure 4-20) presents a good agreement with field observations. This kind of vegetation is found mostly in washes and other areas that tend to accumulate water during part of the year, such as ponds. Figure 4-20 also shows that the least green vegetation can be found in areas occupied by Graham and Graham rock outcrops soil series (dark areas in Figure 4-20).

Spectral Decomposition of Subsets of AVIRIS Data. Once it was discovered that the whole AVIRIS image of the Walnut Gulch Experimental Watershed could not be modeled by the entire set of reference endmembers detected by target test, the next alternative was to use the mixture analysis in a small set of pixels. Spectral decomposition using a subset of the original

AVIRIS data has been used by other authors (Robert et al., 1992) as a way of overcoming the need of a high number of endmembers to model complex scenes. In this study, the nine pixels used for each of the following image endmembers-McAllister, Stronghold-3, and Graham-were recomposed using the selected reference endmembers. The green vegetation image endmember was not modeled as a function of reference endmembers because it was considered a pure pixel and, as a result, it also can be considered reference endmembers. Although Graham/shade could not be spectrally separated from each other in the model using image endmembers, Graham soil was included in the model for spectral recomposition because of the abundance of other materials at the subpixel level (see Table 3-3).

Figures 4-21 through 4-23 present the results of applying spectral recomposition to McAllister, Stronghold-3, and Graham image endmembers, respectively. Notice that in any of the cases shown in these figures, the best fit does not include shade. The absence of shade in modelling image endmembers can be attributed to different reasons for each of the image endmembers. In the case of the McAllister image endmember, the low contrast between shade and liter reference endmember can justify the absence of shade in its spectral recomposition. Stronghold-3 image endmember has a very low level of green vegetation and the selected pixels have no influence from topographic shade. Thus, the shade fraction for this image endmember is below the level of the instrumental noise and, as a result, could not be detected. Finally, the low contrast between shade, volcanic rock and Graham justify the absence of the shade fraction in the Graham image endmember. In addition to these specific reasons, a general reason for the absence or low level of shade in image endmembers is the fact that in mixture analysis when selecting image endmembers, the search is for pixels with a minimum

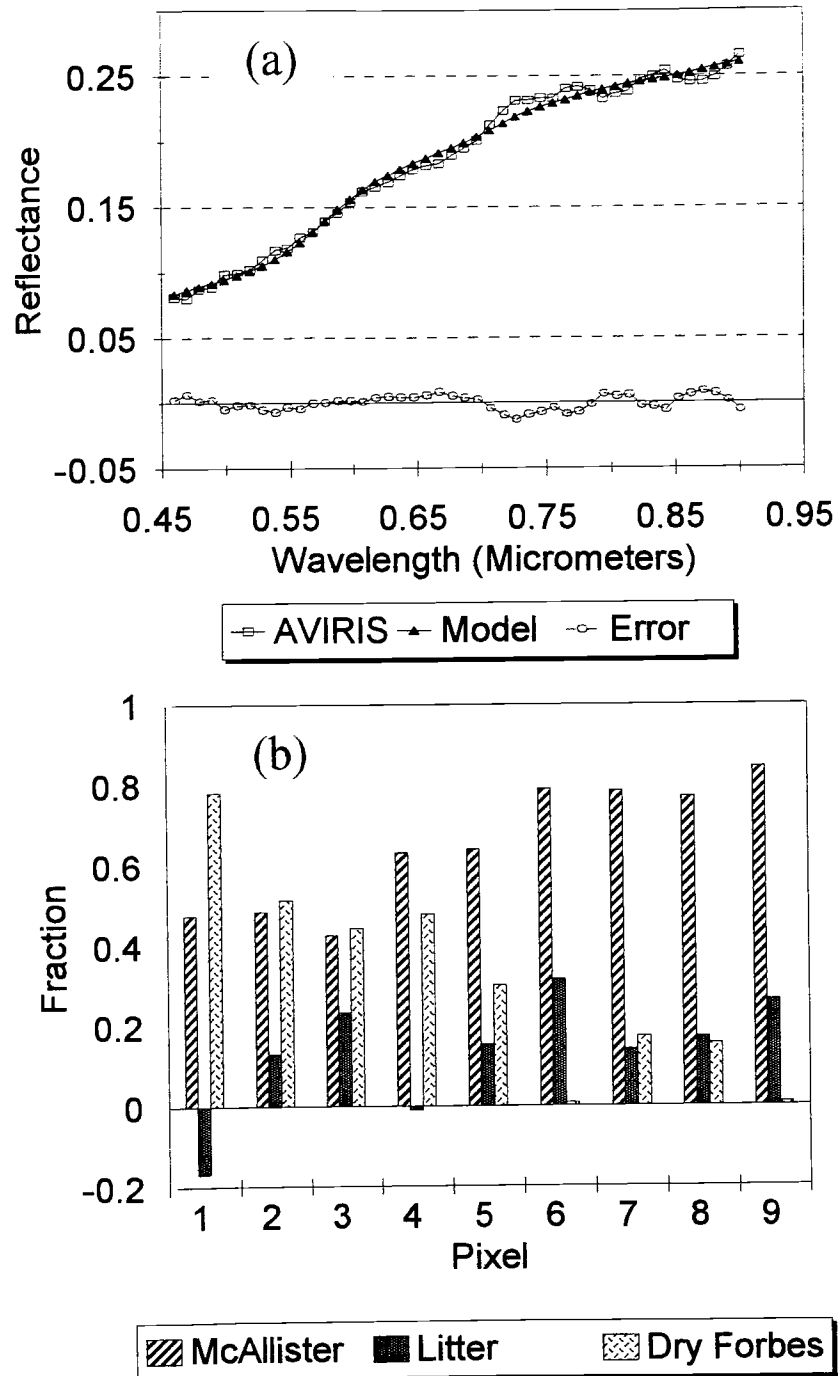


Figure 4-21 Spectral pixel recomposition (a) and reference endmember fractions (b)

for the subset of pixels used as McAllister image endmember

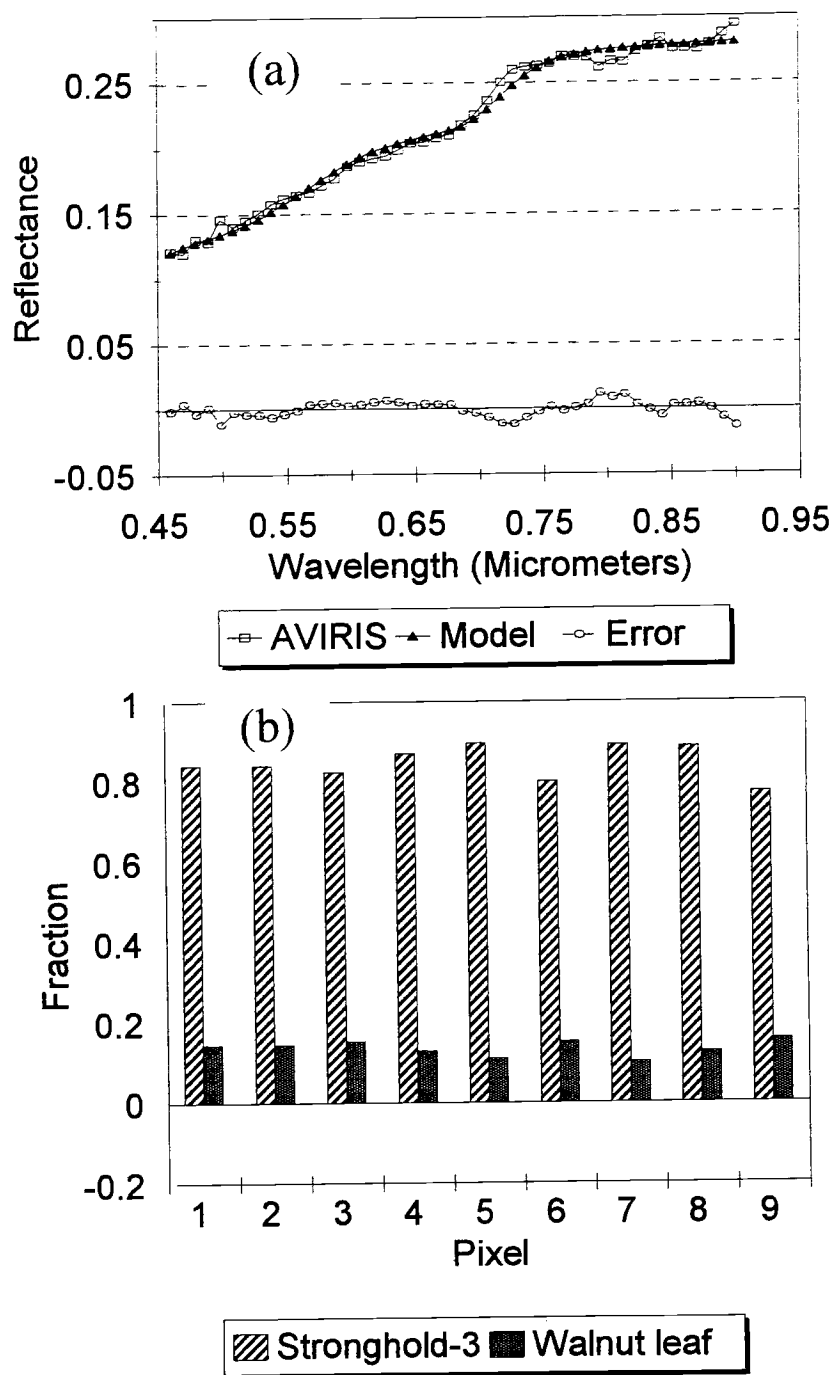


Figure 4-22 Spectral pixel recomposition (a) and reference endmember fractions (b) for the subset of pixels used as Stronghold-3 image endmember

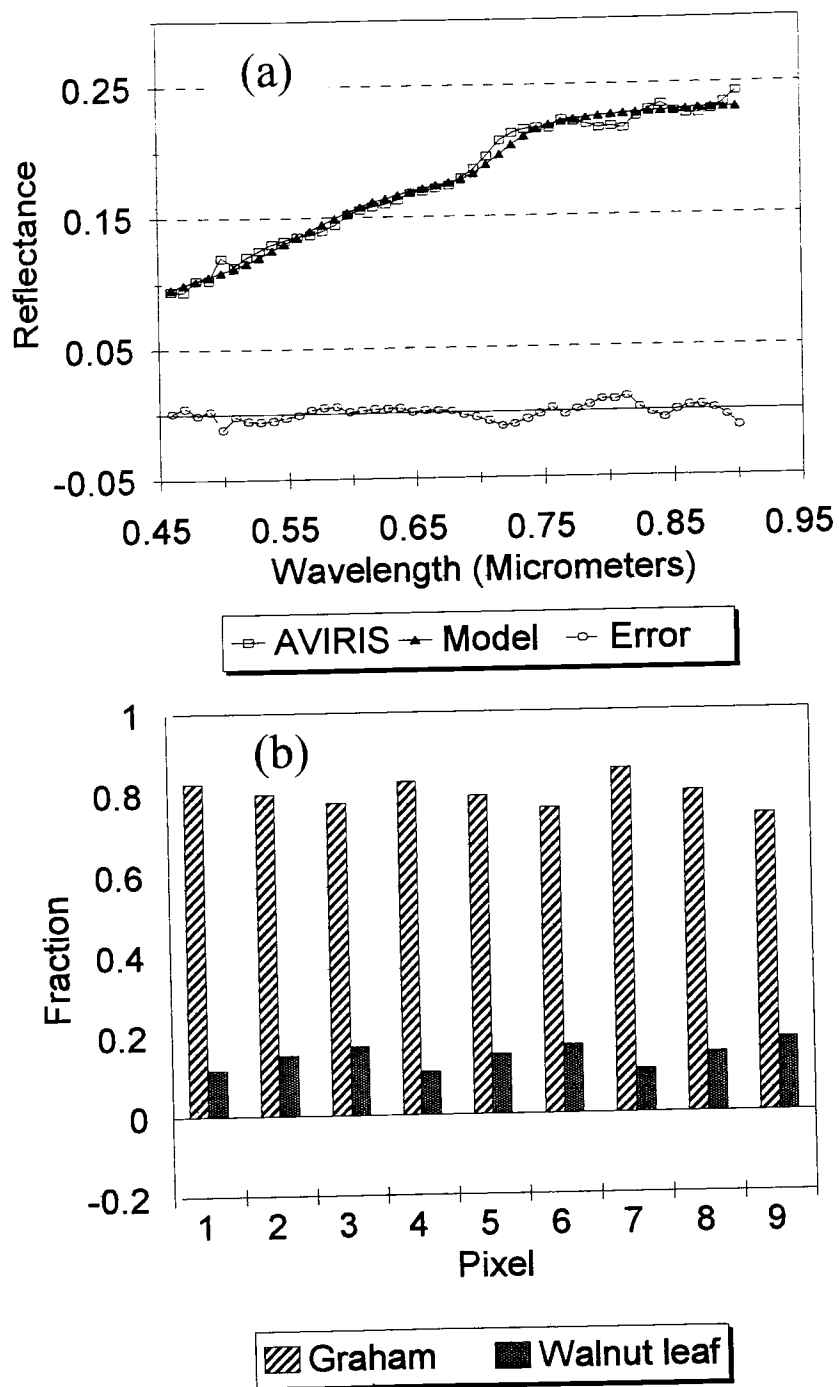


Figure 4-23 Spectral pixel recomposition (a) and reference endmember fractions (b) for the subset of pixels used as Graham image endmember

of shade contribution.

The general analysis of the residuals for the recomposition of the spectral curves of these three image endmembers shows that the error in the NIR region of the spectrum can be attributed to the uneven correction of the atmospheric effect and can be explained in the same way as for the target test in the previous section. The average rms error for the fit of the model for McAllister (which used in addition to this soil, the spectral signatures of litter, and dry forbes) is 0.005 or 2.6 % of the average AVIRIS reflectance for the nine pixels (Figure 4-21a). Proportionally, the error is higher in the visible than in the NIR region of the spectrum, with a maximum of 7.7% at 0.47 μm . The fractions or factor loadings of each reference endmember present in each of the pixels used as the McAllister image endmember is presented in Figure 4-21b. Although the model assumes that negative fractions are not allowed (because they have no physical meaning), the presence of negative fraction in some of the pixels of this image endmember could not be avoided. Hence, pixel one in Figure 4-21b presents a negative fraction out of the expected error for the litter reference endmember. For the remaining pixels, however, this three-reference-endmember model fits the constraints of positive fractions that sum to one within an expected 0.1 rms error.

Figure 4-22a shows the spectral recomposition of the averaged 9 pixels from the AVIRIS image for Stronghold-3 soil, using the field spectrum for this soil and a spectrum of a green leaf from a walnut tree. These two reference endmembers explained the fitness of the model within a rms error of 0.005 or 2.2% of the averaged AVIRIS spectra for Stronghold-3 image endmember. The highest error (8.2%) was found at 0.5 μm and can be attributed to the overcorrection of the ozone absorption band by the Atmospheric Removal

Program (ATREM). For the remaining bands the error is kept below 2% of the AVIRIS spectra except in the water absorption bands present in the interval between 0.7 and 0.9 μm . The analysis of the fractions shows that in any of the 9 pixels used as an image endmember the green vegetation contribution for the mixed spectra is less than 20% with a range of 10% to 15%. On the other hand the area occupied by Stronghold-3 soil in the image endmember pixels can represent as much as 90% of those pixels. The rms error for the fit of the fractions in the case of Stronghold-3 soil is below 5% for any one of the pixels.

The spectral recomposition of the Graham image endmember is shown in Figure 4-23a. Along with the field spectra of the Graham soil, the only reference endmember needed for recomposing the spectral curve of the Graham image endmember is the green vegetation reference endmember given by the walnut leaf spectra. The average rms error for the fit of these two reference endmembers for the recomposition of Graham image endmember is 0.004 or 0.4% of reflectance which also represents 2.4% of the average spectral response of the Graham image endmember. As in the case of the other two image endmembers, the uneven correction of the atmospheric effect by ATREM was responsible for the highest values for the rms error. Hence the rms represents 10% of the measured spectra in 0.5 μm while in the interval between 0.70 and 0.73 μm the rms error varied between 3.0 and 5.5% of the measured spectra.

Figure 4-23b presents the distribution of the Graham soil and green vegetation reference endmembers for the composite spectra of each pixel used as Graham image endmember. Graham soil fraction varied from 74% to 86 % of the area of each pixel while green vegetation endmember represents a range from 10.5% to 18 % for the nine pixels used

as the Graham image endmember. The high contrast between Graham soil and the green vegetation reference endmembers can explain why fractions of green vegetation as low as 10% can be detected using mixture analysis. The detection of very small amounts of green vegetation by mixture analysis make this technique particularly useful for monitoring changes in areas of sparse green vegetation, such as in semi arid environments. As indicated by Huete (1987), green vegetation indices are particularly affected by soil background spectral responses and by the percent of green cover. Vegetation indices from areas with less than 20% green cover have been reported as unreliable.

Conclusions

The spectral and spatial variability of the AVIRIS data from the Walnut Gulch Experimental Watershed was explained by four component images or four image endmembers.

The best fit for spectral mixture analysis was found for the following image endmembers: McAllister soil, Stronghold-3 soil, Graham soil, and green vegetation.

Graham soil, Epitaph, volcanic rock, and shade image endmembers were not separated from each other on the basis of their spectral response. However, the shade image endmember were separated from other dark features on the basis of the spatial context.

Soil spectral maps for the AVIRIS scene of Walnut Gulch Experimental Watershed were derived through spectral mixture analysis on the basis of spectra extracted from its own image.

On the basis of image endmembers and spatial context, three soil spectral classes (McAllister, Stronghold-3, and Graham) were distinguished from other scene components by using spectral mixture analysis.

The target test showed that there were at least seven reference endmembers in AVIRIS image. The reference endmembers detected by target test were: McAllister, Stronghold-3, and Graham soils, dry forbes, litter, dry grass and green vegetation (walnut). Spectral mixture analysis, however, could not be run for these sets of reference endmembers.

Mixture analysis on the basis of the reference endmember was applied only for a set of three reference endmembers: McAllister soil, Graham soil, and walnut leaf. The fraction images produced with these three reference endmembers, however, presented departures from the ground truth with most of the error concentrated in the Graham spectral map.

Spectral mixture analysis, when applied to a subset of pixel, detected the presence and estimated the fractions of six of the seven reference endmembers identified using target test. Thus, soil image endmember spectra were reconstructed on the basis of the reference spectra of each material present in each subset of the AVIRIS scene.

CHAPTER 5

SUMMARY AND CONCLUSIONS

As a main reservoir of water and nutrients not only for growing small organisms but also several terrestrial ecosystems, the soil system is seen as an important component in the process of global change. In this context the role of remote sensing in mapping and monitoring soil, either in terms of anthropogenic or natural transformations, has vital importance. Remote sensing can only be helpful, however, if soil spectral properties can be well characterized for different soil conditions, different viewing/source of illumination geometry, different scales, and different types of remote sensors, which include many narrow bands in the solar reflective spectrum. Without this characterization the results presented by new technologies in image classification, such as mixture analysis, will be misinterpreted. Thus, in this study it was proposed (Chapter 2) to characterize the BRF behavior of eight soils from the Walnut Gulch Experimental Watershed in relation to different wet and rough conditions and view/source of illumination geometry in the optical region of the electromagnetic spectrum.

Chapter 3 added to the information obtained in Chapter 2 the soil spectra from AVIRIS scene with the objectives of comparing the spectral information content for different sensor scales. In addition to that, in Chapter 3 the dimensionality of soil spectra in terms of spectral classes for different soil conditions and different viewing/source of illumination geometry was explored and, it was determined the dimensionality of soil spectra in terms of

main bands need to characterize the soil spectra obtained under lab conditions. In Chapter 4 the generated soil spectral library as well other non soil spectra from the area of the Walnut Gulch Experimental Watershed imaged by AVIRIS and from other sources were used to model the entire image using mixture modeling. Thus, the main objective of Chapter 4 was to generate a soil spectral map of this Watershed.

The soils present in the AVIRIS scene of the Walnut Gulch Experimental Watershed presented anisotropic behavior which is also dependent on soil wetness and surface roughness conditions. The anisotropic behavior of these soils, however, varied inversely with the wavelength, with spectral response in the blue region showing the most anisotropic behavior and the spectral response in the middle infrared, showing the least. The contrast between rocks and soil background affected the anisotropic behavior of soil surfaces present in the AVIRIS scene of Walnut Gulch Experimental Watershed.

In addition to the inherent spectral behavior of soil samples under ground or lab condition (which varied with the factors pointed out), comparison of these soil spectra with soil spectra extracted from the AVIRIS scene showed different information content. Scale and calibration (atmospheric corrected versus apparent reflectance) issues arise as potential sources of the differences in extracting information for the different sensors and conditions utilized in the Walnut Gulch Experimental Watershed. Loss of soil information occurred (even using techniques that are able to detect small absorption feature, such as the first derivative) when moving from a large scale data set (RELAB, sieved sample, and field spectra) to a small scale data set (AVIRIS). As a result of scale effects, soil conditions (wet or dry), and viewing angles, soil spectral classes were different whether the spectral

information content came from lab, field or AVIRIS imagery.

Factor analysis showed that with four unique bands (located at 0.410, 1.310, 0.650, and 2.400 μm), it was possible to reconstruct the four basic soil spectral curves (Epitaph, Graham, McAllister, and Baboquivari) from RELAB data set. The same four was found for the number of component images needed to explain the variation of the AVIRIS data set. The spatial meaning of this dimensionality was explained by using the following image endmembers in the mixture model: McAllister soil, Stronghold-3 soil, Graham soil, and green vegetation.

Low spectral contrast prevented the separation of the shade endmember from other dark soil surfaces, such as Graham and Epitaph soil series. Those soil series, however, was separated from the shade endmember on the basis of the spatial context. Although spectral maps were derived for the AVIRIS scene of the Walnut Gulch Experimental Watershed on the basis of image endmembers due to the scene complexity, the mixture analysis failed in modeling this scene on the basis of the seven reference endmembers detected by the target test. The model run for the three reference endmembers (McAllister, Graham, and Walnut leaf spectra) and the results, particularly for Graham reference endmembers, did not match with field observations.

Subsets of the AVIRIS image were modeled using reference endmembers. In this case, the target test proposed by Malinowski and Howery (1980) proved to be useful in detecting potential reference endmembers. With the mixture analysis, it was possible to model the image endmember spectral responses on the basis of the best candidates for reference endmembers.

APPENDIX A:
ATREM'S INPUT CARD

Table A1. Details of the input card for the ATREM radiative transfer code

Input	Comment
05 14 1991 17 27 08	Date and time (month, day, year, hour, minute, seconds)
31 40 20	Latitude (degrees, minutes, seconds)
N	Hemisphere of the Earth
110 07 00	Longitude (degrees, minutes, seconds)
W	Hemisphere of the Earth (E or W)
9.	Average spectral resolution (nm) of AVIRIS data
aviris_full.wv	Wavelength file (λ in units of μm)
0	Channel ratio parameters (default for soil, rocks and minerals)
2	Atmospheric model number (mid latitude summer)
1 1 1 1 1 1 1	Gas selectors (include H ₂ O, CO ₂ , O ₃ , NO, CO, CH ₄ , and O ₂)
0.34	Total column ozone amount (atm-cm)
1 50	Aerosol model (continental), visibility (50 km)
1.5	Average elevation of the surface scene (1.5 km)
aviris.cub	Input AVIRIS data (224 channels)
1	Input AVIRIS data dimensions in the next line
0 512 410 224 0	The dimensions should be read from header, number of samples (512), number of lines (410), number of channels (224), band sequential
aviris_refl.cub	Output reflectance file (data is reflectance values times 1000)
10.	Output data resolution (nm)
aviris.vap	Output water vapor file (data in units of 1000 x cm)
transm.lib	Output library file containing gaseous transmittance spectra

APPENDIX B:
PICTURE OF THE LANDSCAPE AND DETAILS OF THE SOIL SURFACE OF THE
MCALLISTER SOIL SERIES



Figure B1. Landscape of the McAllister soil series



Figure B2. Details of the surface of the McAllister soil series

APPENDIX C:
PICTURE OF THE LANDSCAPE AND DETAILS OF THE SOIL SURFACE OF THE
STRONGHOLD SOIL SERIES



Figure C1. Landscape of the Stronghold soil series



Figure C2. Details of the surface of the Stronghold soil series

APPENDIX D:
PICTURE OF THE LANDSCAPE AND DETAILS OF THE SOIL SURFACE OF THE
GRAHAM SOIL SERIES



Figure D1. Picture of the landscape and details of the soil surface of the Graham soil series

LIST OF REFERENCES

- Adams, J.B., M.O. Smith, and A.R. Gillespie. 1993. Imaging spectroscopy: Interpretation based on spectral mixture analysis. p. 145-166. *In* Pieters, C.M. and P.A.J. Englert (ed.) Remote geochemical analysis: Elemental and mineralogical composition. Cambridge University Press.
- Adams, J.B., M.O. Smith, and A.R. Gillespie. 1989. Simple models for complex natural surfaces: A strategy for the hyperspectral era of remote sensing. p. 16-21. *In* Proceedings of IGARSS, Vancouver, Canada. 10-14 July 1989.
- Agbu, P.A., D.J.Fehrenbacher, and I.J. Jansen. 1990. Statistical comparison of SPOT spectral maps with field maps. *Soil Sci. Soc. Am. J.* 54:812-818.
- Ambrosia, V.G, J.S. Myers, T. Bobble, and P. Ishikawa. 1991. Sierra Nevada forest stress determination from AVIRIS data. p. 73 - 79. *In* R.O. Green (ed.) Proc. 3rd Airborne Visible/Infrared Imaging Spectrometer (AVIRIS) Workshop, JPL Publication 90-54, Jet Propulsion Laboratory, Pasadena, CA.
- Ball, G.H. 1971. Classification Analysis. Stanford Research Institute. SRI Project 5533.
- Baumgardner, M.F., L.F. Silva, L.L. Biehl, and E.R. Stoner. 1985. Reflectance properties of soils. p. 1-44. *In* N.C. Brady (ed). *Advances in Agronomy*. Academic Press Inc, Orlando-Fl.
- Berk, A., L.S. Bernstein, and D.C. Roberson. 1989. MODTRAN: A moderate Resolution Model for LOWTRAN 7. U.S. Air Force Geophysical Laboratory (AFGL), Hanscom Air Force Base, Massachusetts.
- Bigham, J.M., D.C. Golden, S.W. Buol, S.B. Weed, and L.H. Bowen. 1978. Iron oxides mineralogy of well-drained Ultisols and Oxisols: 2. Influence on color, surface area, and phosphate retention. *Soil Sci. Soc. Am. J.* 42:825-830.
- Bowers, S.A., and R.J. Hanks. 1965. Reflection of radiant energy from soils. *Soil Science*, 100:130-138.
- Breckenfeld, D.H. 1995. Soil survey of Walnut Gulch Experimental Watershed, Arizona. Soil Conservation Service, USDA. 130 pp.
- Brink, R.A., J.W. Densmore, and G.A. Hill. 1977. Soil deterioration and the growing demand for food. *Science* 197:625-629.

- Cahill, J.E. 1979. Derivative spectroscopy: understanding its application. *Am. Lab.* 1979:79-85.
- Card, D.H., D.L. Peterson, P.A. Matson, and J.D. Aber. 1988. Prediction of leaf chemistry by the use of visible and near infrared reflectance spectroscopy. *Remote Sens. Environ.* 26:123-147.
- Chen, Z., and Elvidge, C.D. 1993. Description of derivative-based high spectral-resolution (AVIRIS) green vegetation index. p. 43-48. *In* Vane, G. (ed.) *Imaging Spectrometry of the Terrestrial Environment*. Proceedings of The International Society for Optical Engineering (SPIE), Orlando, Fl. 14-15 April 1993.
- Chen, Z., Curran, P.J., and Hansom, J.D. 1992. Derivative reflectance spectroscopy to estimate suspended sediment concentration. *Remote Sens. Environ.* 44:67-77.
- Cihlar, J., and R. Protz. 1973. Surface characteristics of mapping units related to aerial imaging of soils. *Can. J. Soil Sci.* 53:249-257.
- Cipra, J.E., M.F. Baumgardner, E.R. Stoner, and R.B. MacDonald. 1971. Measuring radiance characteristics of soil with a field spectroradiometer. *Soil Sci. Soc. Am. Proc.* 35:955-966.
- Condit, H.R. 1972. Application of characteristic vector analysis to the spectral energy distribution of daylight and the spectral reflectance of American soils. *Appl. Opt.* 11:74-86.
- Coulson, K.L. 1966. Effects of reflection properties of natural surfaces in aerial reconnaissance. *Appl. Opt.* 5:905-917.
- Coulson, K.L., and D.W. Reynolds. 1971. The spectral reflectance of natural surfaces. *J. Appl. Meteorol.* 10:1285-1295.
- Coulson, K.L., G.M. Bouricius, and E.L. Gray. 1965. Optical reflection properties of natural surfaces. *J. Geophys. Res.* 70:4601-4611.
- Curran, P.J. 1994. Imaging spectrometry - its present and future role in environmental research. p.1-23. *In* J. Hill and J. Megier (ed.) *Imaging spectrometry - a tool for environmental observations*. Kluwer Academic Publishers, Dordrecht, The Netherlands.
- Curran, P.J. and J.A. Kupiec. 1995. Imaging spectrometry: A new tool for ecology. p. 71-88. *In* F.M. Danson and S.E. Plummer (ed.). *Advances in environmental remote sensing*. John Wiley & Sons, New York.

- Curran, P.J., G.M. Foody, K. Ya. Kondratyev, V.V. Kozoderov, and P.P. Fedchenko. 1990. Remote Sensing of Soils and Vegetation in the USSR. Taylor & Francis, London.
- Deering, D.W. 1989. Field measurements of bidirectional reflectance. p. 14-65. In G. Asrar (ed.). Theory and applications of optical remote sensing. John Wiley & Sons, New York.
- Demetriades-Shah, T.H., M.D. Steve, and J.A. Clark 1990. High resolution derivative spectra in remote sensing. *Remote Sens. Environ.* 33:55-64.
- Derek, R.P., G.H. Hall, and F.L. Ellsworth. 1996. A comparison of NDVI and spectral mixture analysis for estimating biophysical properties in boreal forest terrain. p. 230-232. *In* Proceedings of IGARSS, Lincoln, Neb. 27-31 May 1996.
- Dillon, W.R., and Goldstein, M. 1984. *Multivariate Analysis - Methods and Applications*. John Wiley & Sons, New York.
- Eaton, F.D., and I. Dirmhirn. 1979. Reflected irradiance indicatrices of natural surfaces and their effect on albedo. *Applied Optics*, 18:995-1008.
- Epiphanyo, J.C.N., A.R. Formaggio, M.M. Valeriano, and J.B. Oliveira. 1992. Spectral behavior of the soils of Sao Paulo State (in portuguese). Instituto Nacional de Pesquisas Espaciais, Sao Paulo, Brazil. INPE publication 5424-PRP/172.
- Escadafal, R. 1994. Soil spectral properties and their relationships with environmental parameters - examples from arid regions. p. 71-87. *In* J. Hill and J. Megier (ed.) *Imaging spectrometry - a tool for environmental observations*. Kluwer Academic Publishers, Dordrecht, The Netherlands.
- Everitt, B. 1980. *Cluster Analysis*. 2nd Edition. Heineman Educational Books Ltd, London.
- Fernandes, R., J.R. Miller, and L.E. Band. 1996. Comparison of linear least squares unmixing methods and gaussian maximum likelihood classification. p. 420-422. *In* Proceedings of IGARSS, Lincoln, Neb. 27-31 May 1996.
- Farrand, W.H., R.B. Singer, and E. Merenyi. 1994. Retrieval of aparent surface reflectance from AVIRIS data: A comparison of empirical line, radiative transfer, and spectral mixture methods. *Remote Sens. Environ.* 47:311-321.

- Foschi, P.G. 1994. A geometric approach to a mixed pixel problem: Detecting subpixel woody vegetation. *Remote Sens. Environ.* 50:317-327.
- Gamon, J.A., D.A. Roberts, and R.O. Green. 1995. Evaluation of the photochemical reflectance index in AVIRIS imagery. p. 55-58. *In* R.O. Green (ed.) *Summaries of the Fifth Annual JPL Airborne Earth Science Workshop. Vol. 1 AVIRIS Workshop JPL Publication 95-1, Jet Propulsion Laboratory, Pasadena, CA*
- Gao, B.C., and A.F.H. Goetz. 1990. Column atmospheric water vapor and vegetation liquid water retrievals from airborne imaging spectrometer data. *J. Geophys. Res.*, 95:3549-3564.
- Gao, B.C., K.B. Heidebrecht, and A.F.H. Goetz. 1996. *Atmospheric Removal Program (ATREM) Users Guide, Centre for the Study of Earth from Space, Cooperative Institute for Research in Environmental Sciences, University of Colorado, Boulder.*
- Gelderman, F.W. 1970. *Soil Survey of Walnut Gulch Experimental Watershed, Arizona. A special report. United State Department of Agriculture. Soil Conservation Service. 55 pp.*
- Goodin, D.G. and G.M. Henebry. 1996. Seasonal NDVI trajectories in response to disturbance: Toward a spectral-temporal mixing model for tallgrass prairie. p. 215-217. *In Proceedings of IGARSS, Lincoln, Neb. 27-31 May 1996.*
- Goetz, A.F.H. 1992. Principles of narrow band spectrometry in the visible and IR: Instruments and data analysis. *In: Toselli, F., and Bodechtel, J. Imaging Spectroscopy: Fundamentals and Prospective Applications. Kluwer Academic Publishers*
- Goetz, A.F.H., and Boardman, J.W. 1989. Quantitative determination of imaging spectrometer specifications based on spectral mixing models. p. 1036-1039. *In Proceedings of IGARSS, Vancouver, Canada. 10-14 July 1989.*
- Goetz, A.F.H., Vane, G., Solomon, J.E., and Rock, B.N. 1985. Imaging spectrometry for Earth remote sensing. *Science* 228:1147-1153.
- Hlavka, C.A., and Spanner, M.A. 1995. Unmixing AVHRR imagery to access clearcuts and forest regrowth in Oregon. *IEEE Transactions on Geoscience and Remote Sensing* 33:788-795.
- Horwitz, H.M., Halepka, R.F., Hyde, P.D., and Morgenstern, J.P. 1971. Estimating the proportions of objects within a single resolution element of a multispectral scanner. p. 1307-1320. *In Proceedings of 7th International Symposium on Remote*

Sensing of Environment. Ann.Arbor, MI, Environmental Research Institute of Michigan.

- Hoffer, R.M., and C.J. Johannsen. 1969. Ecological potentials in spectral signature analysis. p.1-19. *In* Johnson, P.L. (ed.) Remote sensing in ecology. University of Georgia Press, Athens.
- Huete, A.R. 1996. Extension of soil spectra to the satellite: Atmosphere, geometric, and sensor considerations. *Photo-Interpretation* 2:101-114.
- Huete, A.R. 1987. Soil influences in remotely sensed vegetation-canopy spectra.p. 107-141. *In* Asrar, G. (ed.) Theory and Applications of Optical Remote Sensing. John Wiley & Sons, NY.
- Huete, A.R. 1986. Separation of soil-plant spectral mixtures by factor analysis. *Remote Sen. Environ.* 19:237-251.
- Huete, A.R. and Escadafal, R. 1991. Assessment of biophysical soil properties through spectral decomposition techniques. *Remote Sen. Environ.* 35:149-159.
- Huete, A.R., R.D. Jackson, and D.F. Post. 1985. Spectral response of a plant canopy with different soil backgrounds. *Remote Sens. Environ.* 17:37-53.
- Huang, C., and J.M. Bradford. 1990. Portable laser scanner for measuring soil surface roughness. *Soil Sci. Soc. Am. J.* 54:1402-1406.
- Irons, J.R., K.J. Ranson, D.L. Williams, and R.R. Irish. 1991. An off-nadir-pointing imaging spectroradiometer for terrestrial ecosystem studies. *IEEE Transactions on Geoscience and Remote Sensing.* 29:66-74.
- Irons, J.R., and J.A. Smith. 1990. Soil surface roughness characterization from light scattering observations. p. 1007-1010. *In* Proceedings of IGARSS, Washington, DC. 20-24 May 1990.
- Irons, J.R., R.A. Weismiller, G.W. Petersen.1987. Soil Reflectance. p. 66-106. *In* Asrar, G. (ed.) Theory and Applications of Optical Remote Sensing. John Wiley & Sons, NY.
- Jackson, R.D., P.M. Teillet, P.N. Slater, G. Fedosejevs, M.F. Jasinski, J.K. Aase, and M.S. Moran.1990. Bidirectional measurements of surface reflectance for view angle corrections of oblique imagery. *Remote Sens. Environ.* 32:189-202.

- Jenny, H. 1980. The Soil Resource - Origin and Behavior. Series ecological studies, 37. Springer-Verlag, N.Y.
- Johnson P.E., Smith M.O., and Adams B. 1992. Simple algorithms for remote determination of mineral abundances and particle sizes from reflectance spectra. *J. Geophys. Res.* 97:2649-2657.
- Johnson P.E., Smith M.O., Taylor-George S., and Adams J.B. 1983. A semiempirical method for analysis of the reflectance spectra of binary mineral mixtures. *J. Geophys. Res.* 88:3557-3561.
- Kimes, D.S. 1983. Dynamics of directional reflectance factor distributions for vegetation canopies. *Appl. Opt.* 22:1364-1372.
- Kimes, D.S. and P.J. Sellers 1985 Inferring hemispherical reflectance of the earth's surface for global energy budgets from remotely sensed nadir or directional radiance values. *Remote Sen. Environ.* 18:205-223.
- Kimes, D.S., W.W. Newcomb, C.J. Tucker, I. S. Zonneveld, W. Van Wijngaarden, J. De Leeuw, and G.F. Epema. 1985. Directional reflectance factor distributions for cover types of northern Africa. *Remote Sen. Environ.* 18:1-19.
- Kimes, D.S., B.N. Holben, and C.J. Tucker. 1984. Optimal directional view angles for remote-sensing missions. *Int. J. Remote Sensing*, 5:887-908.
- Kosmas, C.S., N.Curi., R.B. Bryant, and D.P. Franzmeier. 1984. Characterization of iron oxide minerals by second-derivative visible spectroscopy. *Soil Sci. Soc. Am. J.* 48:401-405.
- Kristof, S.J., and A.L. Zachary. 1971. Soil types from multispectral scanner data. *Proc. 7th. Int. Symp. Remote Sens. Environ.*, University of Michigan, Ann Arbor. 1427-1434.
- Kruse, F.A. and W.M. Calvin, 1988. Automated extraction of absorption features from Airborne Visible/Infrared Imaging Spectrometer (AVIRIS) and Geophysical and Environmental Research Imaging Spectrometer (GERIS) data. p. 62-71. *In* G. Vane (ed.) *Proc. of Airborne Visible/Infrared Imaging Spectrometer (AVIRIS) Performance Evaluation Workshop JPL Publication 88-38*, Jet Propulsion Laboratory, Pasadena, CA.
- Lal, R. and B.A. Stewart. 1992. Need for Land Restoration. P. 1-11. *In* Lal, R. and B.A. Stewart (ed.) *Advances in Soil Science. Vol. 17.* Springer-Verlag, NY.

- Malinowski, E.R. 1991. Factor analysis in chemistry. 2nd ed. John Wiley & Sons, New York, NY.
- Malinowski, E.R. 1982. Obtaining the key set of typical vectors by factor analysis and subsequent isolation of component spectra. *Analytica Chimica Acta*, 134:129-137.
- Malinowski, E.R., and Howery, D.G. 1980. Factor analysis in chemistry. John Wiley & Sons, New York, NY.
- Malkmus, W. 1967. Random Lorentz band model with exponential-tailed S line intensity distribution function, *J. Opt. Soc. Am.* 57:323-329.
- Marsh, S.E., P. Switzer, W.S. Kowalik, and R.J.P. Lyon. 1980. Resolving the percentage of component terrains within single resolution elements. *Photogramm. Eng. Remote Sens.* 46:1079-1086.
- May, G.A., and G.W. Petersen. 1975. Spectral signature selection for mapping unirrigated soils. *Remote Sens. Environ.* 4:211-220.
- Milton, E.J. 1987. Principles of field spectroscopy. *Int. J. Remote Sensing*, 8:1807-1827.
- Milton, E.J., E.M. Rollin, and D.R. Emery. 1995. Advances in field spectroscopy. p. 9-32. *In* F.M. Danson and S.E. Plummer (ed.). *Advances in environmental remote sensing*. John Wiley & Sons, New York.
- Moran, M.S., R.D. Jackson, P.N. Slater, and P.M. Teillet, 1992. Evaluation of simplified procedures for retrieval of land surface reflectance factors from satellite sensor output. *Remote Sens. Environ.* 41:169-184.
- Moran, M.S., R.D. Jackson, G.F. Hart, P.N. Slater, R.J. Bartell, S.F. Biggar, D.I. Gellmand, and R.P. Santer. 1990. Obtaining surface reflectance factors from atmospheric and view angle corrected SPOT-1 HRV data. *Remote Sens. Environ.* 32:203-214.
- Munsell Color Company. 1975. Munsell soil color charts. Munsell Color, Baltimore, Md.
- Norris, K.H., R.F. Barnes, J.E. Moore, and J.S. Shenk. 1976. Predicting forage quality by infrared reflectance spectroscopy. *Journal of Animal Science*, 43:889-897.
- Parks, J.M. 1966. Cluster analysis applied to multivariate geologic problems. *J. Geol.* 74:703-715.

- Peterson, D.L., Aber, J.D., Matson, P.A., et al. 1988. Remote sensing of forest canopy and leaf biochemical content. *Remote Sens. Environ.* 24:85-108.
- Planet, W.G. 1970. Some comments on reflectance measurements of wet soils. *Remote Sens. Environ.* 1:127-129.
- Post, D.F., E.H. Horvath, W.M. Lucas, S.A. White, M.J. Ehasz, and A.K. Batchily. 1994. Relations between soil color and Landsat reflectance on semi-arid rangelands. *Soil Sci. Soc. Am. J.* 58:1809-1816
- Post, D.F. 1984. Soil assessment - remote sensing applications in Arizona. p. 45-56. *In* Proceedings of the applications of remote sensing to agriculture. Office of Arid Land Studies, University of Arizona.
- Price, J.C. 1975. Information content of iris spectra. *Journal of Geophysical Research* 80:1930-1937.
- Reflectance Experiment Laboratory (RELAB) 1993. Description and User's Manual. Brown University - Department of Geological Sciences - RI.
- Resende, M. 1976. Mineralogy, chemistry, morphology and geomorphology of some soils of the central plateau of Brazil. Ph.D. thesis. Purdue University, West Lafayette, Indiana.
- Richardson, A.J., Wiegand, C.L., Gausman, H.W., Cuellar, J.A., and Gerbermann, A.H. 1975. Plant, soil, and shadow reflectance components of row crops. *Photogramm. Eng. Remote Sens.* 41:1401-1407.
- Roberts, D.A., M.O. Smith, D.E. Sabol, J.B. Adams, and S. Ustin. 1992. Mapping the spectral variability in photosynthetic and non-photosynthetic vegetation, soils and shade using AVIRIS. p.38-40. *In* Green R.O. (ed.). Summaries of the 3rd Annual JPL Airborne Geoscience Workshop. AVIRIS Workshop, Pasadena, CA, June 1-5 1992.
- Roberts, D.A. 1991. Separating spectral mixtures of vegetation and soils. Ph.D. thesis, University of Washington, Seattle.
- Robichaud, P.R., and M. Molnau. 1990. Measuring soil roughness changes with an ultrasonic profiler. *Transactions of the ASAE.* 33:1851-1858.
- Robinson, B.F., and L.L. Biehl. 1979. Calibration procedures for measurement of reflectance factor in remote sensign field research. *Proc. Soc. Photo-Opt. Instrum. Eng.* 196:16-26.

- Sabol D. E., Adams J.B., and Smith M.O. 1992. Quantitative Subpixel spectra detection of targets in multispectral images. *J. Geophys. Res.* 97:2659-2672.
- SAS Institute Inc. 1995. SAS/STAT User Guide, release 6.03 Edition. SAS publ., Cary, NC.
- Simanton, J.R., R.M. Dixon, and I. McGowan. 1971. A microroughness meter for evaluating rainwater infiltration. *Hidrology and Water Resources in Arizona and the Southwest* 11:171-174.
- Salomonson, V.V., and W.E. Marlatt. 1971. Airborne measurement of reflected solar radiation. *Remote Sens. Environ.* 2:1-8.
- Savitzky, A., and Golay, M.J.E. 1964. Smoothing and differentiation of data by simplified least squares procedures. *Analytical Chemistry*, 36:1627-1639.
- Schowengerdt, R.A. 1983. *Techniques for Image Processing and Classification in Remote Sensing*. Academic Press, Orlando, Fl.
- Schwertmann, U. 1985. The effect of pedogenic environments on iron oxide minerals. p. 171-200. *In* Stewart, B.A. (ed.) *Advances in Soil Science*. Vol. 1. Springer-Verlag, NY.
- Schwertmann, U., and R.M. Taylor 1977. Iron oxides. *In*: Dixon, J.B., S.B. Weed, J.A. Kittrick, M.H. Milford, and J.L. White eds. *Minerals in Soil Environments*. Soil Science Society of America, Madison, Wisconsin, USA. pp. 145-180.
- Shipman H., and Adams J.B. 1987. Detectability of minerals in desert alluvial fans using reflectance spectra. *J. Geophys. Res.* 92:10391-10492.
- Smith, M.O., J.B. Adams, and D.E. Sabol. 1994. Mapping sparse vegetation canopies p 221-235. *In* J. Hill and J. Megier (ed.) *Imaging spectrometry - a tool for environmental observations*. Kluwer Academic Publishers, Dordrecht, The Netherlands.
- Smith, M.O., D. Roberts, J. Hill, W. Mehl, and B. Hosgood. 1994a. A new approach to quantifying abundances of materials in multispectral images. *IGARSS 1994*.
- Smith, M.O., J.B. Adams, and D.E. Sabol. 1994b. Spectral mixture analysis - new strategies for the analysis of multispectral data. *In* J. Hill and J. Megier (ed.) *Imaging spectrometry - a tool for environmental observations*. Kluwer Academic Publishers, Dordrecht, The Netherlands.

- Smith, M.O., S.L. Ustin, J.B. Adams, and A.R. Gillespie. 1990a Vegetation in Deserts: I A regional measure of abundance from multispectral images. *Remote Sens. Environ.* 31:1-26.
- Smith, M.O., S.L. Ustin, J.B. Adams, and A.R. Gillespie. 1990b Vegetation in Deserts: I I. Environmental influences on regional abundance. *Remote Sens. Environ.* 31:27-52.
- Smith, M.O., D.A. Roberts, H.M. Shipman, J.B. Adams, S.C. Willis, and A.R. Gillespie. 1987. Calibrating AIS images using the surface as a reference. p. 63-69. *In* proceedings of 3rd Airborne Imaging Spectrometer Data Analysis Workshop. JPL Publications. Jet Propulsion Laboratory, Pasadena, CA. 2-4 June, 1987.
- Soil Survey Division Staff. 1993. Soil survey manual. USDA-SCS Agric. Handb. 18. US. Gov. Print. Office, Washington, DC.
- Stoner, E.R., M.F. Baumgardner, R.A. Weismiller, L.L. Biehl, and B.F. Robinson. 1980. Extension of laboratory-measured soil spectra to field conditions. *Soil Sci. Soc. Am. J.* 44:572-574.
- Stoner, E.R., and M.F. Baumgardner. 1981. Characteristic variations in reflectance of surface soils. *Soil Sci. Soc. Am. J.* 45:1161-1165.
- Tang, P.O., I.Y. Fung and T. Takahashi. 1990. Observational constraints on the global atmospheric CO₂ budget. *Science* 247:1431-1438.
- Tanre, D., C. Deroo, P. Duhaut, M.Herman, J.J.Morcrette, J.Perbos, and P.Y.Deschamps. 1986. Simulation of the Satellite Signal in the Solar Spectrum (5S), User's Guide (U.S.T. de Lille, 59655 Villeneuve d'ascq, France: Laboratoire d'Optique Atmospherique).
- Torrent, J., U. Shwertmann, H. Fechter, and F. Alferez. 1983. Quantitative relationship between soil color and hematite content. *Soil Science* 136:354-358.
- van Leeuwen, W.J.D., A.R. Huete, C.L. Walthall, S.D. Prince, A. Begue, and J.L. Roujean. 1997. Deconvolution of remotely sensed spectral mixtures for retrieval of LAI, fAPAR and soil brightness. *Journal of Hydrology*, 188:697-724
- Vane, G., Duval, J.E., and Wellman, J.B. 1993. Imaging spectroscopy of the Earth and other solar system bodies. p. 121-143. *In* Pieters, C.M., and P.A. Englert., (ed.) *Remote Geochemical Analysis: Elemental and Mineralogical Composition*. Cambridge University Press, New York.

- Verdebout, J., Schmuck, G., Ustin, S.L., and Sieber, A.J. 1993. Multitemporal AVIRIS-images of forested and agricultural units in southern Germany. p. 23-31. *In* Vane, G. (ed.) *Imaging Spectrometry of the Terrestrial Environment*. Proceedings of The International Society for Optical Engineering (SPIE), Orlando, Fl. 14-15 April 1993
- Weismiller, R.A., S.K. Kast, M.F. Baumgardner, and F.R. Kirschner. 1979. Landsat MSS data as an aid to soil survey - an operational concept. p. 240. *In* *Machine Processing of Remotely Sensed Data*. Purdue University, West Lafayette, Indiana.
- Wessman, C.A. 1995. Estimating canopy biochemistry through imaging spectrometry. p. 57-69. *In* J. Hill and J. Megier (ed.) *Imaging spectrometry - a tool for environmental observations*. Kluwer Academic Publishers, Dordrecht.
- Wessman, C.A, Aber, J.D., Peterson, D.L., and Melillo, J.M. 1988a. Foliar analysis using near infrared reflectance spectroscopy. *Canadian Journal of Forest Research*, 18:6-11.
- Wessman, C.A, Aber, J.D., Peterson, D.L., and Melillo, J.M. 1988b. Remote sensing of canopy chemistry and nitron cycling in temperate forest ecosystems. *Nature* 335:154-156.
- Westin, C.W., and Frazee, C.J. 1976. Landsat data: its use in a soil survey program. *Soil Sci. Soc. Am. J.* 40:81-92.
- Work, E.A, and Gilmer, D.S. 1976. Utilization of satellite data for inventorying prairie ponds and lakes. *Photogramm. Eng. Remote Sens.* 42:685-694.
- Whitbeck, M.R. 1981. Second derivative infrared spectroscopy. *Appl. Spectrosc.* 35:93-95.